Neurovascular Coupling in healthy human retina evaluated with Optical Coherence Tomography

by

Khushmeet K Dhaliwal

A thesis
presented to the University of Waterloo
in fulfillment of the
thesis requirement for the degree of
Doctor of Philosophy
in
Physics

Waterloo, Ontario, Canada, 2024

© Khushmeet K Dhaliwal 2024

Examining Committee Membership

The following served on the Examining Committee for this thesis. The decision of the Examining Committee is by majority vote.

External Examiner:	Maciej Wojwotski Professor, Institute of Physical Chemistry Polish Academy of Sciences
Supervisor(s):	Kostadinka Bizheva Professor, Department of Physics and Astronomy University of Waterloo
Internal Member:	Melanie Campbell Adjunct and Emeritus Professor, Department of Physics and Astronomy University of Waterloo
Internal Member:	Donna Strickland Professor, Department of Physics and Astronomy University of Waterloo
Internal-External Member:	Chris Hudson Professor, School of Optometry and Vision Science University of Waterloo

Author's Declaration

This thesis consists of material all of which I authored or co-authored: see Statement of Contributions included in the thesis. This is a true copy of the thesis, including any required final revisions, as accepted by my examiners.

I understand that my thesis may be made electronically available to the public.

Statement of Contributions

Chapter 3:

Dhaliwal K, Wong A, Wright T, Bizheva K. "Combined optical coherence tomography and electroretinography (OCT+ERG) system for imaging neurovascular coupling in the human retina", submitted to *Neurophotonics, 2024*.

Kostadinka Bizheva conceived the study and provided the study materials.

Khushmeet Dhaliwal acquired the OCT data, **Tom Wright** acquired the ERG data.

Khushmeet Dhaliwal wrote the algorithm for retinal segmentation, ORG signal extraction, and blood flow analysis. **Khushmeet Dhaliwal** and **Alexander Wong** wrote the algorithm for blood vessel segmentation.

Khushmeet Dhaliwal processed the experimental data.

Khushmeet Dhaliwal analyzed the experimental results.

Khushmeet Dhaliwal and **Kostadinka Bizheva** contributed to the interpretation of the results.

Khushmeet Dhaliwal wrote the first draft of the manuscript.

All authors contributed to the final version for publication.

Chapter 4:

Dhaliwal K, Simmons J, Wong A, Hudson C, Wright T, Ballios B, Bizheva K. "Visual stimulus-evoked transient blood flow and blood vessel diameter changes in human retina measured with a combined OCT+ERG system", to be submitted to *IOVS*, 2024.

Kostadinka Bizheva conceived the study and provided the study materials. **Brian Ballios**, **Chris Hudson** and **Tom Wright** contributed to planning of the study.

Khushmeet Dhaliwal acquired the OCT data; **Tom Wright** acquired the ERG data.

Khushmeet Dhaliwal wrote the algorithm for retinal blood flow detection and **James Simmons** and **Khushmeet Dhaliwal** wrote the algorithm for blood vessel segmentation, with the help of **Alex Wong**.

Khushmeet Dhaliwal and **James Simmons** processed the experimental data.

Khushmeet Dhaliwal analyzed the experimental results.

Khushmeet Dhaliwal, **Kostadinka Bizheva**, **Chris Hudson**, **Brian Ballios**, and **Tom Wright** all contributed to the interpretation of the results.

Khushmeet Dhaliwal wrote the first draft of the manuscript.

All authors contributed to the final version in preparation for publication.

Chapter 5:

Dhaliwal K, Hudson C, Wright T, Ballios B, Bizheva K. "Color and frequency dependence of flicker induced transient retinal blood flow changes in healthy human retina measured with OCT".

Kostadinka Bizheva conceived the study and provided the study materials. **Chris Hudson**, **Brian Ballios** and **Tom Wright** contributed to the organization of the study.

Khushmeet Dhaliwal acquired the OCT data.

Khushmeet Dhaliwal wrote the algorithm for retinal blood flow detection and blood vessel segmentation.

Khushmeet Dhaliwal processed the experimental data.

Khushmeet Dhaliwal analyzed the experimental results.

Khushmeet Dhaliwal, **Kostadinka Bizheva**, **Chris Hudson** all contributed to the interpretation of the results.

Khushmeet Dhaliwal wrote the first draft.

Abstract

Retinal neurodegenerative diseases such as glaucoma, age-related macular degeneration (AMD), diabetic retinopathy, and retinitis pigmentosa affect millions of people worldwide and pose a significant burden on public health and the economy. Glaucoma, impacting approximately 80 million people globally, is a leading cause of irreversible blindness. In 2019, an estimated 19.8 million Americans (12.6%) were living with AMD, of which about 1.49 million people faced vision-threatening conditions. An estimated 9.6 million people were living with diabetic retinopathy in 2021, with about 1.84 million of them experiencing vision-threatening stages. In the United States alone, vision impairments- including those resulting from these retinal diseases- cost an estimated $139 billion annually.

Retinal neurodegenerative diseases not only cause progressive damage to the retinal morphology and vascular network, but also cause acute and transient metabolic, physiological, and blood flow changes at the early stages of the disease development which become permanent and chronic at the advanced stages of the disease. Neurovascular Coupling (NVC) refers to the transient vasodilation and increased retinal blood flow resulting from the increased metabolic activity of retinal neurons in response to visual stimulation.

Over the past few decades, a range of imaging techniques from clinical ophthalmoscope and confocal microscopy to adaptive optics scanning laser ophthalmoscope and optical coherence tomography (OCT) have been used *ex vivo* and *in vivo* to study components of the neurovascular coupling and its underlying mechanisms. Techniques such as Laser Doppler Velocimetry, Optical Coherence Tomography Angiography (OCTA), and Doppler Optical Coherence Tomography (D-OCT) have been used to observe the vascular responses of the retina caused by visual stimulation. Additionally, Electroretinography (ERG) has been widely used in clinical settings to evaluate the electrical activity of the neuronal retina. More recently, an optical equivalent to ERG, Optoretinography (ORG) was developed and OCT technology, imaging protocols, and image processing algorithms were designed to conduct OCT-based ORG studies in the human and animal retina. However, most of the Doppler OCT, OCTA, and ORG studies have examined components of the neurovascular coupling separately, potentially overlooking the dynamic interactions and comprehensive responses inherent in neurovascular coupling.

OCT, which acquires simultaneously both intensity and phase information, is particularly well-suited for investigating neurovascular coupling in the retina, as it enables a completely non-invasive approach for simultaneous monitoring of retinal blood flow dynamics and neuronal responses. The integration of a commercial ERG system with a research-grade OCT modality adds further value by offering easy control of the visual stimulus,

use of clinically established ERG protocols designed to elicit responses from specific types of retinal neuronal cells, and using the ERG recordings to validate the visually-evoked neuronal responses. The main objectives of this PhD thesis were:

- To develop a combined OCT+ERG imaging system to conduct *in vivo* and simultaneously morphological and functional imaging that can be utilized for investigating neurovascular coupling in the human retina.
- To evaluate the performance and capabilities of the OCT+ERG system, imaging protocols, and image processing algorithms by conducting a pilot study on healthy human subjects.
- To utilize the OCT+ERG technology to explore the neurovascular coupling mechanisms in the healthy human retina by extracting vascular and neuronal responses from different retinal layers simultaneously.
- To examine the effects of different wavelengths and flicker frequencies on the dynamic retinal blood flow changes evoked by visual stimulation, providing deeper insights into the mechanisms of neurovascular coupling.

Results from this PhD research have been summarized in three manuscripts that are either under review or under preparation for submission. Therefore, this PhD thesis was prepared in such a way that individual manuscripts represent separate thesis chapters.

Acknowledgements

The journey of my PhD has been one of the most cherished chapters of my life, filled with invaluable experiences and growth. None of this would have been possible without the unwavering support of those who lifted me up in times of need, cheered for me, and steadfastly supported me through every challenge.

First and foremost, I wish to express my deepest gratitude to my supervisor, Prof. Kostadinka Bizheva, whose exceptional guidance, mentorship, and encouragement have shaped me into the researcher I am today. Her ability to strike a harmonious balance between independence and support has been pivotal to my growth. I am also profoundly thankful for her financial support and the opportunities she created for me to collaborate with other researchers.

My sincere thanks also go to Prof. Chris Hudson for the enlightening discussions on retinal physiology, which greatly enriched my understanding and approach. I am equally grateful to Prof. Alexander Wong for his valuable insights into image processing tools, which enhanced the depth of my research. I extend my appreciation to Dr. Tom Wright and Prof. Daphne McCulloch for their dedicated training and support with the ERG system.

I am profoundly grateful to my PhD committee members, Prof. Donna Strickland and Prof. Melanie Campbell, for their insightful guidance and steadfast support throughout this journey. Their expertise and encouragement have been invaluable to my progress.

The saying "It takes a village to achieve success" holds true, and I am reminded of this as I extend my heartfelt thanks to Hiruy Haile from the machine shop, and Krunomir Dvorski and Ennis Solorzano from the electrical shop. Their skill and dedication brought my designs and ideas to life, making a tangible impact on my research.

To my colleagues, Keyu Chen, Steph Swanson, Nima Abbasi, and Simran Pattar, thank you for the engaging discussions and for making the lab a place of camaraderie and enjoyment. These years would not have been as fulfilling or memorable without your support and friendship.

To my friends, both in Waterloo and around the world, thank you for keeping me grounded and inspiring me to keep pushing forward. Your companionship and unwavering support have meant more to me than words can express.

To my partner, Nitheesh Pillai, you have been my steadfast companion through every high and low. This achievement is as much yours as it is mine, and I am endlessly grateful for your love, patience, and belief in me.

Finally, to my parents and my brother, thank you for being my constant pillars of encouragement and for always pushing me to strive for excellence. Mumma, I wish you were here to witness this moment. You have been my greatest supporter, and I dedicate this achievement to you. I know you would be proud of who I am today.

Dedication

This and every achievement of my life is dedicated to you, mumma!

Table of Contents

Examining Committee Membership ii

Author's Declaration iii

Statement of Contributions iv

Abstract vi

Acknowledgements viii

Dedication x

List of Figures xv

List of Tables xxii

List of Abbreviations xxiii

Quotation xxv

1 Introduction 1

1.1 Motivation 1

1.2 Retinal Layers 5

1.3 Retinal Blood Flow 8

1.4 Thesis Organization 9

2 Optical Coherence Tomography (OCT) 11
2.1 Optical Coherence Tomography: Theory . . . 12
2.2 Different designs of OCT systems . . . 15
2.2.1 Time-Domain OCT (TD-OCT) . . . 15
2.2.2 Fourier-Domain OCT (FD-OCT)/Spectral-Domain OCT (SD-OCT) 16
2.3 OCT imaging modalities . . . 18
2.4 Characteristics of an FD-OCT system . . . 20
2.4.1 Axial Resolution . . . 20
2.4.2 Lateral Resolution . . . 21
2.4.3 Depth of Focus . . . 23
2.4.4 Digital Resolution . . . 23
2.4.5 Scanning Range . . . 24
2.4.6 Signal to Noise Ratio (SNR) . . . 25
2.5 Doppler OCT . . . 26
2.5.1 Double circular Scanning protocol . . . 28
2.6 Electroretinography (ERG) . . . 30
2.7 Optoretinography (ORG) . . . 32
2.7.1 Intensity-based ORG (iORG) . . . 33
2.7.2 Phase-based ORG (pORG) . . . 34

3 Combined optical coherence tomography and electroretinography (OCT+ERG) system for imaging neurovascular coupling in the human retina 35
3.1 Introduction . . . 37
3.2 Methods . . . 38
3.2.1 OCT+ERG system . . . 38
3.2.2 In-vivo imaging of the human retina . . . 41
3.2.3 Visual stimulation and image acquisition protocols . . . 41
3.2.4 Image processing and data analysis . . . 43

3.3 Results . . . 47
3.3.1 Morphological human retinal images . . . 47
3.3.2 Retinal response to a flash with one intensity . . . 47
3.3.3 Retinal response to different intensities . . . 52
3.4 Discussion . . . 54
3.5 Conclusions . . . 56

4 Visual stimulus-evoked transient blood flow and blood vessel diameter changes in human retina measured with a combined OCT+ERG system 58
4.1 Introduction . . . 60
4.2 Methods . . . 62
4.2.1 OCT+ERG system . . . 62
4.2.2 Subjects . . . 63
4.2.3 Image acquisition protocols and visual stimulation . . . 65
4.2.4 Data analysis . . . 66
4.2.5 Algorithms . . . 67
4.3 Results . . . 68
4.3.1 Functional RBF changes . . . 68
4.3.2 Functional RBV Diameter changes . . . 71
4.3.3 ERG responses . . . 75
4.4 Discussion . . . 75
4.5 Conclusions . . . 78

5 Color and frequency dependence of flicker induced transient retinal blood flow changes in healthy human retina measured with OCT 80
5.1 Introduction . . . 82
5.2 Methods . . . 84
5.2.1 OCT system . . . 84
5.2.2 Imaging Protocol and processing . . . 84

5.2.3 Stimulation . . . 85
5.2.4 Subjects . . . 86
5.3 Results . . . 86
5.3.1 Differential RBF responses in Arteries and Veins to White-Light Flicker Stimulation at 10 Hz and 30 Hz . . . 87
5.3.2 Differential RBF Responses in Arteries and Veins to Red-Light Flicker Stimulation at 10 Hz and 30 Hz . . . 89
5.3.3 Differential RBF Responses in Arteries and Veins to Green-Light Flicker Stimulation at 10 Hz and 30 Hz . . . 91
5.3.4 Differential RBF Responses in Arteries and Veins to Blue-Light Flicker Stimulation at 10 Hz and 30 Hz . . . 93
5.4 Discussion . . . 94
5.5 Conclusions . . . 96

6 Conclusions **97**
6.1 Summary and contributions . . . 97
6.2 Future Work . . . 98

References **99**

List of Figures

1.1 Neurovascular Coupling in the Retina. (A) Neurovascular unit depicting the different neuronal and glial cells involved in the process; figure prepared in BioRender, referenced from Haider *et. al.*, Biomolecules, 2022. (B) Schematic showing the process involved in Neurovascular Coupling: Stimulus causes neuronal activation, leading to increased metabolic activity and increased oxygen and glucose demands in the tissue, which leads to increased release of vasoactive chemicals causing vasodilation of retinal blood vessels and an increase in the retinal blood flow (RBF). 2

1.2 (A) The human eye where the blue polygon shows the approximate location of the zoomed in figures B and C. (B) Structure of human retina and the cells forming the different layers of the retina; figure prepared in BioRender, referenced from Kolb *et. al.*, 2005. (C) OCT B-scan showing the different layers in the retina, corresponding to the layers in figure B. 7

1.3 (A) The human eye and the blue polygon outlines the Optic Nerve region. (B) Optic Nerve vasculature, showing the central retinal artery and vein nourishing the anterior retina; posterior ciliary arteries nourishing the posterior retina through choroid. (C) Capillary networks in the different retinal layers: Superficial Capillary Plexus in the Nerve Fiber and Ganglion Cell Layers, Intermediate Capillary Plexus in the Inner Plexiform Layer, and Deep Capillary Plexus in the Outer Plexiform Layer of the retina; figure prepared in BioRender. 8

2.1 (A) A representative OCT A-scan. (B) An OCT B-scan of a human retina generated by combining A-scans. (C) A volumetric OCT scan. 12

2.2 A simplified schematic of a fiber-based OCT system based on Michelson Interferometer. 13

2.3 (A) A simplified schematic for Time-Domain OCT system with a translational reference mirror. (B) A simplified schematic of the Spectral-Domain OCT system with a spectrometer and a line detector. (C) A simplified schematic of the Swept-Source OCT system with a swept-wavelength light source. 18

2.4 (A) Shape of the beam in imaging plane in PSc-OCT system. (B) Beam shape at the imaging plane in LS-OCT system. (C) Beam shape at the imaging plane in FF-OCT system. 19

2.5 (A) Low NA objective creates a larger beam waist. (B) A high NA objective creates a smaller beam waist. (C) Gaussian beam profile near the focal plane depicting the beam characteristics. 22

2.6 A schematic of back-scattering geometry for Doppler OCT, depicting the Doppler angle θ between the incident beam and the blood corpuscle velocity. 27

2.7 Schematic depicting the geometry of the concentric circular scanning protocol across the retina, cross-sectioning a blood vessel at two locations. . . . 29

2.8 (A) Neuronal unit of the retina, showing from left the retinal pigment epithelium cell, a cone photoreceptor, a bipolar cell and a retinal ganglion cell; figure prepared in BioRender. (B) A standard ERG trace showing a-wave, b-wave, and the oscillatory potentials and the cells these responses originate from. 31

3.1 (A) Schematic of the combined OCT+ERG system. (B) Photograph of the OCT+ERG imaging probe. (C) Laser spectrum measured from the reference arm of the OCT system. (D) Axial OCT PSF after hardware (red color) and software (black color) dispersion compensation. (E) Sensitivity roll-off with imaging depth. 39

3.2 Image acquisition protocol for the optoretinography and functional blood flow recordings. (A) Timeline of the visual stimulus. (B) A sequence of 1,200 repeated B-scans acquired over duration of $\sim$ 6 seconds from a location in the retina approximately midway between the fovea and optic nerve head (C, red line). 42

3.3 Protocol for extracting ORG traces from the repetitive B-scans. (A) A representative B-scan showing the layered structure of the human retina and cross-sections of large blood vessels in the RNFL. (B) Flow chart of the image processing steps to extract the optical path length difference (OPD) and intensity ORG traces from different retinal layers. Example ORG traces: OPD (C) and intensity (D) extracted from the OS-2 band of the photoreceptors layer. 43

3.4 Protocol for measuring transient changes in the retinal blood vessels. (A) A representative retinal B-scan with the cross-section of a retinal blood vessel marked with the red dashed line. (B) Flow chart of the image processing steps to quantify dynamic vascular responses (blood flow change and dilation / constriction of retinal blood vessels) to visual stimulation. (C) Retinal blood flow change in response to 4 ms single flash white-light stimulus. (D) Corresponding blood vessel diameter change. 45

3.5 OCT images of the healthy human retina. The high spatial resolution is sufficient to resolve the Bruch's membrane (green arrow), the RPE (orange arrow), the photoreceptors OS-2 layer (blue arrow) and reflections from individual cone OS tips (red arrow) (A), the 3 sub-layers in the retinal IPL (B) and the intricate capillary network in the retinal OPL (C). *En face* view of the photoreceptors IS/OS junction (D). Magnified views of the photoreceptors mosaic, where tips of individual cones are resolved (white dots in E and F). 48

3.6 (A) Representative B-scan of the healthy human retina from a functional OCT time series with layers labeled. (B) Retina intensity profiles extracted from the series of B-scans for selected time points before, during and after application of the visual stimulus. Pictorial representation of the cellular pathway for generation of visual information. 49

3.7 Summary of the healthy human retina response to visual stimulation (white light, single flash, 4 ms duration and $43.4 cd.s/m^2$ intensity) in terms of physiological changes in the retinal neurons measured with OCT (intensity and OPD changes) and ERG, and vascular changes (transient changes in the RBF and BVD). (A) Optical pathlength changes from PR OS-2 layer. Intensity changes measured from retinal layers located in the posterior (B) and anterior (C) retina. (D) Representative ERG recording. Visually evoked changes in the retinal blood flow (E) and blood vessel diameter (F). 50

3.8 Different responses at different intensities of single-flash stimuli. (A) ERG traces; (B) RBF changes; (C) BVD changes; (D) and (H) Optical path length and intensity changes in the photoreceptor OS-2 layer; (E) and (I) Optical path length and intensity changes in the outer plexiform layer; (F) and (J) Optical path length and intensity changes in the inner plexiform layer; and (G) and (K) Optical path length and intensity changes in the retinal nerve fiber layer. 52

4.1 (A) *En face* projection of the Optic Nerve Head, where red lines show the approximate location of the OCT double circular scans. (B) Unwrapped circular B-scan, showing vessel cross-sections. (C) Plot showing raw RBF data (black curve), smoothed using a moving Savitzky-Golay function (red curve). (D) The smoothed curve is further band-blocked to remove fluctuations due to pulsatile motion (blue curve). (E) The mean of the first two seconds of RBF values serves as the baseline value to obtain RBF percentage change, characterized by Amplitude and Latency. 64

4.2 Flow-chart depicting the retinal blood flow and retinal blood vessel diameter processing algorithm. 67

4.3 (A) Fractional RBF change measured from an artery at baseline (black curve) and in response to 10 Hz white-light flicker stimulation of increasing intensities (red, blue, and green curves). (B) Average RBF peak magnitude measured in retinal arteries in response to increasing stimulus intensity. (C) Average RBF peak latency response measured in arteries in response to 10 Hz white-light flicker stimulation. (D) Fractional RBF change measured from a vein at baseline (black curve) and in response to 10 Hz white-light flicker stimulation of increasing intensities (red, blue, and green curves). (E) Average RBF peak magnitude measured in retinal veins in response to increasing stimulus intensity of 10 Hz white-light flicker stimulation. (F) Average RBF peak latency measured in veins in response to 10 Hz white-light flicker stimulation. 69

4.4 (A) Summary of the RBF peak change in arteries (red plot), veins (green plot), and total blood flow behavior (black plot) in response to increasing stimulus intensity of 10 Hz white-light flicker stimulation. (B) RBF peak latency trend in arteries (red curve), veins (green curve), and overall vessel response (black curve) to increasing stimulus intensity of 10 Hz white-light flicker stimulation. The error bars represent the Standard Error of the mean values. 70

4.5 (A) Retinal blood vessel diameter changes in the lateral direction in an artery in response to varying stimulus intensities of 10 Hz white-light flicker stimulation (red and blue curves). (B) Retinal blood vessel diameter changes in the axial direction in an artery in response to varying stimulus intensities of 10 Hz white-light flicker stimulation (red and blue curves); the black curves in these figures represent the response of the blood vessel in the absence of flicker stimulation. (C) Time-averaged vessel cross-section of an artery before flicker stimulation. (D) Time-averaged vessel cross-section of an artery during flicker stimulation. (E) Retinal blood vessel diameter changes in the lateral direction in a vein in response to varying stimulus intensities of 10 Hz white-light flicker stimulation (red and blue curves). (F) Retinal blood vessel diameter changes in the axial direction in a vein in response to varying stimulus intensities of 10 Hz white-light flicker stimulation (red and blue curves); the black curves in these figures represent the response of the blood vessel in the absence of flicker stimulation. (G) Time-averaged vessel cross-section of a vein before flicker stimulation. (H) Time-averaged vessel cross-section of a vein during flicker stimulation. 72

4.6 (A) Retinal blood vessel diameter changes in the lateral direction in arteries as a function of the vessel diameter in response to increasing stimulus intensity for 10 Hz of white-light flicker stimulation. (B) Retinal blood vessel diameter changes in the axial direction in arteries as a function of the vessel diameter in response to increasing stimulus intensity for 10 Hz of white-light flicker stimulation. (C) Retinal blood vessel diameter changes in the lateral direction in veins as a function of the vessel diameter in response to increasing stimulus intensity for 10 Hz of white-light flicker stimulation. (D) Retinal blood vessel diameter changes in the axial direction in veins as a function of the vessel diameter in response to increasing stimulus intensity for 10 Hz of white-light flicker stimulation. 74

4.7 (A) ERG traces in response to increasing intensity of 10 Hz white-light flicker stimulus. (B) Zoomed in ERG response depicting the negative a-wave and the first positive b-wave. 76

5.1 (A) RBF response measured from an artery (red) and a vein (green) in response to 10 Hz of white-light flicker stimulation. The black curve corresponds to RBF changes measured during dark recordings (no stimulus). RBF peak amplitude (B) as a function of the stimulus intensity for arteries (red), veins (green), and the total retinal blood flow (black) and latency (C) as a function of the stimulus intensity in response to 10 Hz white-light flicker stimulation. (D) RBF response measured from an artery (red) and a vein (green) in response to 30 Hz of white-light flicker stimulation. RBF peak amplitude (E) to varying stimulus intensities for arteries (red), veins (green), and the total retinal blood flow (black). (F) Latency response of arteries (red) and veins (green) to varying stimulus intensities. The error bars represent the Standard Error of the mean values. Statistically significant differences in the arterial and venous RBF responses are marked with an asterisk in Figures 5.1B and 5.1C. 88

5.2 (A) RBF response measured from an artery (red) and a vein (green) in response to 10 Hz of red-light flicker stimulation. The black curve corresponds to RBF changes measured during dark recordings (no stimulus). RBF peak amplitude (B) and latency (C) as functions of the stimulus intensity to varying stimulus intensities. (D) RBF response measured from an artery (red) and a vein (green) in response to 30 Hz of white-light flicker stimulation. RBF peak amplitude (E) and latency (F) to varying stimulus intensities. The error bars represent the Standard Error of the mean values. 90

5.3 (A) RBF response measured from an artery (red) and a vein (green) in response to 10 Hz of green-light flicker stimulation. The black curve corresponds to RBF changes measured during dark recordings (no stimulus). RBF peak amplitude (B) and latency (C) as functions of the stimulus intensity to varying stimulus intensities. (D) RBF response measured from an artery (red) and a vein (green) in response to 30 Hz of white-light flicker stimulation. RBF peak amplitude (E) and latency (F) to varying stimulus intensities. The error bars represent the Standard Error of the mean values. 92

5.4 (A) RBF response measured from an artery (red) and a vein (green) in response to 10 Hz of blue-light flicker stimulation. The black curve corresponds to RBF changes measured during dark recordings (no stimulus). RBF peak amplitude (B) and latency (C) as functions of the stimulus intensity to varying stimulus intensities. (D) RBF response measured from an artery (red) and a vein (green) in response to 30 Hz of white-light flicker stimulation. RBF peak amplitude (E) and latency (F) to varying stimulus intensities. The error bars represent the Standard Error of the mean values. 93

List of Tables

3.1 Bleaching percentage for different stimulus intensities. 42

4.1 Bleaching percentage for different stimulus intensities. 65

4.2 Peak RBF change values (mean and standard error) for different subjects using various stimulus intensities in the study. 71

4.3 RBF peak latency values (mean and standard error) for different subjects using various stimulus intensities in the study. 73

5.1 Bleaching percentage for different stimulus intensities for different colors of stimulation. 86

List of Abbreviations

AMD	Age-related Macular Degeneration
ANSI	American National Standards Institute
AO	Adaptive Optics
AO-SLO	Adaptive Optics Scanning Laser Ophthalmoscope
BF	Blood Flow
BVD	Blood Vessel Diameter
CMOS	Complementary Metal Oxide Semiconductor
COST	Cone Outer Segment Tip
CW	Continuous Wave
DC	Dispersion Compensation
DCP	Deep Capillary Plexus
D-OCT	Doppler Optical Coherence Tomography
DOF	Depth of Focus
ELM	External Limiting Membrane
ERG	Electroretinography
FA	Fluorescein Angiography
FD	Fourier-Domain
FD-OCT	Fourier-Domain Optical Coherence Tomography
FF	Full-Field
FF-OCT	Full-Field Optical Coherence Tomography
FOV	Field-of-View
FWHM	Full-Width at Half-Maximum
GCL	Ganglion Cell Layer
ICG	Indocyanine Green
ICP	Intermediate Capillary Plexus
ILM	Internal Limiting Membrane
INL	Inner Nuclear Layer
IOS	Intrinsic Optical Signal
IPL	Inner Plexiform Layer
IS	Inner Segment
ISOS	Inner Segment-Outer Segment
LDF	Laser Doppler Flowmetry

LDV	Laser Doppler Velocimetry
LED	Light Emitting Diode
LF-OCT	Line-Field Optical Coherence Tomography
LS-OCT	Line-Scan Optical Coherence Tomography
MEMS	Micro-Electromechanical System
MPE	Maximum Permissible Exposure
NA	Numerical Aperture
NFL	Nerve Fiber Layer
NIR	Near-Infrared
NVC	Neurovascular Coupling
OCT	Optical Coherence Tomography
OCTA	Optical Coherence Tomography Angiography
ONH	Optic Nerve Head
ONL	Outer Nuclear Layer
OP	Oscillatory Potentials
OPD	Optical Pathlength Difference
OPL	Outer Plexiform Layer
ORG	Optoretinography
OS	Outer Segment
PR	Photoreceptor
PSc	Point-Scan
PSc-OCT	Point-Scan Optical Coherence Tomography
PSF	Point Spread Function
RBF	Retinal Blood Flow
RBV	Retinal Blood Vessel
RBVD	Retinal Blood Vessel Diameter
RNFL	Retinal Nerve Fiber Layer
RPE	Retinal Pigment Epithelium
SD	Spectral-Domain
SD-OCT	Spectral-Domain Optical Coherence Tomography

"It always seems impossible until it's done."

Nelson Mandela

Chapter 1

Introduction

1.1 Motivation

The human eye serves as a gateway to the outside world, allowing us to experience the beauty of our surroundings. The optics of the anterior segment of our eyes focus light and create an image of the visual world onto a layer at the posterior segment of the eye, called the retina. In a way, the retina can be considered as the sensor of a high-resolution camera, converting the optical image into electrical neural impulses that are transmitted to the brain, creating visual perception.

The retina is a light-sensitive tissue composed of various specialized cells called neurons, which also serve as the fundamental units of the brain [1]. During embryonic development, the retina and the optic nerve originate from the same tissue as the central nervous system, making the retina an extension of our brain [2]. This unique relationship between the retina and the brain has led to the retina being referred to as 'the window to our brain' [3]. The retina is also highly vascularized, with the anterior portion of the retina nourished by surface blood vessels originating from the optic nerve head and the posterior retina supported by the choroidal vasculature [4–8].

Functional Hyperemia, first described by Roy and Sherrington in 1890 in the brain [9], refers to the dilation or constriction of blood vessels and the subsequent increase or decrease in blood flow in response to neuronal metabolic demands [10]. In the retina, this process is referred to as neurovascular coupling, which reflects the relationship between the stimulus-evoked changes in the neuronal function and the corresponding changes in the local blood vasculature (transient blood flow increase or decrease and dilation or constriction

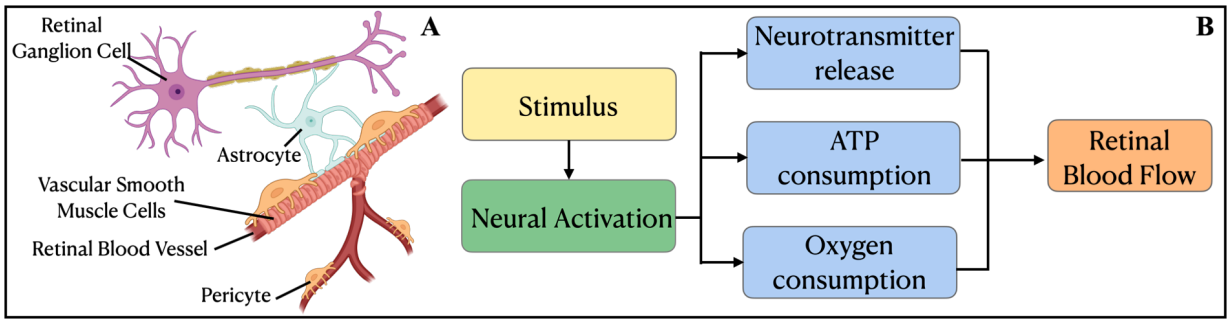


Figure 1.1: Neurovascular Coupling in the Retina. (A) Neurovascular unit depicting the different neuronal and glial cells involved in the process; figure prepared in BioRender, referenced from Haider *et. al.*, Biomolecules, 2022. (B) Schematic showing the process involved in Neurovascular Coupling: Stimulus causes neuronal activation, leading to increased metabolic activity and increased oxygen and glucose demands in the tissue, which leads to increased release of vasoactive chemicals causing vasodilation of retinal blood vessels and an increase in the retinal blood flow (RBF).

of the blood vessels) [11–15], as depicted in Figure 1.1, which is referenced from [16, 17]. Neurovascular coupling is crucial for maintaining retina health, ensuring that the metabolic demands of the neurons are met by providing appropriate amounts of nutrients and oxygen through blood flow adjustments [7, 18, 19].

Retinal neurodegenerative diseases, such as glaucoma [20–22], age-related macular degeneration [23, 24], retinitis pigmentosa [25–29], and diabetic retinopathy [30–32], are known to induce both morphological as well as physiological changes in the retina [7]. It is hypothesized that these conditions impair retinal autoregulation and neurovascular coupling, furthering the disease progression [7, 31].

Over the years, numerous imaging modalities have been employed to visualize and quantify ocular blood flow *in vivo*. Techniques such as Fundus Photography [33, 34], Laser Doppler Flowmetry (LDF) [35, 36], Laser Doppler Velocimetry (LDV) [11, 37–39], Scanning Laser Ophthalmoscope (SLO) [40, 41], Fluorescein Angiography (FA) [42–44], and Indocyanine Green (ICG) Angiography [45, 46] have been instrumental in advancing our understanding of retinal blood circulation.

Fundus Photography allows for the visualization of the retina and the vasculature nourishing its anterior segment [34]. It can be used to detect changes in the retinal structure and vasculature, especially evident at the later stages of retinal neurodegenerative diseases. Retinal Vessel Analyzers, which often utilize a Fundus Camera, enable the measurement of

retinal blood vessel diameters directly from the fundus photographs, and have been widely used in past studies [15, 47]. While this imaging technology has a compact and relatively simple optical design and has been used for clinical examination of the retina for nearly a century, this technology provides only *en face* view of the retina with limited spatial resolution [48]. FA and ICG Angiography techniques are used for retinal examination, and both techniques utilize a contrast agent- fluorescein and indocyanine green dye, respectively- to visualize and derive qualitative information about the ocular blood flow and blood perfusion [42]. FA is used to contrast retinal blood vessels [43, 44]. ICG, on the other hand, absorbs light in the near-infrared (NIR) region where tissue scattering is lower, allowing for imaging of the choroidal vasculature [45, 46]. While these techniques are effective for visualizing retinal and choroidal vasculature, they rely on the administration of contrast agents, making them invasive and not suitable for routine procedures [49, 50]. Moreover, they lack direct derivation of quantitative information on retinal blood flow, which is an important marker for some disease detection.

LDF is a non-contact and label-free technique used in ophthalmology to measure retinal blood flow [37]. This technique is based on the principle of Doppler shift, where the frequency of light scattered by the moving blood corpuscles in the retinal vessels differs from that of the surrounding static tissue. By analyzing these frequency shifts, LDF provides relative quantitative information about particle concentration and blood flow, often used for assessing tissue perfusion [35, 36]. Similarly, LDV is a technique used for assessing the local retinal blood velocity [38]. While both of these methods provide valuable quantitative information, they can be time-consuming and may not be practical for routine clinical use.

Optical Coherence Tomography (OCT), first reported in 1991, has emerged as an alternative imaging modality that offers *in-vivo*, non-contact, non-invasive, high-resolution, and volumetric imaging capabilities [51]. With its ability to provide high cellular-level resolution and high-speed acquisition, OCT technology is being increasingly used in both clinical practices and research settings for retinal assessment and diagnosis [52, 53]. Importantly, OCT can simultaneously capture neuronal responses and associated blood vessel changes, making it an ideal tool for studying neurovascular coupling [54]. For almost two decades, it has been extensively used to measure retinal blood flow *in vitro* [55–57] and *in vivo* [58–64]. Functional extensions of OCT, such as Doppler OCT (D-OCT) [65–67], and Optical Coherence Tomography Angiography (OCTA) [68–72], enable the observation of stimulus-evoked retinal blood flow changes, while phase-resolved methods facilitate the detection of neuronal changes [73–88]. However, most of these studies have relied on sequential experiments to examine these neurovascular components separately, potentially overlooking dynamic, real-time interactions between neuronal and vascular responses.

Optoretinography (ORG) is the optical equivalent of electroretinography(ERG), which

is a clinically established method for electrical recordings of the responses of retinal neurons to visual stimulation. The use of OCT for non-invasive, optical recording of visually evoked neuronal changes was first proposed by Bizheva and the proof-of-principle was demonstrated *in vitro* in animal tissue where OCT and ERG data were acquired synchronously [89]. With advances in camera and laser technologies, over the past 20 years different OCT system designs were developed for ORG recordings of visually evoked neuronal activity in the human and animal retina: point scanning Spectral Domain OCT [81], AO-OCT [76,77], Full-Field SS-OCT [74,83,85,88] and Line-Field -SD-OCT [78,84]. While majority of the ORG data was acquired mostly from healthy retinas, most recent studies have explored changes in the ORG signal related to retinal diseases [28].

The primary objective of this thesis research is to explore the applications of OCT to investigate neurovascular coupling in healthy human retina. With its high resolution and ability to provide volumetric information, OCT enables the recording of stimulated neurons as well as the associated vascular response from the same dataset, thus offering invaluable insights into neurovascular coupling. The specific goals outlining this PhD research are:

- To investigate neurovascular coupling in the healthy human retina using a combined OCT and electroretinography (ERG) system.
- To measure retinal blood flow changes in the optic nerve head in the healthy human retina in response to white-light flicker stimulation.
- To characterize the cone and rod responses and the related retinal blood flow changes in the human retina using colored flicker stimulation (red, green, and blue).

To fully understand the mechanisms of neurovascular coupling and the stimulus-evoked blood flow changes in the retina, it is crucial to appreciate the intricate structure of the retina. Each of the retinal layers performs different functions and is composed of different cell types, which together contribute to the complex process of visual perception. The interaction between cells in these layers plays a key role in regulating blood flow in response to increased neuronal activity due to visual stimulation. A detailed understanding of these retinal layers and the complex retinal vascular supply is, therefore, fundamental to understanding how neuronal stimulation and vascular responses are coordinated within the retina.

1.2 Retinal Layers

The human retina, the innermost layer of the vertebrate eye, contains photosensitive pigments essential for the detection of light [90, 91]. It is a highly organized, multi-layered tissue, as shown in Figure 1.2, that transforms light into neural signals [1, 92]. The neural retina is composed of several layers of neuronal cells interconnected by synapses and is supported by an outer layer of pigmented epithelium. Each layer of the retina plays a specific role in visual processing and interaction with blood vessels [91]. From the farthest to the closest from the vitreous body, they are [90]:

1. **Retinal pigment epithelium (RPE):** This is the outermost layer of the retina and the closest to the choroid. It is formed of a single layer of cuboidal epithelial cells and provides support and nourishment to the neural retina. The pigment in this layer prevents light reflection throughout the globe of the eyeball, thereby playing an important role in clear vision. RPEs also play a crucial role in recycling the cellular debris from the photoreceptors via the choroidal blood vessels. Damage to the RPEs in diseases like AMD leads to the accumulation of cellular waste in the retina, causing degeneration of photoreceptors.

2. **The inner segment and outer segment (IS/OS) of the photoreceptors:** This is the layer where the inner and the outer segments of the photoreceptors, the rods and the cones, lie. The rods are mainly responsible for night vision and are easily saturated in the daylight or any bright light, whereas cones provide color vision.

    - The **outer segments** of the photoreceptors contain a specialized photopigment called the rhodopsin. Rhodopsin consists of a protein 'Opsin' and a chromophore 'Retinal'. Retinal absorbs photons of light and triggers a biochemical process called phototransduction. Humans have four different opsins, one found in the rods and the other three found in cones responding to small, medium, and long wavelengths, corresponding to the S, M, and L cones.
    - The **inner segments** of the photoreceptors contain the densely packed mitochondria that generate energy for the photoreceptors.

3. **External Limiting Membrane (ELM):** This layer has a network-like structure that separates the inner segment portions of the photoreceptors from their cell somas.

4. **Outer Nuclear Layer (ONL):** This layer contains the cell bodies (somas) of the photoreceptors, housing their nuclei and essential organelles for cellular function.

5. **Outer Plexiform Layer (OPL):** This is a layer of dense network of neuronal synapses in the retina. Here, the rod spherules and the cone pedicles meet the dendrites of the horizontal, bipolar, and amacrine cells. Retinal bipolar cells transmit signals, directly or indirectly (via Amacrine cells), from the photoreceptors to the ganglion cells. Amacrine cells work laterally and help integrate, modulate, and adjust the timing of the ganglion cell output of the retina. Horizontal cells integrate and regulate input from multiple photoreceptors, contributing to the processing of visual signals through lateral inhibition, which enhances contrast.

6. **Inner Nuclear Layer (INL):** This layer contains the somas of the bipolar, horizontal, and amacrine cells. Cell bodies of Müller cells also lie in this layer.

7. **Inner Plexiform Layer (IPL):** This layer, like the OPL, contains synapses between different types of neurons. Here, bipolar cell axons form synapses with the ganglion cell dendrites. The IPL is formed of 5 sublayers depending on the different types of bipolar cells forming synapses with ganglion cells.

8. **Ganglion Cell Layer (GCL):** This layer contains the cell somas of the ganglion cells.

9. **Nerve Fiber Layer (NFL):** This layer is composed of the ganglion cell axons, that are bundled together and protected with a myelin sheath to form nerve fibre bundles and the optic nerve head (ONH).

10. **Inner Limiting Membrane (ILM):** This is a basement membrane layer that also includes the Müller Cells' synapses. This layer separates the retina from the vitreous humor.

In addition to these different types of neuronal cells, there are glial cells like Müller cells, Astrocytes, and Microglia that are also present in the retina [90]. **Müller cells** are the principal glial cells of the inner retina that provide structural and metabolic support to the retinal neurons by breaking down glycogen to fuel aerobic energy production in the nerve cells. They also help regulate ion concentrations, participate in removing neural waste products and cellular debris, and protect neurons from exposure to excess neurotransmitters. They span across almost the entire thickness of the retina, as shown in Figure 1.2, playing a key role in maintaining homeostasis and aiding in light transmission [91, 92]. **Astrocytes** are characteristic star-shaped glial cells that support the ganglion cells axons. **Microglia** can be found across the retina associated with the blood vessels, lying in a dormant state, and activated at the time of trauma or inflammation.

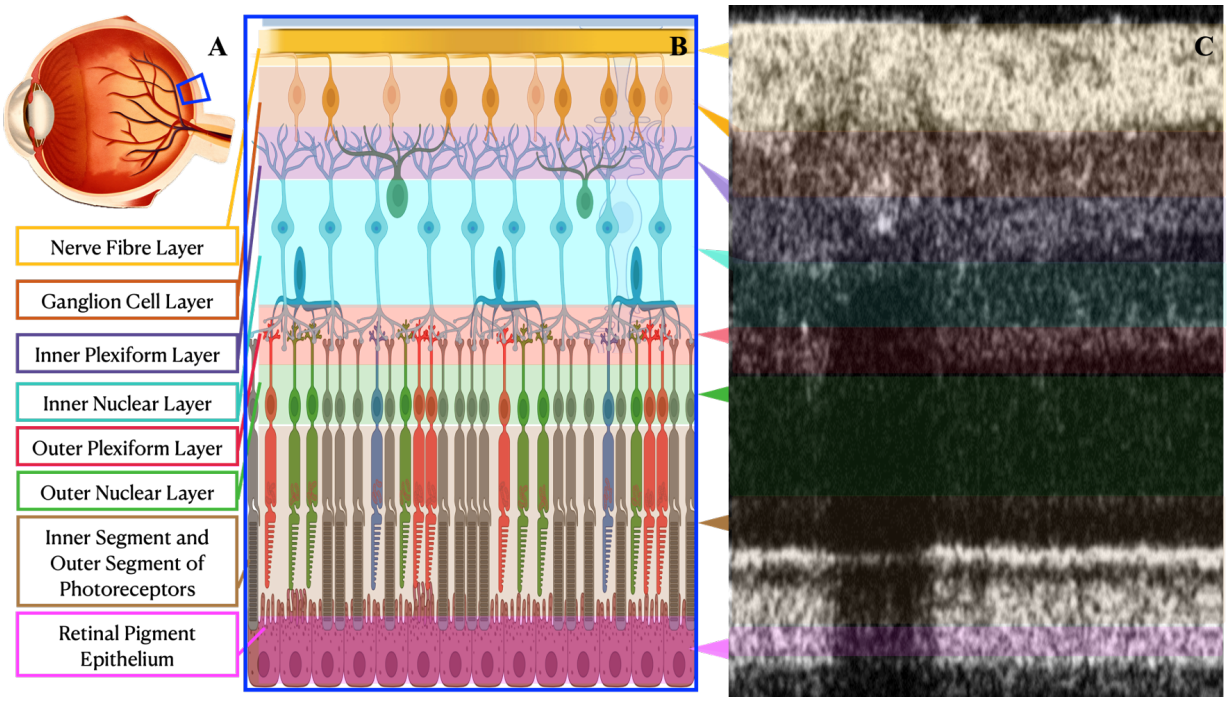


Figure 1.2: (A) The human eye where the blue polygon shows the approximate location of the zoomed in figures B and C. (B) Structure of human retina and the cells forming the different layers of the retina; figure prepared in BioRender, referenced from Kolb *et. al.*, 2005. (C) OCT B-scan showing the different layers in the retina, corresponding to the layers in figure B.

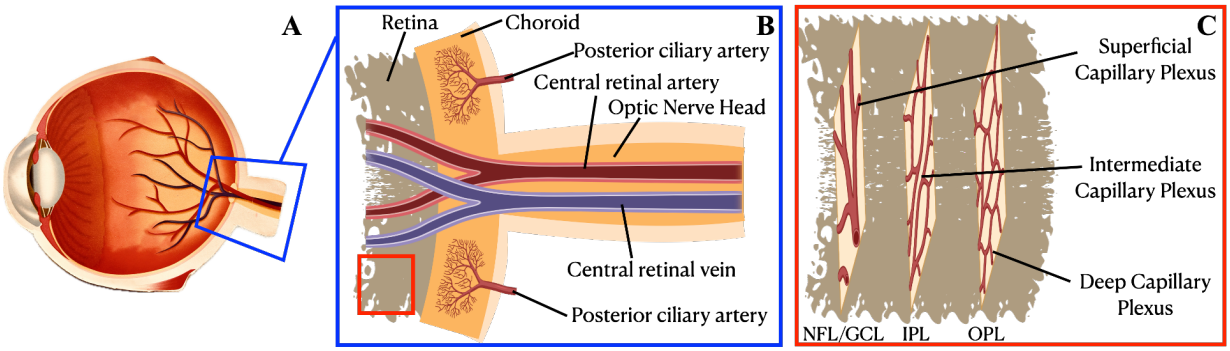


Figure 1.3: (A) The human eye and the blue polygon outlines the Optic Nerve region. (B) Optic Nerve vasculature, showing the central retinal artery and vein nourishing the anterior retina; posterior ciliary arteries nourishing the posterior retina through choroid. (C) Capillary networks in the different retinal layers: Superficial Capillary Plexus in the Nerve Fiber and Ganglion Cell Layers, Intermediate Capillary Plexus in the Inner Plexiform Layer, and Deep Capillary Plexus in the Outer Plexiform Layer of the retina; figure prepared in BioRender.

In addition to serving as the site for neuronal connections, the plexiform layers house beds of capillaries that nourish the retinal cells [8]. These capillaries branch from larger retinal blood vessels, forming the basis of the retinal neurovascular network, a crucial element in neurovascular coupling, which will be explored further in the next section.

1.3 Retinal Blood Flow

The human eye is supported by two primary vascular beds: the Uveal and the Retinal [4]. The uveal vasculature comprises blood vessels from the iris, ciliary bodies, and the choroid, while the vascular supply through the ONH constitutes the retinal vasculature [90, 93]. Retinal vasculature supplies the inner retina via the central retinal artery, whereas the outer retina is nourished through the choroid via the posterior ciliary arteries [94], as shown in Figure 1.3.

When the retina is stimulated by light, 'Retinal' in the photoreceptors absorbs the photon and undergoes a conformational change, initiating a cascade of biochemical signals that transmit visual information to the brain [90, 95]. This activation leads to energy consumption by the cell, thereby causing an energy deficit. To compensate for this energy deficit, the local blood supply increases through a process known as autoregulation [4, 11].

This coupling of increased metabolic demand with increased blood flow, referred to as neurovascular coupling, results in local vasodilation [15, 96]. These vascular changes lead to structural alterations in the retinal tissue, which can be detected using a phase-sensitive imaging system such as OCT [55, 62, 97].

As shown in Figure 1.3, the central retinal artery branches into several large arteries that emerge from the ONH and further divide into three distinct capillary beds within the inner retina: the Superficial Vascular Complex (SVC), the Intermediate Capillary Plexus (ICP) and the Deep Capillary Plexus (DCP) [8,98]. Similarly, the posterior ciliary arteries form a capillary network to nourish the outer retina.

In this thesis, the focus is on the vascular response in the larger blood vessels around the ONH, and surface blood vessels located between the ONH and the fovea. Vascular responses from the posterior ciliary arteries are not discussed in this thesis, since these vessels lie deeper in the tissue, requiring higher wavelength imaging beams to accurately extract RBF changes.

1.4 Thesis Organization

This thesis is structured based on three journal articles, which are either under review or in preparation for submission. The detailed contributions of the thesis author to each article are listed in the 'Statement of Contributions' section of the thesis. Below is an overview of each chapter:

Chapter 2:

- Provides an overview of the OCT technology, outlining its fundamental principle based on low-coherence interferometry;
- Highlights the distinctions between Time-Domain OCT and Fourier-Domain OCT;
- Presents the characteristics of Fourier-Domain OCT;
- Concludes with a brief discussion on electroretinography and optoretinography.

Chapter 3:

- Details the development of a research-grade combined OCT+ERG system and its performance evaluations;

- Discusses capabilities of the system in measuring both retinal blood flow and neuronal activity, leveraging the integrated OCT and ERG systems.

Chapter 4:

- Presents findings on changes in retinal blood flow and blood vessel diameter in healthy human subjects at the Optic Nerve Head in response to 10 Hz white-light flicker stimulation;
- Showcases the system's effectiveness in capturing dynamic vascular responses.

Chapter 5:

- Explores the differential retinal blood flow responses to different wavelengths and flicker frequencies with an aim to isolate responses from specific types of photoreceptors-both rods and cones, or predominantly cones when rod responses are saturated at higher flicker frequencies.

Chapter 6:

- Provides summary of the research conducted during the PhD, highlighting key findings and contributions;
- Also offers a brief discussion on potential future research directions and advancements stemming from this work.

Chapter 2

Optical Coherence Tomography (OCT)

In 1971, Michel Duguay proposed that optical echoes could be used to visualize biological tissues, a groundbreaking concept that laid the foundation for modern biological imaging techniques [99]. Since biological tissues are highly scattering, using an ultrahigh-speed shutter could effectively capture light echoes from within the tissue while minimizing the effects of scattered light [100].

Optical Coherence Tomography (OCT) is based on the principle of low-coherence interferometry, a powerful tool that measures the magnitude and echo time delay of backscattered light [51]. The term 'optical' refers to the use of light as the imaging modality; 'coherence' indicates the significance of the interference using low-coherence light, and 'tomography' is derived from the ancient Greek word *tomos*, meaning 'section', and the Latin word *graphia*, meaning 'representation'. In essence, OCT enables cross-sectional imaging of biological tissues with interference from a low-coherence light source. It is often regarded as the optical equivalent of ultrasound, where sound waves are used to image biological structures.

OCT offers non-invasive, high-speed, cellular-level resolution imaging of biological tissues *in vivo*. It achieves cross-sectional and volumetric imaging by measuring the magnitude and echo time delay of backscattered light [54]. As illustrated in Figure 2.1, the imaging process begins with an A-scan, a one-dimensional depth-resolved reflectivity profile (Z-axis) of the sample at a specific point. Multiple A-scans across the lateral axis (X-axis) are combined to form a two-dimensional intensity image known as a B-scan. Further combining multiple B-scans across different locations results in a three-dimensional volumetric dataset (Y-axis).

This chapter briefly reviews the theoretical foundations of OCT, the different OCT

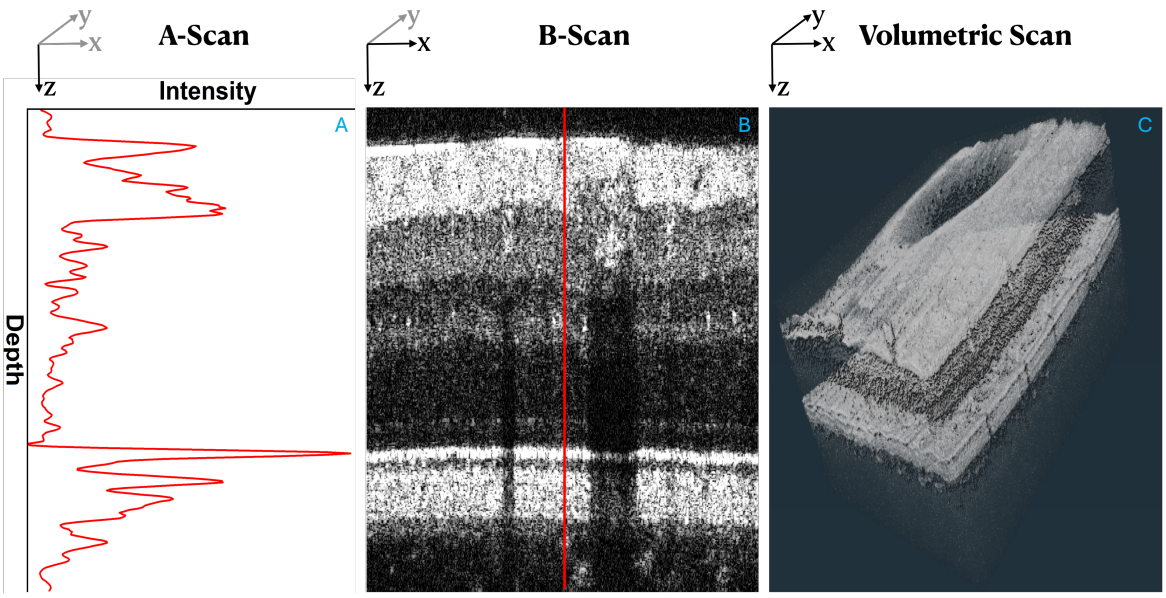


Figure 2.1: (A) A representative OCT A-scan. (B) An OCT B-scan of a human retina generated by combining A-scans. (C) A volumetric OCT scan.

imaging modalities, and the specific techniques employed in this PhD study. Additionally, this chapter also reviews Electroretinography (ERG) and its optical counterpart, Optoretinography (ORG).

2.1 Optical Coherence Tomography: Theory

Figure 2.2 illustrates a simplified schematic of an OCT system, which is based on a Michelson interferometer. In a typical fiber-based OCT system, the light source has an electric field component characterized by:

$$E_i = s\left(k, \omega\right) e^{i(kz - \omega t)}. \tag{2.1}$$

Here, $s\left(k, \omega\right)$ represents the amplitude of the electric field, which is a function of the wavenumber $k = \frac{2\pi}{\lambda}$ and the angular frequency $\omega = 2\pi\nu$. This electromagnetic field is split using a fiber coupler into two arms: the reference arm, where a mirror is placed at the end for back-reflection, and the sample arm, where the sample to be imaged backscatters light

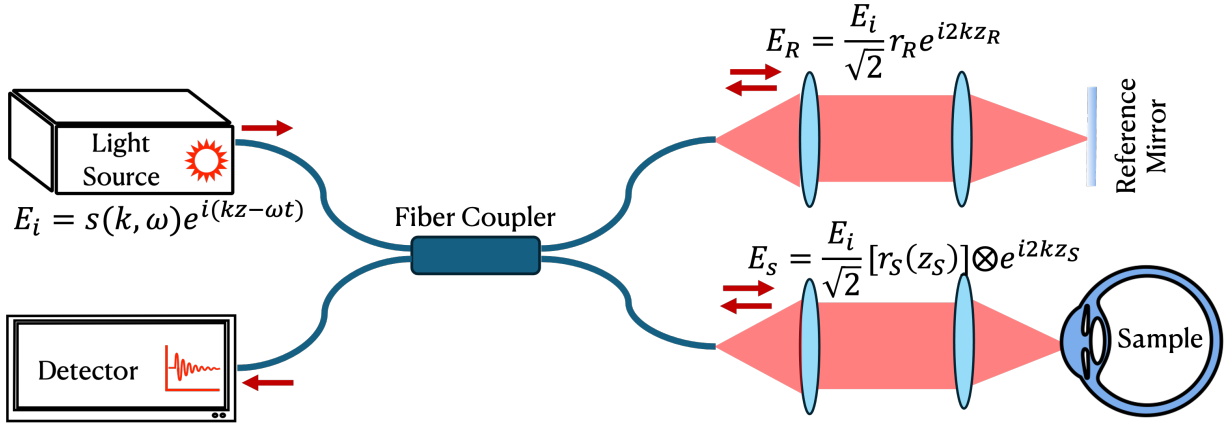


Figure 2.2: A simplified schematic of a fiber-based OCT system based on Michelson Interferometer.

from its different layers, forming an interference pattern at the detector [52,54]. Interference happens when the signal from both arms is within the spatial and temporal coherence. To ensure that, the reference arm is designed to closely resemble the sample arm in terms of path length and dispersion.

Assuming a perfect 50:50 split at the fiber coupler between the reference and the sample arms, the electric field reflected from the reference arm mirror can be expressed as:

$$E_R = E_i \frac{1}{\sqrt{2}} r_R e^{i2kz_R}, \tag{2.2}$$

The field reflected from the sample arm, which depends on the depth of the sample layers, can be expressed as:

$$E_S = E_i \frac{1}{\sqrt{2}} \left(r_S\left(z_S\right) \circledast e^{i2kz_S} \right) \tag{2.3}$$

In the above equations, z_R is the distance of the reflective surface in the reference arm (the mirror) from the beam splitter and z_S is the distance of the multi-layered reflective surfaces in the sample arm from the beam splitter. The terms r_R and $r_S\left(z_S\right)$ represent the electric field reflectivity of the mirror in the reference arm and the multi-layered sample as a function of the individual sample layers, respectively, with $\circledast$ representing convolution and the factor of 2 in the exponential term accounts for the round-trip path length to each

sample reflection. If there are n discrete sample reflectors in the sample arm, $r_S(z_S)$ can be represented using the equation:

$$r_S(z_S) = \sum_{i=1}^{n} r_{S,i}\delta(z_S - z_{S,i}) \tag{2.4}$$

Here, $r_{(S,i)}$ represents the electric field reflectivity of the i-th layer in the sample at a depth $z_{(S,i)}$, and δ is the Dirac Delta function, indicating the position of each layer in the sample.

The combined electromagnetic field from both arms is captured by a square-law detector, which generates a photocurrent proportional to the square of the sum of the electromagnetic fields incident on it:

$$I_D(k,\omega) = \frac{\rho}{2}\left\langle |E_R + E_S|^2 \right\rangle \tag{2.5}$$

This can be expanded to:

$$I_D(k,\omega) = \frac{\rho}{2}\left\langle (E_R + E_S)(E_R + E_S)^* \right\rangle \tag{2.6}$$

In these equations, ρ represents the responsivity of the detector, and the angular brackets represent the integration over the detector response time. Substituting equations (2.2) and (2.3) into equation (2.6) and considering only the real part of the resulting equation, the 'spectral interferogram' is obtained as:

$$\begin{aligned} I(k) = S(k)\Bigg\{ R_R + \sum_{i=1}^{n} R_{S,i} \;\; &+ 2\sum_{i=1}^{n} \sqrt{R_R R_{S,i}}\cos\left[2k(z_R - z_{S,i})\right] \\ &+ \sum_{i,j=1,i\neq j}^{n} \sqrt{R_{S,i}R_{S,j}}\cos\left[2k(z_{S,i} - z_{S,j})\right] \Bigg\} \end{aligned} \tag{2.7}$$

In the above equation, $S(k) = \frac{\rho}{4}\left\langle s(k,\omega)^2 \right\rangle$, and the power reflectivity for any reflector is the magnitude of the square of the respective electric field reflectivity, i.e., $R_R = |r_R^2|$. This equation can be broken down into three main components:

1. **Constant or 'DC' terms**: The first two terms (R_R and $\sum_{i=1}^{n} R_{S,i}$) represent the self-interference from the reference and the sample arms, respectively. The reference arm term, R_R is the largest component of the OCT signal and typically forms the background signal, which is removed from the final data. The sample arm self-interference term, $\sum_{i=1}^{n} R_{S,i}$, is generally negligible due to the lower reflectivity of the sample tissue layers compared to the reference arm mirror.

2. **Cross-correlation term**: The term $2\sum_{i=1}^{n}\sqrt{R_R R_{S,i}}\cos\left[2k\left(z_R - z_{S,i}\right)\right]$ represents the interference between the reference arm and the sample arm reflectivity profiles. This is the primary term used to reconstruct $r_S\left(z_S\right)$ from the low-coherence OCT signal, providing the depth-resolved information needed for imaging.

3. **Auto-correlation term**: The term $\sum_{i,j=1,i\neq j}^{n}\sqrt{R_{S,i}R_{S,j}}\cos\left[2k\left(z_{S,i} - z_{S,j}\right)\right]$ represents the interference between reflections from different layers within the sample itself. This term is negligible when the optical setup and power selection in the sample arm is optimized relative to the reference arm.

2.2 Different designs of OCT systems

Different interpretations of equation (2.7) give rise to the two categories of OCT systems: Time-Domain OCT (TD-OCT) and Fourier-Domain OCT (FD-OCT).

2.2.1 Time-Domain OCT (TD-OCT)

Early OCT systems incorporated a scanning reference arm delay with a low-coherence light source and an interferometer, which are collectively known as the Time-Domain OCT (TD-OCT) systems. In a typical TD-OCT system, the length of the reference arm, z_R, is scanned as a function of time to reconstruct the sample reflectivity profile $r_S\left(z_S\right)$ at different depths. This is typically attained using a linear stage to translate the reference mirror, a piezoelectric actuator-based fiber stretcher, or other mechanisms to generate depth-resolved information along the A-scan direction.

Conventionally, TD-OCT systems achieve A-scan rates on the order of a few kHz, with the performance limited by the signal-to-noise ratio (SNR) due to reduced exposure time and the presence of moving mechanical components such as galvanometer scanners and fiber stretchers [101]. A typical TD-OCT system schematic is shown in Figure 2.3, where a translational reference mirror is employed to obtain depth information.

Assuming the incident light has a Gaussian spectral profile given by:

$$s\left(k\right)=\frac{1}{\Delta k\sqrt{\pi}}e^{-\left(\frac{k-k_0}{\Delta k}\right)^2}, \tag{2.8}$$

where $k_0=\frac{2\pi}{\lambda_0}$ is the central wavenumber, and Δk is the spectral half-width at $\frac{1}{e}$ intensity. Integrating equation (2.7) over all values of k, the resulting photocurrent is given by:

$$I_D\left(z_R\right)=\frac{\rho}{4}\left[s_0\left(R_R+\sum_{i=1}^{n}R_{S,i}\right)\right]+\frac{\rho}{2}\left[s_0\sum_{i=1}^{n}\sqrt{R_RR_{S,i}}e^{-\left(z_R-z_{S,i}\right)^2\Delta k^2}\cos\left(2k_0\left(z_R-z_{S,i}\right)\right)\right] \tag{2.9}$$

Here, $s_0=\int_0^\infty s\left(k\right)dk$ is the spectrally integrated power emitted by the light source. The first term in the equation corresponds to the 'DC offset', while the second term corresponds to the cross-correlation term or 'fringe bursts'. The exponential decay term, $e^{-\left(z_R-z_{S,i}\right)^2\Delta k^2}$, suggests that the interference signal peaks when $z_R=z_{S,i}$ and quickly diverges as the path length difference increases. The signal width is determined by the Fourier transform of $s\left(k\right)$.

2.2.2 Fourier-Domain OCT (FD-OCT)/Spectral-Domain OCT (SD-OCT)

An alternative to TD-OCT is the Fourier-Domain OCT (FD-OCT), which provides much higher acquisition speeds and improved system sensitivity. In FD-OCT, instead of mechanically scanning the reference arm, the reflectivity profile $r_S\left(z_S\right)$ is reconstructed by applying a Fourier Transform to the measured detector signal $I_D\left(k\right)$, avoiding the need for moving components and therefore, the integral over the wavenumbers.

By using the Fourier Transform pair $\frac{1}{2}\left(\delta\left(z+z_0\right)+\delta\left(z-z_0\right)\right)\overset{\mathcal{F}}{\longleftrightarrow}\cos\left(kz_0\right)$ and the convolution property of the Fourier Transforms $x\left(z\right)\circledast y\left(z\right)\overset{\mathcal{F}}{\longleftrightarrow}X\left(k\right)Y\left(k\right)$, the inverse Fourier Transform of equation 2.7 gives:

$$\begin{aligned}i_D\left(z\right)=&\frac{\rho}{8}\left[\gamma\left(z\right)\left[R_R+\sum_{i=1}^{n}R_{S,i}\right]\right]+\frac{\rho}{4}\left[\gamma\left(z\right)\circledast\sum_{i=1}^{n}\sqrt{R_RR_{S,i}}\left(\delta\left(z\pm2\left(z_R-z_{S,i}\right)\right)\right)\right]\\&+\frac{\rho}{8}\left[\gamma\left(z\right)\circledast\sum_{i,j=1,i\neq j}^{n}\sqrt{R_{S,i}R_{S,j}}\left(\delta\left(z\pm2\left(z_{S,i}-z_{S,j}\right)\right)\right)\right]\end{aligned} \tag{2.10}$$

Here, $\gamma(z)$ is the Fourier Transform of the power spectral density function $s(k)$. The first term corresponds to the 'DC offset', the second term is the 'cross-correlation' signal and the third term is the 'auto-correlation' signal. The cross-correlation term gives the desired sample reflectivity profile $r_S(z_S) = \sum_{i=1}^{n} \sqrt{R_{S,i}}\delta(z_S - z_{S,i})$. Taking advantage of the sifting property of the delta function for the cross-correlation term:

$$i_{CC}(z) \propto \sum_{i=1}^{n} \sqrt{R_R R_{S,i}} \{\gamma[2(z_R - z_{S,i})] + \gamma[-2(z_R - z_{S,i})]\} \tag{2.11}$$

Equation (2.11) contains information from all the discrete sample layers within the scanning range forming an A-scan, therefore eliminating the need to include mechanical components to change the optical path.

However, a mirror image of the sample reflectivity profile appears on the other side of the zero path length, manifested in the terms $\gamma[2(z_Z R - z_{S,i})]$ and $\gamma[-2(z_Z R - z_{S,i})]$, where they differ only in the sign. As long as the sample remains on one side of the zero path length delay, this artifact is not disabling. Additional image artifacts also arise from the DC and the auto-correlation terms, which can be best eliminated by subtracting the background signal and ensuring that the reference reflectivity is sufficient.

FD-OCT requires a resolved interference k-spectrum to obtain the Fourier Transform, which is typically achieved by two methods:

1. **Spectral-Domain OCT (SD-OCT)**: This approach uses a broadband light source in combination with a spectrometer and line detector. The spectrometer in front of the camera separates the continuous emission (CW) from the broadband light source into individual wavelengths, allowing all spectral components to be detected simultaneously.

2. **Swept-Source OCT (SS-OCT**: In this approach, a tunable-wavelength light source sequentially sweeps a narrow band of the spectrum over time, with the signal detected using a single detector.

Both of these approaches fall under the FD-OCT category, and a typical system schematic is described in Figure 2.3.

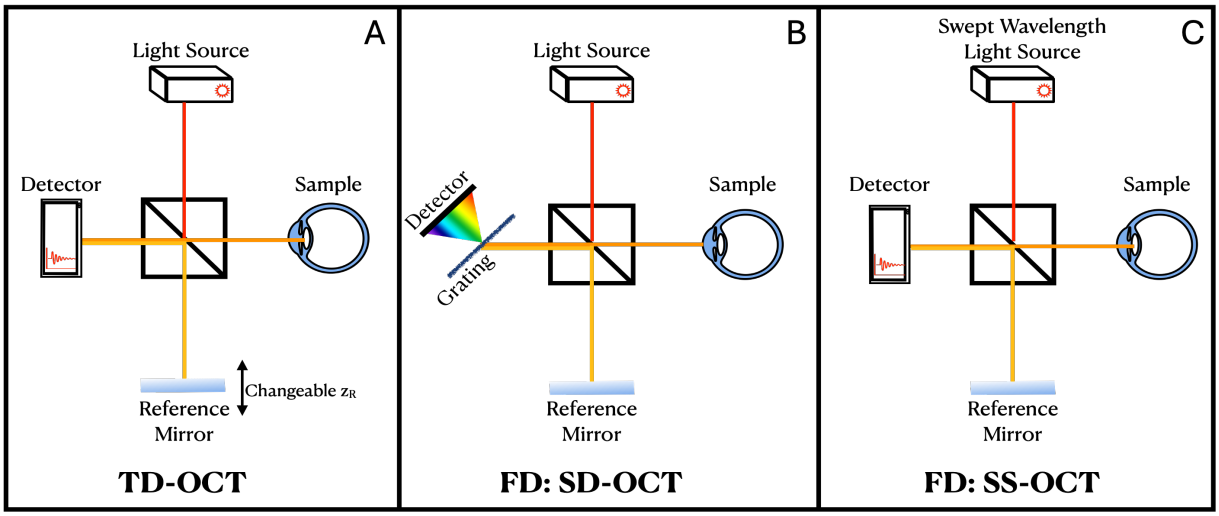


Figure 2.3: (A) A simplified schematic for Time-Domain OCT system with a translational reference mirror. (B) A simplified schematic of the Spectral-Domain OCT system with a spectrometer and a line detector. (C) A simplified schematic of the Swept-Source OCT system with a swept-wavelength light source.

2.3 OCT imaging modalities

OCT systems can be classified into three categories based on the scanning types: point-scan OCT (PSc-OCT), line-scan OCT (LS-OCT), and full-field OCT (FF-OCT). Figure 2.4 illustrates these approaches, highlighting their differences in the beam shapes at the image plane. For simplicity, we assume that each of these systems uses the FD-OCT approach with a microscopic objective to focus light on the sample. Although these modalities are also applicable to TD-OCT, FD-OCT has become the predominant method in recent years and is also the method employed in this thesis.

PSc-OCT refers to an OCT system that acquires one A-scan (depth scan) at a time by focusing a narrow, confocal beam at each location in the sample. This point-by-point scanning reduces cross-talk and enhances image quality compared to other OCT modalities with similar system SNR. A single camera exposure (in an SD-OCT system) or full spectrum sweep (for SS-OCT) generates one A-scan, and scanning mirrors (or micro-electromechanical system (MEMS) mirrors) move the beam in the XY plane to construct a 3D dataset. The flexibility of two scanning mirrors allows for customizable scanning patterns, such as circular scans, which are valuable in functional studies [62]. However, due to individual A-scan acquisition, PSc-OCT systems are generally slower in terms of data

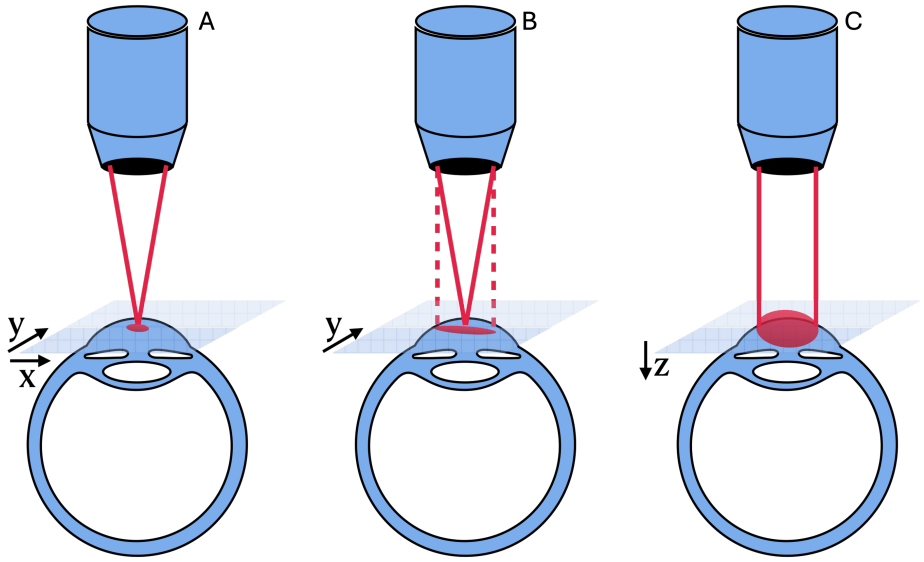


Figure 2.4: (A) Shape of the beam in imaging plane in PSc-OCT system. (B) Beam shape at the imaging plane in LS-OCT system. (C) Beam shape at the imaging plane in FF-OCT system.

acquisition as compared to the LS-OCT and FF-OCT systems. Researchers have reported A-scan rates of up to 600 kHz for an SD-PSc-OCT system [102–104] and 5.2 MHz for an SS-PSc-OCT [105] using high-speed line cameras and special light sources, respectively. However, clinical systems typically operate at around 100 kHz, which poses challenges for larger Field-of-View (FOV) imaging due to potential artifacts from involuntary body movements.

LS-OCT, also known as Line-Field OCT (LF-OCT), refers to an OCT system that captures all lateral positions in a cross-sectional image (B-scan) simultaneously. First demonstrated in 1999, LS-OCT utilizes a 2D lens to convert a circular-shaped beam into a line-shaped beam [106], limiting the confocality to one direction. This means that the imaging beam projected onto the sample arm is a straight line, enabling parallel acquisition of depth data along the line using a 2D sensor (for SD-OCT) or line camera (for SS-OCT). LS-OCT reduces motion artifacts related to eye or body movements, though its FOV in the B-scan direction is limited due to energy redistribution along the line. Recent advancements in LS-OCT methods have enabled data acquisition rates equivalent to A-scan rates of several MHz [107–112]. While LS-OCT provides faster data acquisition than PSc-OCT, its beam shape restricts the data acquisition only to volumetric raster scanning

and does not allow for circular, Lissajous or radial scanning patterns which maybe useful for some biomedical applications.

Full-field OCT (FF-OCT) systems acquire one *en face* image at a time, typically using TD-system [113]. Unlike PSc-OCT and LS-OCT systems, FF-OCT does not capture depth information at the same time. A parallel beam is projected onto the sample, generating a single *en face* image per exposure. FF-OCT systems are not viable for SD-OCT systems due to the need for a 3D sensor to simultaneously capture 2D spatial and 1D spectral information. As a result, FF-OCT systems typically employ either TD or SS configurations to obtain volumetric images. A key advantage of FF-OCT is its independence from depth-of-focus limitations associated with beam focusing, allowing the use of high-numerical-aperture (NA) objectives to achieve cellular-level lateral resolution across the entire scanning depth. However, cross-talk is a common challenge in FF-OCT due to the lack of confocality in either direction, therefore techniques such as random phase modulations and multi-mode fibers (e.g., spatio-temporal optical coherence tomography, STOC-T) have been developed to address this issue [114, 115]. FF-OCT systems capable of achieving speeds up to 1.5 million A-scans per second have been reported [116–120].

Given the need for customizable scanning profiles in this research, a PS-OCT system was used to conduct this PhD study.

2.4 Characteristics of an FD-OCT system

This section outlines key characteristics of a typical FD-OCT system that are necessary for assessing its performance. The characteristics discussed here are based on a PSc-OCT system with a normalized Gaussian beam profile. The field amplitude for the beam is given by equation 2.8. This Gaussian profile provides a foundational model for understanding the beam behavior and resolution in OCT imaging.

2.4.1 Axial Resolution

The axial resolution of an OCT system represents its theoretical limit to resolve two distinct points along the axial (depth) direction of a sample. Unlike other OCT system parameters, axial resolution is solely determined by the profile of the light source and is independent of the physical setup of the system. Taking the Fourier Transform of the field amplitude $s(k)$ yields:

$$\gamma(z) = \mathcal{F}\{s(k)\} = e^{-z^2\Delta k^2} \tag{2.12}$$

This result, known as the 'coherence function', defines the coherence length (l_c), or axial resolution, of the OCT system. The axial resolution is given by the full-width at half maximum (FWHM) of the coherence function:

$$l_c = \delta_z = \frac{2\sqrt{ln(2)}}{\Delta k} = \frac{2ln(2)}{\pi}\frac{\lambda_0^2}{\Delta\lambda} \tag{2.13}$$

Here, $\lambda_0 = \frac{2\pi}{k_0}$ is the central wavelength of the light source, and $\Delta\lambda$ is the bandwidth of the spectrum, defined as the FWHM of the wavelength spectrum. In terms of Δk, we have:

$$\left(\Delta k = \frac{\pi}{\sqrt{ln(2)}}\frac{\Delta\lambda}{\lambda_0^2}\right). \tag{2.14}$$

For light sources with non-Gaussian beam profiles, this axial resolution calculation serves as an estimate; a more precise measure can be obtained by taking the Fourier Transform of the actual beam profile.

2.4.2 Lateral Resolution

The lateral resolution of an OCT system is typically described as the focused spot size formed by the beam waist of a Gaussian beam incident on the sample. Since an OCT system has a confocal component, the theoretical lateral resolution (δ_x) can be analyzed by treating the light propagation through a confocal microscope. The intensity detected at the focal plane can be described by:

$$I(v) = \left(\frac{2 \cdot J_1(v)}{v}\right)^4 \tag{2.15}$$

Here, $J_1(v)$ is the first-order Bessel function of the first kind and v is the normalized lateral range parameter, which is defined by:

$$v = \frac{2\pi x \sin(\alpha)}{\lambda_0}. \tag{2.16}$$

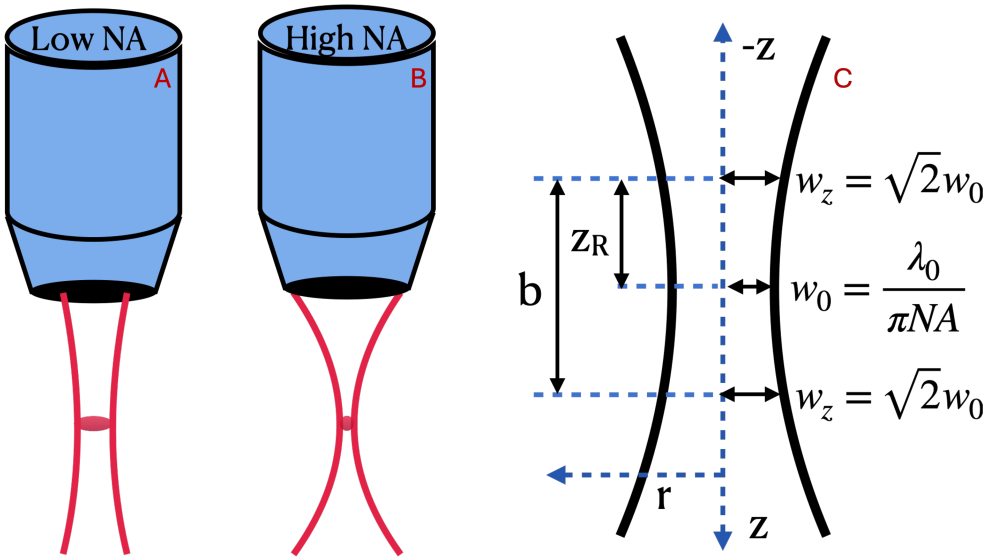


Figure 2.5: (A) Low NA objective creates a larger beam waist. (B) A high NA objective creates a smaller beam waist. (C) Gaussian beam profile near the focal plane depicting the beam characteristics.

In this expression, x represents the lateral distance from the optical axis, α is the half-angular aperture of the objective, and λ_0 is the central wavelength. The numerical aperture of the objective is given by $NA = \sin(\alpha)$. The lateral resolution, defined as the FWHM of the beam width at the focal plane, is given by the following equation:

$$\delta_x = \frac{\sqrt{2ln\,(2)}}{\pi}\frac{\lambda_0}{sin\,(\alpha)} \approx 0.37\frac{\lambda_0}{\sin(\alpha)} = 0.37\frac{\lambda_0}{NA} \tag{2.17}$$

Since the lateral resolution is inversely related to the numerical aperture, higher NA objectives result in smaller focal spot sizes and improved lateral resolution, shown in Figure 2.5.

It is important to note that lateral resolution depends only on the central wavelength λ_0 and not on the bandwidth. Therefore, for narrow-band systems, calculations based on the spectral central wavelength provide a reasonable approximation of lateral resolution, though this may not hold for broadband input spectra.

2.4.3 Depth of Focus

The Rayleigh range, or the Rayleigh length (z_R), is defined as the distance along the propagation direction from the focal plane to the point where the beam's cross-sectional area doubles, or where the intensity falls to $\frac{1}{e^2}$ of its maximum at the beam waist. It is given by the following relation:

$$Z_R = \frac{\pi w_0^2}{\lambda} = \frac{1}{\pi}\frac{\lambda_0}{NA^2}. \tag{2.18}$$

where w_0 is the beam waist, λ_0 is the central wavelength, and NA represents the numerical aperture of the objective lens.

Assuming a Gaussian beam with an intensity profile given by:

$$I\left(r\right) = I_0 e^{-frac2r^2 w(z)^2} \tag{2.19}$$

z in the above equation is the propagation axis, r is the radial distance from the axis, and $w\left(z\right)$ represents the beam radius at which the intensity falls to $\frac{1}{e^2}$ of I_0.

The depth of focus (DOF), also known as the confocal parameter (b), is twice the Rayleigh range, indicating the depth over which the beam maintains enough intensity to remain in focus. The DOF is calculated as follows:

$$DOF = b = 2Z_R = \frac{2\pi w_0^2}{\lambda_0} = \frac{2\lambda_0}{\pi NA^2} \tag{2.20}$$

For a Gaussian beam, a higher numerical aperture results in a smaller beam waist and consequently a shorter DOF, while a lower NA results in a longer DOF. This relationship is illustrated in Figure 2.5.

2.4.4 Digital Resolution

The digital resolution ($\tilde{\delta}$) of an OCT system refers to the effective resolution of each pixel, determined by the ratio of the field of the view (FOV) for an image and the number of pixels spanning that FOV. Since OCT systems have separate axial and lateral resolutions, the digital resolutions for each direction are also described independently.

The digital axial resolution ($\tilde{\delta_z}$) of an OCT system is given by:

$$\tilde{\delta_z} = \frac{z_{max}}{\frac{N}{2}} = \frac{1}{2\left(\frac{1}{\lambda_{min}} - \frac{1}{\lambda_{max}}\right)} \tag{2.21}$$

where z_{max} represents the maximum depth range, N is the total number of camera pixels used for spectral detection, and the $\frac{1}{2}$ factor accounts for the mirror artifact from the Fourier Transform.

The digital lateral resolution ($\tilde{\delta_x}$) is defined by:

$$\tilde{\delta_x} = \frac{FOV_x}{N_x} \tag{2.22}$$

where FOV_x represents the lateral field of view in the (x) direction and N_x is the number of pixels in that direction (i.e., the number of A-scans). Similarly, the digital resolution in the y-direction is defined by the FOV in the y-direction divided by the number of B-scans.

According to the Nyquist-Shannon sampling theorem, the digital resolution of the OCT system should be at least half the actual resolution to prevent aliasing and accurately capture the image detail.

2.4.5 Scanning Range

From equation 2.7, it can be seen that the auto-correlation term exhibits a sinusoidal function in the form $\cos\left[2k\left(z_R - z_{S,i}\right)\right]$. As the difference in optical path length increases, so does the frequency of the interference fringe. In OCT systems, where the detector has a finite number of pixels, the Nyquist-Shannon sampling theorem applies, which states that the sampling frequency should be at least twice the detected frequency to avoid aliasing.

For an OCT system with an N-pixel detector and a broadband light source with spectral width Δk, the Nyquist-Shannon theorem sets the following condition to avoid aliasing:

$$2\Delta k\left(z_R - z_{S,i}\right) \leq \frac{N}{2} \times 2\pi \tag{2.23}$$

Setting both sides of the above inequality equal yields the maximum scanning range (z_{max}) for the OCT system:

$$2\left(k_{max} - k_{min}\right) z_{max} = N\pi \tag{2.24}$$

Rearranging this equation gives:

$$Z_{max} = \frac{N\pi}{2\left(k_{max} - k_{min}\right)} = \frac{N}{4}\frac{1}{\left(\frac{1}{\lambda_{min}} - \frac{1}{\lambda_{max}}\right)} \tag{2.25}$$

Here, k_{max} and k_{min} denote the upper and lower limits of the wavenumber range of the light source, while λ_{min} and λ_{max} represent the corresponding minimum and maximum wavelengths. This expression defines the maximum achievable depth range for an OCT system given its pixel count and spectral properties.

2.4.6 Signal to Noise Ratio (SNR)

As the name implies, the Signal-to-Noise Ratio (SNR) is the ratio of the actual signal to the noise detected by the detector. For an OCT system, it is defined as:

$$SNR = \frac{\langle I_D \rangle^2}{\sigma^2} \tag{2.26}$$

where $\langle I_D \rangle^2$ is the power of the mean-square peak signal on the detector, and σ^2 represents the noise variance. If only the zero-delay signal is considered (i.e., $z_R = z_S$), the cross-correlation intensity term from equation 2.7 can be expressed as:

$$I_D \propto \rho\left(k\right) s^2\left(k\right) \sqrt{r_R r_S} \tag{2.27}$$

If the detector has a quantum efficiency η and an integration time τ, this equation can be further rearranged as:

$$I_D = \frac{\eta\tau}{h\nu} s^2\left(k\right) \sqrt{r_R r_S} \tag{2.28}$$

where h is the Planck's constant, and ν is the frequency of the photons. Assuming a shot-noise-limited system, the noise at the detector is dominated by the back-reflection from the reference arm mirror, and the noise variance follows Poisson distribution as:

$$\sigma^2 = \frac{\eta\tau}{h\nu} s^2\left(k\right) r_R \tag{2.29}$$

Combining these equations yields the following expression for the SNR:

$$SNR = \frac{\eta\tau}{h\nu} s^2(k)\, r_S = \frac{\eta\tau P_S}{h\nu} \tag{2.30}$$

The above equation describes the SNR of an OCT system, assuming a perfect detector with no additional noise sources. However, according to the Nyquist-Shannon sampling theorem, high-frequency interference fringes may not be detected as effectively with a detector that has a limited number of pixels, thereby reducing the system's SNR, the phenomenon known as 'SNR roll-off'.

In typical imaging systems, sensitivity is defined as the smallest signal that can be distinguished from noise. However, in this thesis, the terms 'SNR' and 'sensitivity' will be used interchangeably.

2.5 Doppler OCT

When an electromagnetic wave interacts with moving particles, the backscattered wave experiences a frequency shift, a phenomenon known as Doppler frequency shift. This shift in frequency occurs due to the relative motion between the incident optical beam and the moving particles and can be expressed by the following relation:

$$f_D = \frac{1}{2\pi}(\vec{k_i} - \vec{k_s}) \cdot \vec{v} \tag{2.31}$$

Here, $\vec{v}$ is the velocity of the moving particles, and $\vec{k_i}$ and $\vec{k_s}$ are the wavevectors of the incident and the reflected beams, respectively. Since the Doppler frequency shift is directly proportional to the velocity of the moving particles, rearranging the above equation allows the determination of velocity from the measured frequency shift.

Doppler OCT utilizes this principle to measure the velocity of blood corpuscles, with the electromagnetic field generated by the imaging light source [61, 66], as depicted in Figure 2.6. In FD-OCT, the Doppler frequency shift, f_D, manifests as a phase shift $\Delta\phi$ in the spectral interference pattern detected by the line-scan detector. A Fourier Transform is then applied to calculate the Doppler Shift by measuring the phase difference between sequential A-scans at each pixel [60, 121]. This shift in the detected signal can be used to measure the velocity of the blood particles, while the morphological images from OCT can help determine the blood vessel diameter. Since blood flow is the product of blood velocity and the cross-sectional area of the blood vessel, Doppler OCT enables the quantification of blood flow *in vivo*.

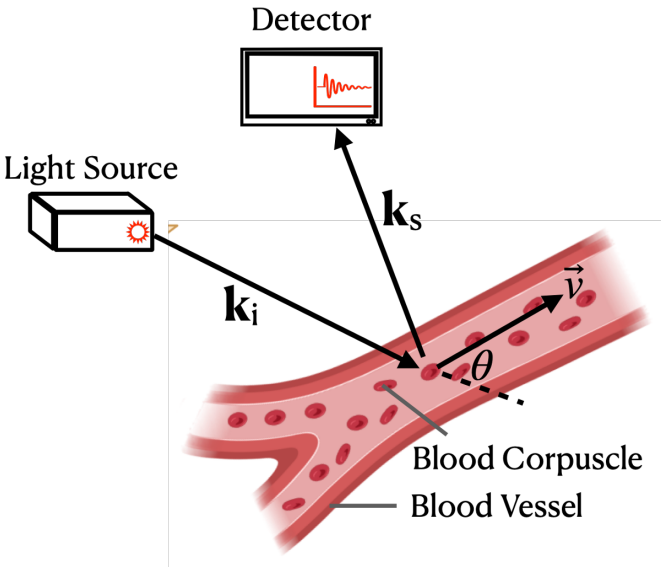


Figure 2.6: A schematic of back-scattering geometry for Doppler OCT, depicting the Doppler angle θ between the incident beam and the blood corpuscle velocity.

Simplifying equation 2.31 gives the following relation for Doppler frequency shift:

$$f_D = \frac{2nv_z}{\lambda_0} \tag{2.32}$$

Here, n is the refractive index of the medium, λ_0 is the central wavelength of the imaging beam, and v_z is the blood velocity component along the propagation direction of the incident beam. This velocity component v_z is given by:

$$v_z = |\vec{v}|\cos\theta \tag{2.33}$$

θ, here, is the Doppler angle, defined as the angle between the incident beam and the direction of blood flow. Accurate determination of this angle is essential for calculating absolute retinal blood flow (RBF). *In vivo*, a double circular scanning protocol around the Optic Nerve Head (ONH) can be employed to estimate this angle, as described in the next section.

Alternative scanning protocols, such as the rectangular scanning method [122], allow for manual selection of scan positions from volumetric or *en face* images to avoid vessel

bifurcations or pronounced vessel curvatures. However, this method may not always permit accurate retinal blood flow extraction due to the Doppler angle's variability. Furthermore, human error can affect the accuracy of this protocol. System modifications that introduce an additional imaging beam to the system have been developed to make RBF measurements independent of the Doppler angle. While promising, these approaches require specialized hardware to obtain total retinal blood flow (TRBF) [64].

The application of the Doppler effect in measuring retinal blood flow has an inherent limitation, as the maximum determinable Doppler shift is given by [55, 57, 61]:

$$f_D = \frac{1}{2\tau} \tag{2.34}$$

where τ is the time resolution of the sequential A-scans. Substituting this value into equation 2.32 gives the maximum detectable velocity as:

$$v_{max} = \frac{\lambda_0}{4n\tau \cos\theta} \tag{2.35}$$

The minimum detectable velocity, on the other hand, is limited by the phase noise of the OCT system.

2.5.1 Double circular Scanning protocol

To accurately determine absolute RBF and measure changes in response to external stimulation, the angle between the imaging beam and the blood vessels plays a crucial role. If the beam is perpendicular to the blood vessel, no Doppler shift would be detected as governed by the $\cos\theta$ dependence.

The double circular scanning protocol, developed by Wang *et. al.*, acquires OCT data using two concentric circles around the ONH [62]. This ensures that the imaging beam intersects through all major blood vessels supplying the inner retina. Because this protocol does not require any additional equipment or system modifications, it is highly adaptable to point-scan OCT systems, which are widely used in clinical settings.

When the OCT imaging beam scans in a circular pattern on the retina, it traces a cone. By scanning in double concentric circles with radii r_1 and r_2, two cones are projected onto the retina, cross-sectioning each blood vessel at two locations with co-ordinates $S_1(r_1, \Theta_1, z_1)$ by the inner cone and $S_2(r_2, \Theta_2, z_2)$ by the outer cone as shown in Figure 2.7. The blood vessel vector $\vec{R_b}$ can be described as:

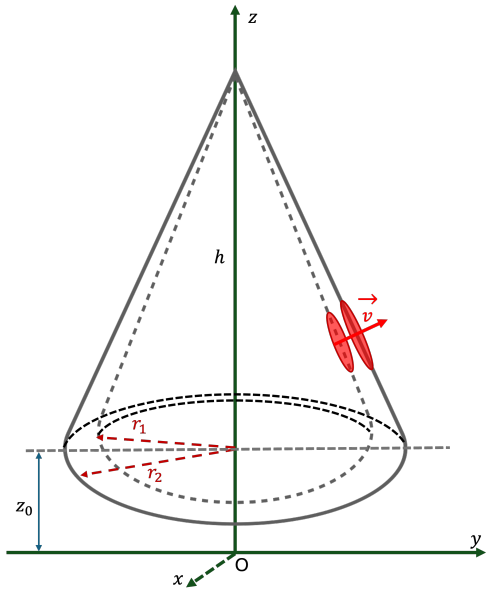


Figure 2.7: Schematic depicting the geometry of the concentric circular scanning protocol across the retina, cross-sectioning a blood vessel at two locations.

$$\vec{R_b} = (r_1 \cos\Theta_1 - r_2 \cos\Theta_2, r_1 \sin\Theta_1 - r_2 \sin\Theta_2, z_1 - z_2), \tag{2.36}$$

This vector describes the orientation of the blood vessel between the two circular scans. The Doppler angle θ can then be calculated using geometry. Setting a coordinate system such that the nodal point of the cone has coordinates $(0, 0, h + z_0)$ and at a scanning point P on the retina with coordinates $(r\cos\Theta, r\sin\Theta, z_0)$, the vector of the scanning beam $\vec{S}$ would be given by:

$$\vec{S} = (r\cos\Theta, r\sin\Theta, -h), \tag{2.37}$$

where z_0 is the distance between the origin of the coordinate system and the retinal plane, and h is the distance from the nodal point of the cone to the retina. Therefore, the Doppler angle θ between the OCT imaging beam and blood vessel can be determined by:

$$\cos\theta = \frac{(\vec{R_b} \cdot \vec{S})}{|R_b||S|} \tag{2.38}$$

Here, the magnitudes $|R_b|$ and $|S|$ represent the lengths of the blood vessel and the beam vectors, respectively. By choosing a small difference between the radii r_1 and r_2, the radius r for the scanning point P is approximated as $r = \frac{(r_1+r_2)}{2}$.

Once the Doppler angle is determined, the absolute value of retinal blood velocity can be used to calculate the average volumetric flow $\bar{F}$ over the period (T) of one cardiac cycle as:

$$\bar{F} = |\cos\alpha| \sum_{S} r A_p \Delta\Theta \Delta D \cdot \frac{1}{T} \int_0^T P(t)dt \tag{2.39}$$

Here, $\cos\alpha = \frac{\vec{S}\cdot\vec{R_b}}{|R_b|}$, α is the angle between the blood vessel cross-section and the OCT plane, A_p is the speed distribution of blood flow in the vessel, $\Delta D = D_1 - D_2$ is the difference between the z-axis locations of the blood vessel cross-sections in the two unwrapped circular scans, and $k = \frac{1}{T}\int_0^T P(t)dt$ represents the cardiac pulsation factor.

2.6 Electroretinography (ERG)

Electroretinography (ERG) measures the electrical response of the retinal neurons to visual stimulation. The first ERG was recorded in 1865 by Swedish physiologist Alarik Holmgren on an amphibian retina [90,123]. Today, ERG is a routine clinical practice used to diagnose various eye diseases and study retinal function, with the potential to isolate individual cell-type responses. Although minimally invasive, ERG can distinguish cellular responses based on the type of stimulation used and the environmental conditions to a certain extent.

A typical ERG setup has a recording electrode, a reference electrode, and a ground electrode. The recording ERG electrode is placed on the surface of the cornea to measure the retinal electrical activity, while the reference and ground electrodes are positioned on the forehead and behind the ear lobe, respectively, after adequately prepping the skin. These electrodes are connected to an amplifier, that amplifies the difference between the recording and the reference electrodes. In this thesis, ERG traces were obtained *in vivo* from healthy human eyes by gently placing a positive electrode under the eyelid, ensuring no obstruction to the simultaneous OCT imaging.

When a photoreceptor in the retina is stimulated, it generates an electrical current due to fluxes (K^+, Na^+ and Ca^{2+}) through a process called phototransduction [95]. Since vertebrate photoreceptors are stacked in parallel, the horizontal component of the current cancels out, leaving only the radial component of the current, which is transmitted through

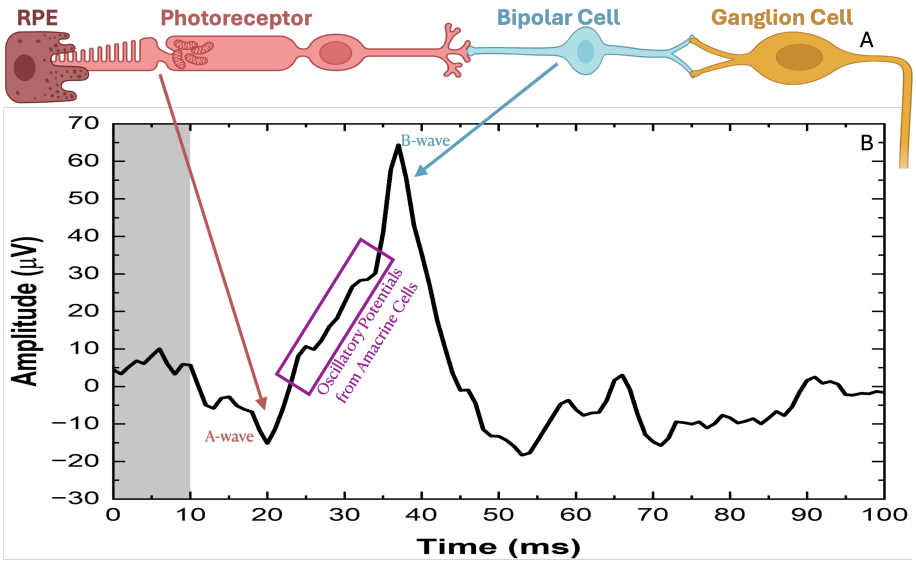


Figure 2.8: (A) Neuronal unit of the retina, showing from left the retinal pigment epithelium cell, a cone photoreceptor, a bipolar cell and a retinal ganglion cell; figure prepared in BioRender. (B) A standard ERG trace showing a-wave, b-wave, and the oscillatory potentials and the cells these responses originate from.

the inner retinal cells, such as bipolar cells, retinal ganglion cells, horizontal cells, amacrine cells, and Müller cells. This radial current is detected by the ERG electrode.

A typical ERG response triggered by a single short flash consists of a fast negative deflection called the A-wave, followed by a positive peak called the B-wave, and a slower positive wave called the C-wave. Longer visual stimulation elicits an additional response, the D-wave, which arises from different types of cell responses as described below.

A-wave: This fast negative response originates from the photoreceptors (both rods and cones) in the outer retina, as the flash interrupts the dark current. The A-wave reflects the function of the outer retina.

B-wave: The first positive peak following the A-wave arises from the integrated response from different types of cells in the Inner Nuclear Layer such as the Müller cells and the ON bipolar cells. The B-wave reflects on the function of the middle retina. Its amplitude is measured as the voltage difference between the A- and the B- waves.

C-wave: A slower positive wave that arises from the basal cells of the Retinal Pigment Epithelium in the outer retina. It is associated with the regeneration of photoreceptors and appears after the B-wave as shown in Figure 2.8.

D-wave: This response occurs in ERG traces with longer stimulation (typically $>$ $100ms$) and reflects the activity of the OFF bipolar cells in response to the cessation of visual stimulation.

Oscillatory Potentials (OPs): High-frequency oscillations superimposed on the rising B-wave, OPs typically originate from the inner retinal cells such as the amacrine cells, and provide insight into the inner retinal health as well as vascular supply. OPs can be isolated from the ERG response by applying a band-pass or a high-pass filter.

Although ERG is the clinical gold standard and is routinely used to assess retinal function, it has some limitations. It is invasive, lacks a clear distinction between the different cell responses, and requires extensive protocols to isolate responses from specific cell types. Moreover, ERG only provides the electrical response of the tissue. In contrast, OCT is non-contact, non-invasive, and offers high-resolution imaging that can capture structural, functional, and physiological responses simultaneously. Given the complementary strengths of ERG and OCT, obtaining simultaneous functional OCT and ERG responses can provide a more comprehensive view of retinal cellular responses.

In this thesis, small-duration single flashes ($< 10ms$) or flicker stimulation at $10Hz$ or $30Hz$ for a duration of $1s$ are used to study the functional retinal responses in healthy human subjects. Therefore, the analysis focuses on the negative A-wave and the first positive B-wave.

2.7 Optoretinography (ORG)

Optoretinography (ORG) refers to a group of optical imaging techniques that detect light-evoked intrinsic optical changes, such as the optical path length (OPL) and/or intensity variations, in the light backscattered from the retinal tissue. ORG is considered the optical analog of ERG, as both measure retinal activity, though ORG captures optical rather than electrical responses [82].

In the early 1990s, Stepnoski *et. al.* demonstrated that neuronal impulses initiate an electrical activity in tissues, leading to changes in the refractive index [124]. These refractive index changes alter the optical properties of the tissue, which can be measured using optical systems such as OCT and SLO.

The first reports of intrinsic optical signal (IOS) changes in the retina came from Bizheva et. al. [89] about two decades ago in 2006. They initially called the technique 'Optophysiology', which later evolved into what we now call 'Optoretinography' (ORG). Early studies

were conducted *ex vivo* using Time-Domain OCT to detect intensity-based IOS changes in frog [125] and rabbit retinas [89]. More recent advances have enabled *in vivo* ORG studies in both animal models and human subjects through the use of Fourier-Domain OCT, which allows for more detailed and rapid data acquisition [73, 75–81, 83, 84, 86–88, 126–128].

The adoption of Line-Scan OCT and STOC-T has made a significant improvement in phase stability and motion artifacts due to the parallel acquisition of B-scans. Integrating Adaptive Optics (AO) has further enhanced the spatial resolution, allowing more precise imaging of the retinal layers and structures [76, 78, 83, 84, 88].

Typically, the retinal intrinsic signals can be categorized into fast signals and slow signals. **Slow signals** are generally associated with slow physiological processes such as cell swelling, blood flow changes, or metabolic responses, happening on the scale of a few seconds to minutes. **Fast signals**, in contrast, correspond to rapid neuronal activity such as phototransduction in photoreceptors and the generation of action potentials, which occurs on time courses of hundreds of milliseconds [129].

IOS changes in ORG can be derived using either intensity-based or phase-based measurements:

2.7.1 Intensity-based ORG (iORG)

Intensity-based ORG (iORG) relies on morphological changes triggered by neuronal activation that affect optical properties of the tissue- refractive index, scattering, birefringence, or reflectivity [75, 89, 124, 125, 128]. The iORG signal can be detected by either analyzing the relative intensity variation in the local pixel values in response to a light stimulus or by examining the appearance of hyper- and hypo-reflective bands in the retina under different lighting conditions. Typically, the iORG is quantified by measuring the relative intensity variation as:

$$iORG = \frac{I_{abs} - I_{baseline}}{I_{baseline}} = \frac{\Delta I}{I} \tag{2.40}$$

where, I_{abs} refers to the average intensity value of a retinal layer ine one B-scan, $I_{baseline}$ denotes the mean intensity of the tissue layer before the onset of stimulus, and ΔI represents the difference in the two values in one B-scan.

2.7.2 Phase-based ORG (pORG)

Phase-based ORG (pORG) is the most prevalent method used to study retinal neuronal dynamics due to its higher sensitivity compared to intensity-based measurements. High-speed OCT systems, particularly those with adaptive optics, can capture fast intrinsic signals that happen in the scale of a few milliseconds. pORG evaluates phase changes to assess optical path length (OPL) variations in the retina [28,74–78,80,81,83–85,87,88,130]. For a typical photoreceptor pORG, the change in OPL (ΔOPL) is given by:

$$\Delta OPL = \frac{\lambda_0}{4\pi} \times (\phi_{COST} - \phi_{ISOS}) \tag{2.41}$$

where λ_0 is the central wavelength of the light source used in the imaging system, and $(\phi_{COST} - \phi_{ISOS})$ represents the phase difference between the Inner Segment-Outer Segment (ISOS) junction and the cone outer segment tip (COST) layer. Several studies have shown that the magnitude of these OPL changes is strongly correlated with the intensity of the light stimulus [76, 83, 84, 88]. This method can also capture responses from other retinal layers, provided there are distinguishable peaks with a high SNR value.

However, pORG is highly sensitive to motion artifacts and typically requires high-speed acquisition systems with high phase stability. Additionally, pORG signals often require extensive post-processing, including sub-pixel registration, to reduce noise and improve accuracy. The establishment of normative data for ORG responses in healthy human population is crucial to compare results from diseased subjects. Moreover, clinical application would require simplification of data acquisition and analysis. Although current studies capture responses across retinal layers, further research into the nature of signals and the origin is needed to deepen our understanding of the phenomenon of neurovascular coupling.

In this thesis, both intensity- and phase-based intrinsic optical signals are studied in response to a short-duration single flash ($< 10ms$). Responses are extracted from both inner retinal layers, such as the Nerve Fibre Layer and Inner Plexiform Layer, as well as the outer retinal layers, including the Photoreceptor layer, Outer Plexiform Layer, and Retinal Pigment Epithelium. This approach helps elucidate the distinct activation patterns of these structures in response to visual stimulation.

Chapter 3

Combined optical coherence tomography and electroretinography (OCT+ERG) system for imaging neurovascular coupling in the human retina

Notes and Acknowledgments

This chapter describes the optical design of a combined OCT+ERG system developed for simultaneous data acquisition of the OCT morphological images, Doppler OCT blood flow data, ORG responses from neuronal cells of the retinas well as the ERG recordings. The OCT+ERG system was used to image a healthy human retina in response to a single flash summarizes the results from a study that aimed to under the effect of stimulating different types of photoreceptors on retinal blood flow in healthy humans, measured with a combined OCT + ERG system. The content of this chapter is based on the following submitted manuscript:

Dhaliwal K, Wong A, Wright T, Bizheva K. "Combined optical coherence tomography and electroretinography (OCT+ERG) system for imaging neurovascular coupling in the human retina", submitted to *Neurophotonics, 2024.*

Author Contributions

Kostadinka Bizheva conceived the study and provided the study materials.

Khushmeet Dhaliwal acquired the OCT data, **Tom Wright** acquired the ERG data.

Khushmeet Dhaliwal wrote the algorithm for retinal segmentation, ORG signal extraction, and blood flow analysis. **Khushmeet Dhaliwal** and **Alexander Wong** wrote the algorithm for blood vessel segmentation.

Khushmeet Dhaliwal processed the experimental data.

Khushmeet Dhaliwal analyzed the experimental results.

Khushmeet Dhaliwal and **Kostadinka Bizheva** contributed to the interpretation of the results.

Khushmeet Dhaliwal wrote the first draft of the manuscript.

All authors contributed to the final version for publication.

3.1 Introduction

The retina, often called 'the window to the brain', is an extension of the central nervous system (CNS) designed for detection of visual information and its transmission to the visual cortex of the brain [131]. Retinal neurons of highly specialized function such as photoreceptors which detect light and filter it by spectral content, bipolar and horizontal cells which filter the photoreceptors responses spatially and temporally, and the ganglion cells which amplify the visual information and transmit it to the brain, are organized is well defined layers [1, 90–92]. Furthermore, the retina is highly vascularized with oxygen and nutrition delivered to the retinal neuron in the anterior retina by the inner retina vasculature, and to the photoreceptors by the choroidal vasculature [4, 94]. Neurovascular coupling in the retina is referred to as a temporary increase in the retinal blood flow and vasodilation of retinal blood vessels in response to the increased metabolic demand of retinal neurons. This phenomenon was first observed in the brain [9] and later, in the retina [11, 12] using non-invasive optical imaging methods.

Potentially blinding retinal diseases such Age-related Macular Degeneration (AMD) [23, 24], Diabetic Retinopathy [27,30,31], Retinitis Pigmetosa [25,26,28] and Glaucoma [20–22] affect a large portion of the world's aging population and amount to $> \$1.5B$ in direct costs to the Canadian Health Care system annually [132]. These diseases cause progressive loss of normal function and eventually irreversible cell death of retinal neurons that in the later stages of disease development are registered as morphological changes. As these diseases cause metabolic and physiological changes in the retinal neurons, studies have reported blood flow changes with the progression of these retinal diseases [7, 18]. However, the dynamic relationship between neuronal and blood flow changes (neurovascular coupling) is still not fully understood in the healthy and diseased human and animal retina partly due to the fact that functional and vascular studies have been conducted separately.

Optical Coherence Tomography (OCT) is an imaging modality that can generate non-invasively volumetric images of the retina with micrometer scale resolution, sufficient for visualization of the fine layered structure of the human retina [117, 120, 133–135]. When combined with Adaptive Optics, OCT is also able to visualize individual retinal neurons [76,77,136]. Doppler OCT can be used to measure retinal blood flow [57,60,61] while optical microangiography (OMAG) can used to map the retinal vasculature in 3D over a wide field-of view [69,137,138]. All of these OCT-based technologies have found valuable applications in ophthalmology for clinical research of various ophthalmic diseases [28, 63, 69, 139]. Both Doppler OCT [64–66] and OMAG [70,72] technologies have been used in the recent past to evaluate blood flow changes in the human retina evoked by visual stimulation. However, these studies utilized very long stimuli (> 5 seconds) and did not record the retinal blood

flow (RBF) changes continuously [64, 65, 71, 122]. Therefore, they were not able to provide information of the transient behaviour of the RBF with high temporal resolution.

Optoretinography (ORG) is the optical equivalent of electroretinography(ERG), which is a clinically established method for electrical recordings of the responses of retinal neurons to visual stimulation. The use of OCT for non-invasive, optical recording of visually evoked neuronal changes was first proposed by Bizheva and the proof-of-principle was demonstrated in in-vitro in animal tissue where OCT and ERG data were acquired synchronously [89]. With advances in camera and laser technologies, over the past 20 years different OCT system designs were developed for ORG recordings of visually evoked neuronal activity in the human and animal retina: point scanning Spectral Domain OCT [81], AO-OCT [76, 77], Full-Field SS-OCT [74, 83, 85, 88] and Line-Field -SD-OCT [78, 84]. While majority of the ORG data was acquired mostly from healthy retinas, most recent studies have explored changes in the ORG signal related to retinal diseases [28].

Here we present the design of a novel, combined OCT+ERG system, imaging protocols and image processing algorithms that were developed for simultaneous probing of visually evoked changes in the human retina neuronal function and RBF with high spatial and high temporal resolution. The OCT+ERG imaging modality can serve as a new research tool for exploring neurovascular coupling in the human retina.

3.2 Methods

The following paragraphs describe the optical design of the OCT system, the imaging protocols for the data collection and the image processing algorithms for analysis of the neuronal and vascular responses of the living retina to visual stimulation.

3.2.1 OCT+ERG system

A combined OCT+ERG system was developed for non-invasive probing of neurovascular coupling in the living human retina. The optical design of the compact, fiberoptic, spectral-domain OCT system is shown in Figure 3.1, while a photograph of the OCT imaging probe integrated with a custom visual stimulator is presented in Figure 3.1B. The output of a femtosecond laser (Femtolasers GmbH, Austria) was connected to a spool of a 100 m long fiber to stretch the femtosecond pulses and mimic CW emission over a broad spectral range ($\sim$ 670 nm to 920 nm). The output from the spool was interfaced with a fiberoptic

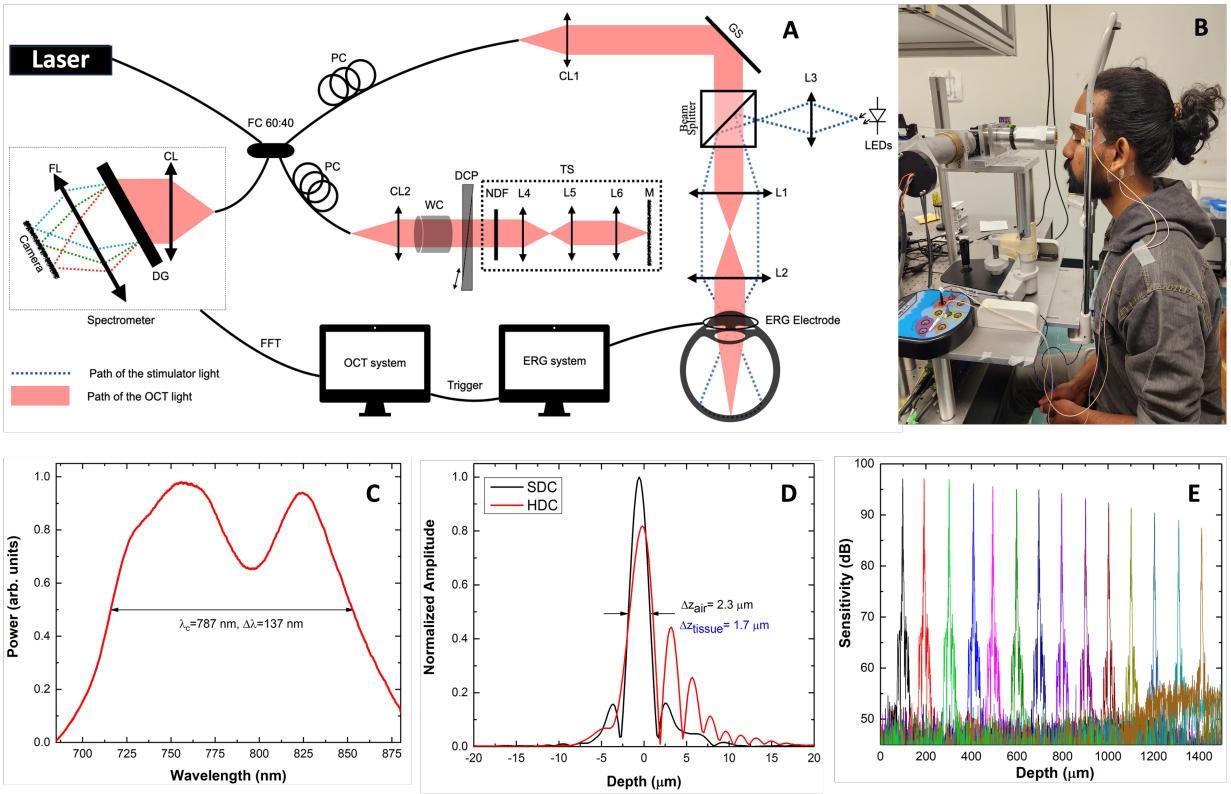


Figure 3.1: (A) Schematic of the combined OCT+ERG system. (B) Photograph of the OCT+ERG imaging probe. (C) Laser spectrum measured from the reference arm of the OCT system. (D) Axial OCT PSF after hardware (red color) and software (black color) dispersion compensation. (E) Sensitivity roll-off with imaging depth.

coupler (60/40 split ratio, Gould Fiberoptics, USA) that served as the core of the OCT interferometer.

In the imaging arm of the OCT system, a parallel optical beam of 2.8 mm diameter was generated with a fiber collimator (CL1 - achromat doublet, f = 10 mm, Thorlabs, USA). A pair of galvanometric scanners (Cambridge Technologies, USA) were used to scan the imaging beam over the retinal surface. A telescope comprised of 2 achromat doublet lenses (L1 (f = 75 mm) and L2 (f = 60 mm), Thorlabs, USA) was used to generate a parallel optical beam of 2.24 mm diameter and optical power $\sim$ 1.1 mW that was projected onto the human cornea. The mechanical design of the telescope allowed for easy adjustment of the distance between lenses L1 and L2 to compensate for myopia and hyperopia in the imaged subjects and fine-tune the focusing of the imaging beam within the retina. A custom visual stimulator comprised of a wheel with 4 LEDs (white, blue, green and red) was integrated with the OCT imaging probe through lens L3 (f = 50 mm, Thorlabs, USA) and a pellicle beam splitter (T/R ratio of 92/8, Thorlabs, USA). This design allows for the light from one of the LEDs to be focused at the pupil plane of the human eye in order to generate wide field of view illumination of the retina with almost uniform intensity (Maxwellian view). The custom visual stimulator was interfaced with a commercial electroretinography (ERG) system (Espion 2, Diagnosys LLC, USA), which served two purposes: a) precise control of the timing, duration, intensity and frequency of visual stimulus; and b) simultaneous collection of ERG and OCT recordings, so that the ERG recordings are used as a “gold standard" to validate the ORG traces extracted from the OCT images.

The reference arm of the OCT interferometer was comprised of a fiber collimator (achromat doublet, f = 10 mm, Thorlabs, USA), a custom-built 1 cm long water cell (WC) for crude compensation of water dispersion of the OCT imaging beam within the human eye, a custom dispersion compensation (DCP) unit comprised of BK7 prisms mounted on miniature translation stages (Edmund Optics, USA), a telescope (L4 and L5, achromat doublets (f4 = f5 = 60 mm), Thorlabs, USA), a focusing lens (L6, achromat doublet (f = 10 mm), Thorlabs, USA) and a mirror mounted on a miniature translation stage (Edmund Optics, USA). The telescope and the focusing mirror were mounted on a manual translation stage (Edmund Optics). Polarization controllers (PC) were used in both arms of the interferometer.

The detection end of the OCT system was comprised of a commercially available spectrometer (Cobra-S 800, Wasatch Photonics, Durham, USA), interfaced with a line-scan CMOS camera (OCTOPLUS, Teledyne, USA) with a readout rate of 250 kHz.

Figure 3.1C shows the spectrum of the optical beam measured at the detection end of the OCT system, which accounts spectral changes induced by the optical transmission

function of the OCT system. Figure 3.1D shows the axial PSF after hardware dispersion compensation only (red line) and after additional software dispersion compensation (black line), based on previous publications [52, 53]. The OCT system's maximum sensitivity measured for 1.1 mW imaging power which is well below the maximum permissible exposure (MPE) as specified by the ANSI standard [140] and camera speed of 250 kHz was 98 dB with a roll-off of $\sim$ 10 dB over a scanning range of 1.5 mm (Figure 3.1E).

3.2.2 In-vivo imaging of the human retina

A pilot study to test the clinical viability of the OCT+ERG system was conducted on 2 healthy subjects (2 males, age range 25 yo $\pm$ 5 years). The study received full ethics clearance from the University of Waterloo's Office of Research Ethics and a written consent was obtained from all participants. The study participants underwent standard clinical examination prior to the OCT imaging sessions and only subjects with no ocular diseases or a history of epilepsy and nearly perfect vision (minor correction up to -1 Diopters) were included in the study. A DTL type ERG electrode was inserted under the lower eyelid of the imaged eye, while reference and ground ERG electrodes are applied to the participant's temple and behind the ear respectively (Figure 3.1B). Both pupils were dilated by application of 1 drop of Tropicamide in each eye followed by $\sim$ 30 minutes dark adaptation. A faint red LED was used as fixation target for the contralateral eye.

3.2.3 Visual stimulation and image acquisition protocols

In this study, the retina was stimulated with white-light single flashes of 4 ms duration and different intensities ranging from $0 cd.s/m^2$ (dark recordings) to $43.4 cd.s/m^2$. OCT and ERG data were acquired over a period of $\sim$ 6 seconds (1 second pre-stimulus and 5 seconds post-stimulus), as shown in Figure 3.2A. Table 3.1 shows the percentage of photoreceptor bleaching for each stimulus intensity used in this study, calculated based on the method described by Rushton and Henry [86, 141].

Large field-of-view, volumetric morphological OCT images of the retina (1,000 A-scans $\times$ 1,000 B-scans, corresponding to $\sim$ 7 mm $\times$ 7 mm) were acquired prior to acquisition of the functional OCT recordings, to map the vasculature on the retinal surface. Next, a series of 1,200 OCT B-scans, each composed of 1,000 A-scans spanning over 1 mm (Figure 3.2B), were acquired from the same place in the retina located approximately midway between the fovea and the optic nerve head (red line in Figure 3.2C).

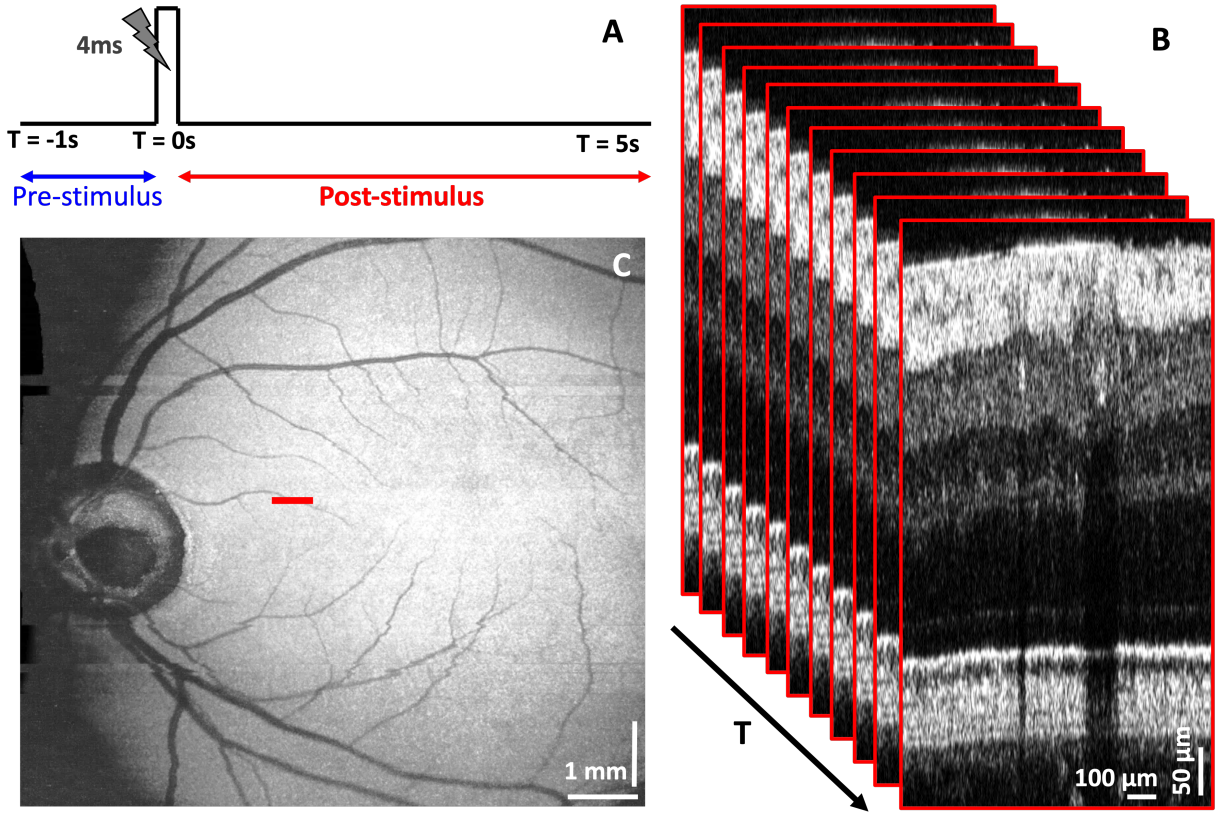


Figure 3.2: Image acquisition protocol for the optoretinography and functional blood flow recordings. (A) Timeline of the visual stimulus. (B) A sequence of 1,200 repeated B-scans acquired over duration of ~ 6 seconds from a location in the retina approximately midway between the fovea and optic nerve head (C, red line).

Stimulus Intensity ($cd.s/m^2$)	**Photoreceptors Bleaching** (%)
1.4	1.4
14.5	13.8
43.4	36

Table 3.1: Bleaching percentage for different stimulus intensities.

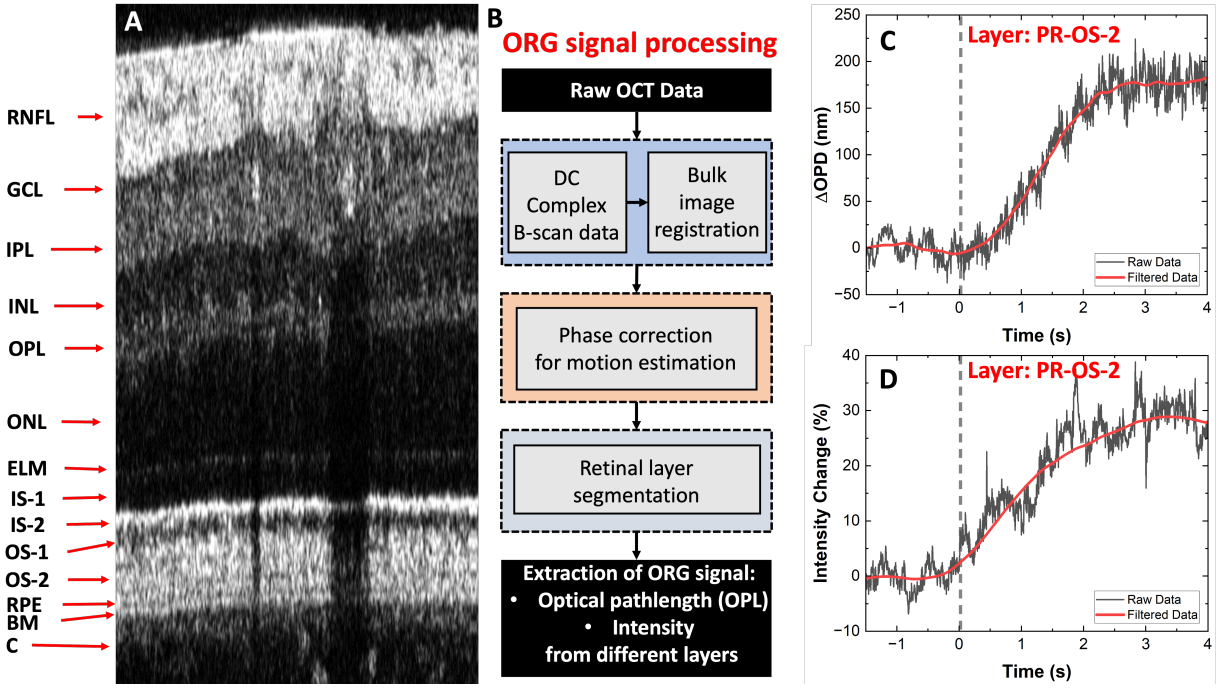


Figure 3.3: Protocol for extracting ORG traces from the repetitive B-scans. (A) A representative B-scan showing the layered structure of the human retina and cross-sections of large blood vessels in the RNFL. (B) Flow chart of the image processing steps to extract the optical path length difference (OPD) and intensity ORG traces from different retinal layers. Example ORG traces: OPD (C) and intensity (D) extracted from the OS-2 band of the photoreceptors layer.

3.2.4 Image processing and data analysis

Custom MATLAB-based algorithms were developed for processing and analysis of the OCT data. The raw OCT data was first processed to generate dispersion-compensated complex-valued B-scans (representative intensity image shown in Figure 3.3A). Figure 3.3B shows a flow chart for the image processing steps designed to measure ORG responses (optical path length and intensity changes) from different retinal layers. To account for involuntary eye motion caused by breathing, heartbeat and eye muscle twitching, a sub-pixel phase-restoring image registration method was utilized to correct for motion-related misalignment between consecutive B-scans [87, 142, 143]. Next, a region of interest (ROI) located outside the shadows of the retinal blood vessels was defined for each B-scan of the time series,

the retinal layers were segmented automatically based on their intensity profiles using boundary detection and textural changes [144], and the B-scans were flattened using the photoreceptors IS-2 layer as a guideline. The segmented data was used to extract optical path length and intensity changes for each retinal layer in response to visual stimulation. To generate the intensity traces, the values for all pixels within each segmented layer were averaged both axially and laterally to reduce speckle noise. Optical path length changes within the segmented layers were calculated based on the following equation:

$$\Delta OPD = \frac{\lambda_0}{4\pi} \times (\phi_{target} - \phi_{reference}) \tag{3.1}$$

where, ΔOPD represents the optical path length changes between the reference and the target layers, λ_0 is the central wavelength of the imaging light source, and $(\phi_{target} - \phi_{reference})$ represents the phase difference between the target retinal layer and the reference layer. IS-2 was used as the reference layer for OS-2, and Inner Plexiform Layer (IPL) was used as the reference layer for all the other target layers. Phase stability of the system was characterized by determining the inter-layer displacement sensitivity, measured by employing methods described by other groups [78, 133]. The calculated inter-layer displacement sensitivity with spatial averaging was found to be about 5 nm.

Representative OPD and intensity traces extracted from the photoreceptors OS-2 layer are shown in Figures 3.3C and 3.3D, respectively. The high frequency data (black line) resulting from the OCT speckle pattern and periodic modulations related to breathing and heart rate were filtered out using a combination of filtering functions, in order to generate the smooth time traces (red curves) in Figures 3.3C and 3.3D.

A custom algorithm was also developed for quantifying vascular changes (retinal blood flow and blood vessel diameter) caused by visual stimulation. Figure 3.4A shows a representative B-scan, where an ROI including the cross-section of a retinal blood vessel is marked with the red dashed line. Figure 3.4B shows a flow chart of the algorithm developed for analysis of the vascular changes.

Bulk registration was used to align all B-scans for eye motion [142]. Next, a blood vessel was manually selected from the first B-scan in the time series by looking at the shadow cast by the vessel in the deeper layers of retina as blood cells are highly reflective. The width of the shadow was correlated to the diameter of the blood vessel as the lumen of retinal blood vessels has much lower reflectivity. The blood vessel was cropped from all B-scans in the time series using a semi-automated algorithm. This data was used to extract the blood velocity information based on the phase shift between the adjacent A-scans [60, 121]. The retinal blood flow (RBF) was obtained from each B-scan using:

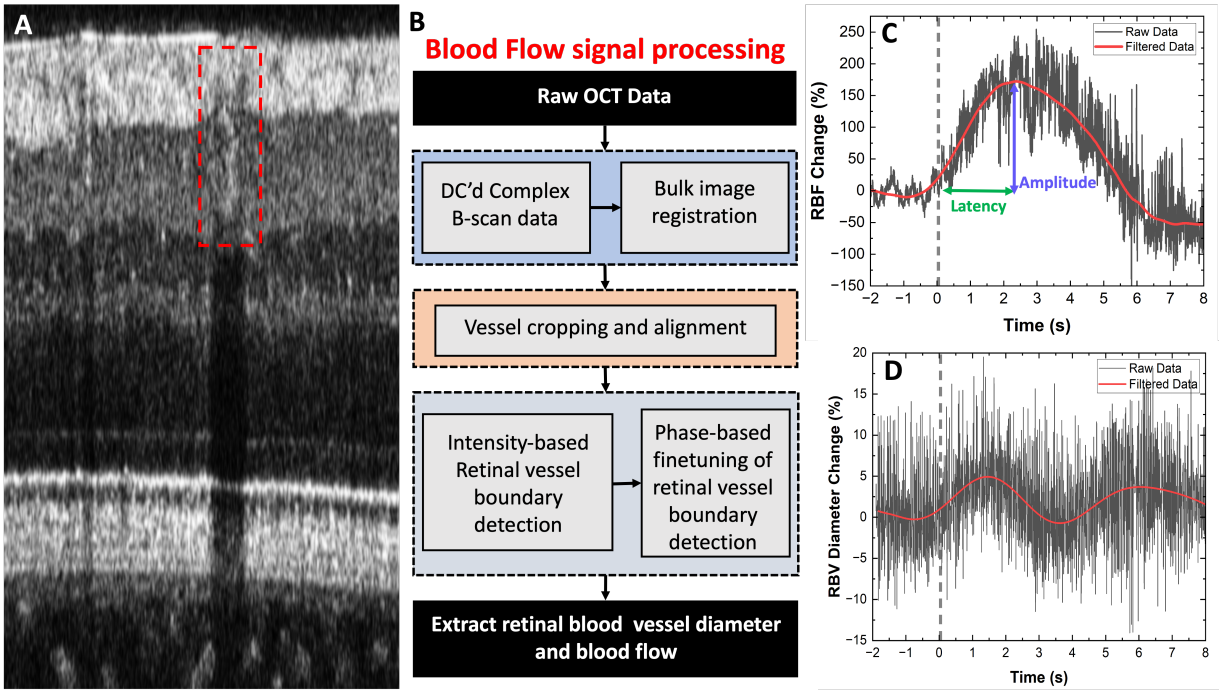


Figure 3.4: Protocol for measuring transient changes in the retinal blood vessels. (A) A representative retinal B-scan with the cross-section of a retinal blood vessel marked with the red dashed line. (B) Flow chart of the image processing steps to quantify dynamic vascular responses (blood flow change and dilation / constriction of retinal blood vessels) to visual stimulation. (C) Retinal blood flow change in response to 4 ms single flash white-light stimulus. (D) Corresponding blood vessel diameter change.

$$F = V \times \frac{\pi D^2}{4} \tag{3.2}$$

where, F is the retinal blood flow, V is the retinal blood velocity, and D is the diameter of the blood-vessel cross-section. Therefore, the blood velocity and vessel area information (in appropriate units) was used to evaluate visually evoked RBF changes over the time series of B-scans.

Representative RBF and blood vessel diameter (BVD) time traces are shown in Figures 3.4C and 3.4D. The raw data exhibited high fluctuations (black lines) because of the speckle present in the OCT images. A smoothing filter with a moving window (Savitzky-Golay) was used to filter out the high frequency component of the data. Next, the filtered data was zero-padded ($\sim 3\times$) to enable band-block filtering of the pulsatile fluctuations caused by the participant's heart rate and to generate smooth traces (red lines) of the time-dependent changes of the RBF and BVD caused by the visual stimulation of the retina. Fractional changes in the RBF was computed based on the following relation:

$$RBFChange\,(\%) = \frac{SignalRBFvalue\,(A) - BaselineRBFvalue\,(B)}{BaselineRBFvalue\,(B)} \times 100 \tag{3.3}$$

where, the signal RBF value corresponds to the RBF value obtained for a vessel in each B-scan and the baseline RBF value corresponds to the mean RBF value during the pre-stimulus period. A similar analysis was conducted to compute fractional changes for BVD response in the axial and lateral directions:

$$BVDChange\,(\%) = \frac{SignalBVDvalue\,(A) - BaselineBVDvalue\,(B)}{BaselineBVDvalue\,(B)} \times 100 \tag{3.4}$$

Here, the signal BVD value represents to the value of cross-sectional diameter of a blood vessel in a B-scan and the baseline BVD value is determined by taking average of the vessel diameter fluctuations over pre-stimulus recording.

To quantity the RBF and BVD response to visual stimulation, we employed 2 metrics: 'amplitude', measured relative to the baseline (pre-stimulus data) and 'latency' measured from the onset of the visual stimulus to the time of the peak response (Figure 3.4C).

3.3 Results

3.3.1 Morphological human retinal images

Figure 3.5 shows representative cross-sections and *en face* morphological images of the healthy human retina. The high axial OCT resolution allowed for clear visualization of the Bruch's membrane (Figure 3.5A, green arrow), the retinal pigmented epithelium (RPE, Figure 3.5A, orange arrow), the posterior end of the photoreceptors outer segment (OS-2, Figure 3.5A, blue arrow), that contains RPE micro-villi rich in melanin granules, responsible for the high reflectivity of this sub-layer, reflections from cone tips in the anterior part of the photoreceptor's outer segment (Figure 3.5A, red arrows) and the highly reflective posterior end of the photoreceptors inner segment (IS-2, Figure 3.5A, white arrow), that contains densely packed mitochondria. The high axial resolution also allows for visualization of three distinct sub-bands in the retinal inner plexiform layer (IPL, Figure 3.5B, yellow arrow) that were previously observed with research-grade visible light OCT technology with comparable axial resolution [134].

Figure 3.5C shows an *en face* view of the microvasculature at the inner plexiform layer (IPL) of the retina. Figure 3.5D shows an *en face*, maximum intensity projection image of the photoreceptors IS/OS junction. Figures 3.5E and 3.5F show magnified views of a ROI located a few degrees away from the center of the fovea, where reflections from cones can be observed (highly reflective white dots).

3.3.2 Retinal response to a flash with one intensity

Figure 3.6B shows intensity profiles of the human retina generated from a time series of B-scans (single representative B-scan from the series is shown in Figure 3.6A) for selected time points before, during and after the single flash stimulus. The intensity profiles were aligned with respect to each other, using the peak corresponding to the photoreceptors IS-2 layer as a reference point. A simplified pictorial representation of the retina's cellular pathway for generation and transmission of visional information is also shown in Figure 3.6A. The figure shows clearly that visual stimulation causes time dependent increase and decrease in the intensity of different retinal layers, as well as temporary swelling in some of the retinal layers, that results is spatial shifts of the intensity peaks corresponding to those retinal layers (optical pathlength changes).

Figure 3.7 shows a summary of the retinal response to visual stimulation (4 ms duration and $43.4 cd.s/m^2$ intensity) in terms of physiological changes in the retinal neurons

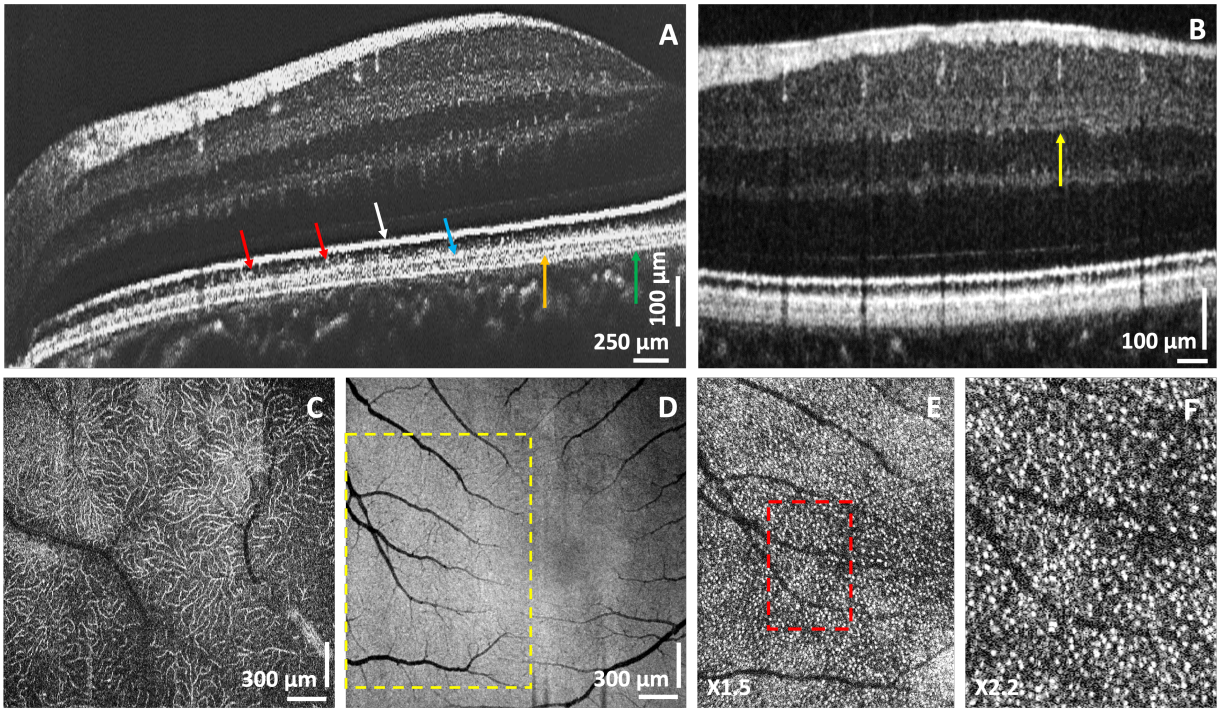


Figure 3.5: OCT images of the healthy human retina. The high spatial resolution is sufficient to resolve the Bruch's membrane (green arrow), the RPE (orange arrow), the photoreceptors OS-2 layer (blue arrow) and reflections from individual cone OS tips (red arrow) (A), the 3 sub-layers in the retinal IPL (B) and the intricate capillary network in the retinal OPL (C). *En face* view of the photoreceptors IS/OS junction (D). Magnified views of the photoreceptors mosaic, where tips of individual cones are resolved (white dots in E and F).

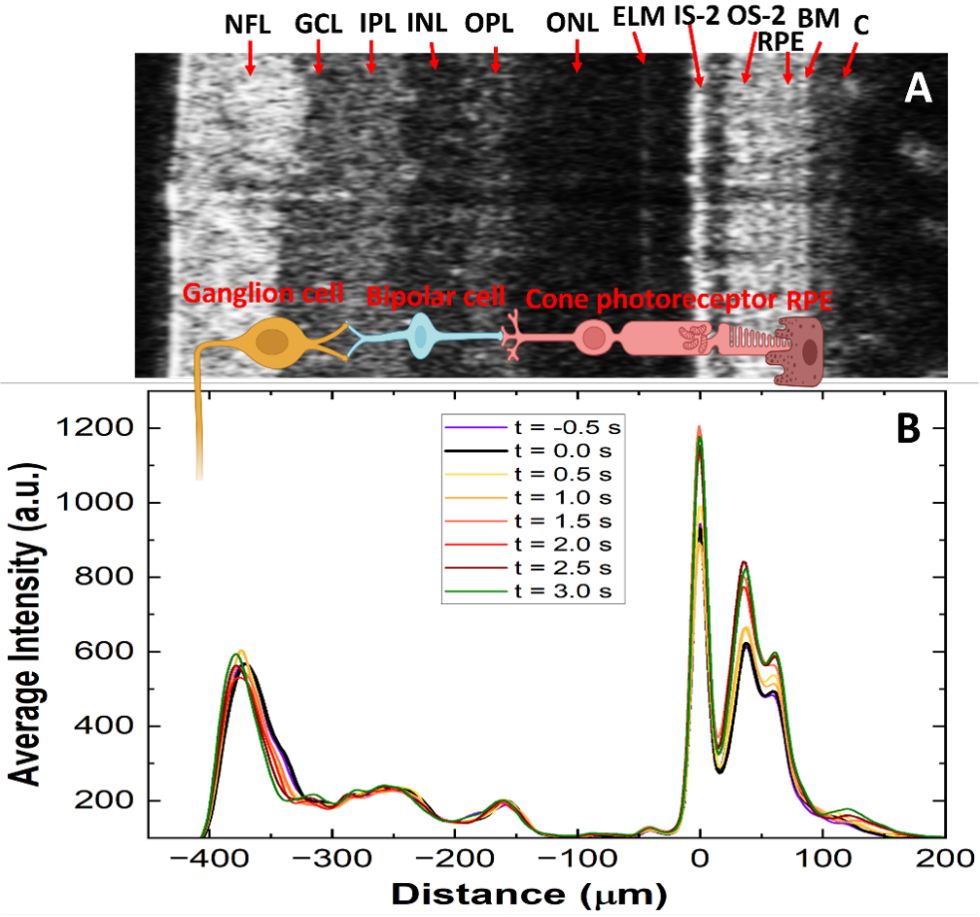


Figure 3.6: (A) Representative B-scan of the healthy human retina from a functional OCT time series with layers labeled. (B) Retina intensity profiles extracted from the series of B-scans for selected time points before, during and after application of the visual stimulus. Pictorial representation of the cellular pathway for generation of visual information.

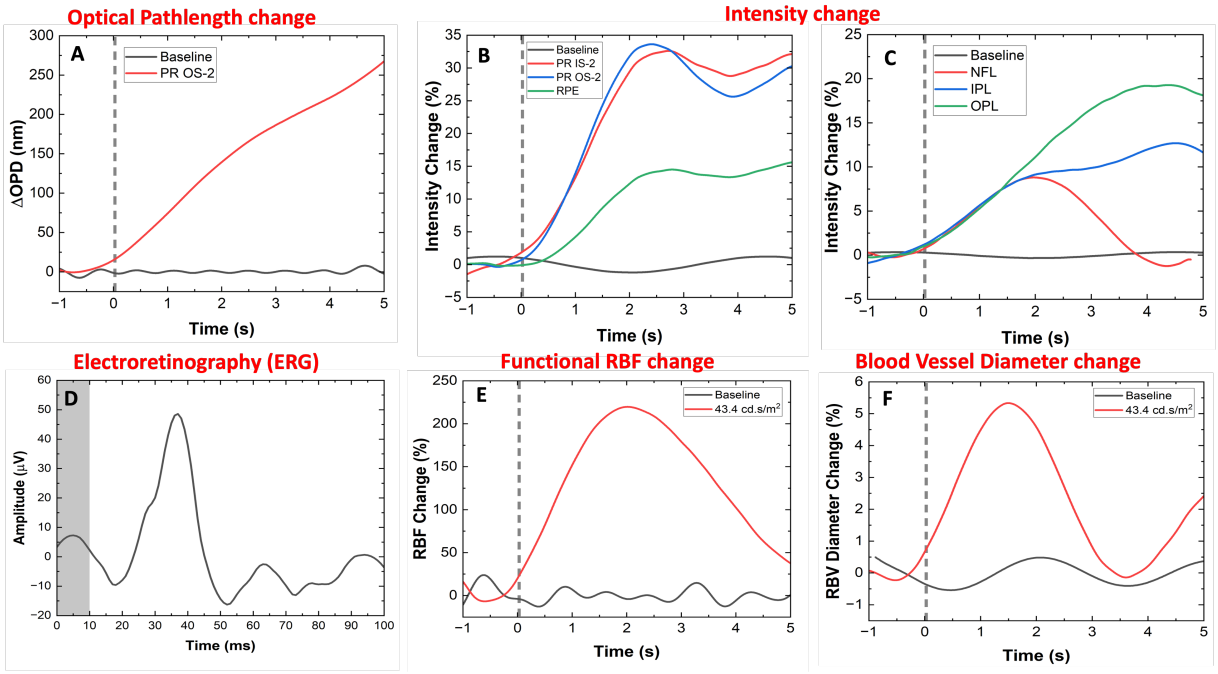


Figure 3.7: Summary of the healthy human retina response to visual stimulation (white light, single flash, 4 ms duration and $43.4 cd.s/m^2$ intensity) in terms of physiological changes in the retinal neurons measured with OCT (intensity and OPD changes) and ERG, and vascular changes (transient changes in the RBF and BVD). (A) Optical path-length changes from PR OS-2 layer. Intensity changes measured from retinal layers located in the posterior (B) and anterior (C) retina. (D) Representative ERG recording. Visually evoked changes in the retinal blood flow (E) and blood vessel diameter (F).

measured with OCT (intensity and OPD changes) and ERG, and vascular changes (transient changes in the RBF and BVD). Figure 3.7A shows phase-based optical path length changes in the photoreceptors OS-2 band (red line). The photoreceptors show a consistent expansion, reaching a value of $\sim$ 250 nm at $\sim$ 5 seconds after the stimulus onset. The black line shows the OPD changes during baseline (dark recording).

Figure 3.7B and 3.7C show intensity-based changes in the retinal layers. Figure 3.7B shows the intensity changes in the outer retina, specifically the IS-2 (red curve), the OS-2 (blue curve), and the RPE (green curve). The intensity changes observed in the IS-2 and the OS-2 layers are similar in magnitude ($\sim$ 30%), however the peak intensity change for the OS-2 layer occurs a few milliseconds earlier than the change in the IS-2 layer. The intensity change in the RPE layer is of significantly lower magnitude and reaches a plateau almost simultaneously with the change observed in the OS-2 layer. The black curve shows the baseline (dark recording) response of the PR OS-2 layer.

Figure 3.7C shows intensity changes in the NFL (red curve), the IPL (blue curve) and the OPL (green curve). The OPL shows the highest change in intensity amongst these retinal layers, with a maximum change of sim20% plateauing at $\sim$ 3.5 seconds after the stimulus onset. The NFL and the IPL both show a similar intensity change of $\sim$ 10% at $\sim$ 2 seconds after the stimulus onset with the IPL intensity returning to baseline within $\sim$ 4 seconds of the stimulus onset. The black curve shows the baseline (dark recording) response of the IPL layer.

Figure 3.7D shows a representative single flash ERG trace acquired for a stimulus intensity of $3.44 cd.s/m^2$. The negative a-wave peaks at $\sim$ 18 ms after the flash onset, while the positive b-wave peaks at $\sim$ 35 ms after the flash onset. The gray rectangle in the plot shows the timing and the duration of the white light, single flash stimulus.

Figure 3.7E shows representative RBF traces from dark recordings (no flash, black curve) and a single flash recording with intensity of $43.4 cd.s/m^2$ (red curve). The black curve in the figure shows the blood flow response in the absence of visual stimulation. On an average an RBF change of $< 20\%$ is present in the absence of visual stimulation. However, a change of as high as 200% is observed with a single flash of $43.4 cd.s/m^2$ intensity (red curve), which peaked at $\sim$ 2 seconds after the flash onset. The RBF changes are transient and the flow returns to baseline within $\sim$ 5 seconds from the stimulus onset.

Figure 3.7F shows representative changes in retinal blood vessel diameter in response to a single-flash stimulus of $43.4 cd.s/m^2$ intensity. The black curve shows the response in the absence of stimulation, where a slight pulsatile behavior is be observed. However, with the onset of stimulation, the vessel dilates to $\sim$ 5% reaching a maximum value at $\sim$ 1.5 seconds after the onset of the flash (red curve).

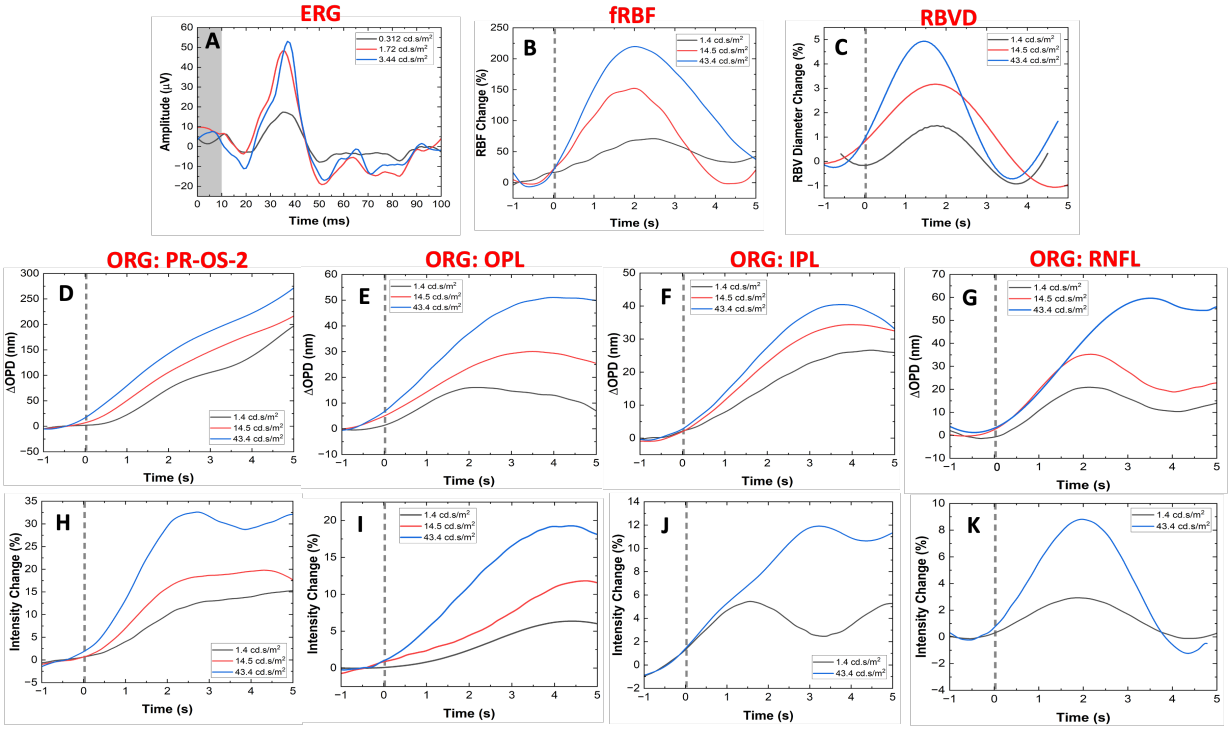


Figure 3.8: Different responses at different intensities of single-flash stimuli. (A) ERG traces; (B) RBF changes; (C) BVD changes; (D) and (H) Optical path length and intensity changes in the photoreceptor OS-2 layer; (E) and (I) Optical path length and intensity changes in the outer plexiform layer; (F) and (J) Optical path length and intensity changes in the inner plexiform layer; and (G) and (K) Optical path length and intensity changes in the retinal nerve fiber layer.

3.3.3 Retinal response to different intensities

Next, we explored the dependence of the retinal response to visual stimulation of different intensity by varying the intensity of the 4 ms single white-light flash stepwise in the range $0 - 43.4 cd.s/m^2$. Figure 3.8 shows representative results for 3 stimulus intensity values: $1.4 cd.s/m^2$, $14.5 cd.s/m^2$ and $43.4 cd.s/m^2$. The ERG recordings (Figure 3.8A) showed progressive increase of the amplitude of the a-wave and b-wave, as well as small changes in the peak latency of the b-wave.

The retinal blood flow (Figure 3.8B) showed significant increase in the peak magnitude of the transient blood flow changes with progressive increase of the stimulus intensity.

The peak latency decreased initially between recordings with $1.4cd.s/m^2$ and $14.5cd.s/m^2$ stimulus intensities, and plateaued for flash intensity of $43.4cd.s/m^2$. Similar non-linear behavior of the RBF latency was observed by our research group in retinal veins for measurements conducted at the periphery of the optic nerve head in a different study [145]. The recovery time of the RBF baseline is also affected by the intensity of the visual stimulus and is longer for the highest intensity of the flash. The retinal blood vessel diameter (RBVD) (Figure 3.8C) showed similar behavior to the RBF. The peak magnitude of the vasodilation increased progressively while the peak latency decreased with the increase of the stimulus intensity.

Figures 3.8D and 3.8H show the phase-based (optical pathlength difference – OPD) and the intensity-based ORG responses for the photoreceptors OS-2 layer respectively. The OPD traces showed almost linear increase over the 5 seconds time with the onset of the flash, and the response was proportional with the increase of the flash intensity, reaching a peak magnitude of $\sim$ 300 nm for the strongest flash. While the magnitude of the intensity-based ORG responses also scaled with the increase of the flash intensity, it plateaued at $\sim$ 2.5 seconds relative to the flash onset, reaching a peak magnitude of $\sim$ 30% relative to the baseline (dark recording).

Figures 3.8E and 3.8I show the phase-based (OPD) responses and intensity-based ORG responses measured from the retinal outer plexiform layer (OPL) respectively. The optical path-length increase in this layer is almost 10 times smaller in magnitude compared to the response measured from the photoreceptors OS-2 layer, reaching peak magnitudes of $\sim$ 20 nm, 30 nm and 50 nm for the 3 flash intensity values respectively. The peak latency relative to the onset of the flash also increased with the intensity of the flash in the range of 2s – 4s. For the lower intensity flashes, the response showed tendency for return to baseline, while the response to the strongest flash ($43.4cd.s/m^2$) plateaued after 4 seconds relative to the flash onset. The intensity-based responses measured for the lower intensity flashes showed transient responses of peak magnitudes of $\sim$ 5% and $\sim$ 12% and peak latencies of $\sim$ 1 second and $\sim$ 2 seconds respectively. The response to the strongest flash plateaued at $\sim$ 20% and $\sim$ 3.5 seconds latency relative to the flash onset.

Figures 3.8F and 3.8J show the phase-based (OPD) responses and intensity-based ORG responses measured from the retinal inner plexiform layer (IPL) respectively. The OPD traces showed progressive increase of the peak magnitude from $\sim$ 20 nm to $\sim$ 40 nm with increase of the flash intensity, while the peak latency decreased from $\sim$ 4.3 seconds to $\sim$ 3.5 seconds respectively. All of the traces showed tendency to return to baseline. The intensity-based responses showed progressive increase in the peak magnitude from $\sim$ 5% to $\sim$ 13% with increase of the flash intensity, while the peak latency increased from $\sim$ 1.5 seconds to $\sim$ 3 seconds respectively.

Figures 3.8G and 3.8K show the phase-based (OPD) responses and intensity-based ORG responses measured from the retinal nerve fiber layer (NFL) respectively. For the lowest stimulus intensity of $1.4cd.s/m^2$, the phase-based ORG response plateaued at $\sim$ 20 nm, with $\sim$ 2 second peak latency. The OPD response to the stimulus intensity of $14.5cd.s/m^2$, peaked at $\sim$ 30 nm with $\sim$ 2 second peak latency. The strongest flash resulted in almost linear OPD change that peaked at $\sim$ 60 nm with $\sim$ 3.5 second peak latency. The intensity-based changes measured from the NFL were of generally smaller magnitude peaking in the range of $3\% - 9\%$ with progressive increase of the peak latency with the stimulus intensity increase.

3.4 Discussion

The novel OCT+ERG modality (imaging technology and image processing algorithms) presented here allows for simultaneous high-resolution imaging of the human retina morphology and probing of the retinal neuronal and blood flow responses to visual stimulation. The OCT system is designed to operate in the same wavelength region ($\sim$ 800 nm) as commercial OCT systems and has a compact fiberopic design. The high axial resolution ($1.7\mu m$) is sufficient to resolve the multi-layered structure of the posterior human retina (Figure 3.3A), including the RPE and the Bruch's membrane, as well as the triple sub-bands of the inner plexiform layer (Figure 3.5B, yellow arrow) that have been observed in the past with research-grade, visible light (VIS-OCT) technology of similar axial resolution [134]. The system's lateral resolution is sufficient to resolve reflections from the tips of individual cone photoreceptors in the healthy human retina located a few degrees away from the fovea (white dots in Figures 3.5E and 3.5F), as well as the fine capillary network of the outer plexiform layer (Figure 3.5C).

Integration of the OCT system with a commercial ERG technology serves several purposes:

a) Synchronous ORG and ERG recording that allow clinicians access to retinal morphological, functional and vascular data that is acquired simultaneously;

b) Easy, flexible control of the visual stimulus and utilization of clinically approved ERG protocols for retinal stimulation

As the ORG research field is still relatively new, simultaneously recorded ERG traces can serve as a "gold standard" to validate the ORG recordings. Note that while the current

design of the visual stimulator allows for flexibility of choice in terms of timing, duration, intensity, frequency pattern and color of the visual stimulus, it can only generate a wide-field, Maxwellian view illumination of the retina. It also does not provide a fixation pattern for the imaged eye. Future designs of the visual stimulator will include fixation targets for the imaged eye, as well as ability to project spatial patterns of different sizes on the surface of the retina.

Results from this pilot study demonstrate that the OCT technology and image processing algorithms allow for measurement of both phase-based OPD changes and intensity-based changes from all major retinal layers, as well as transient changes in the retinal blood flow caused by visual stimulation of the retina. The simultaneous measurement of both neuronal responses and transient changes in the blood flow and vasodilation of local blood vessels allows for conducing of non-invasive studies of neurovascular coupling in the human retina. Data from this pilot study shows that in general both the phase-based OPD and intensity-based responses from retinal layers populated by different types of retinal neurons, to visual stimulation increase in magnitude relative to the baseline (dark recordings) with increase of the stimulus intensity, while the latency of the peak responses decreases or increases with increase of the stimulus intensity depending on the retinal layer type. The largest phase-based OPD changes were observed from the photoreceptors OS-2 sub-layer, which is consistent with results from animal studies and can be explained with transient water influx following the phototransduction process of rhodopsin located in the photoreceptors outer segments [127, 128]. The OS-2 layer also shows the largest intensity change ($\sim 30\%$) which can be associated with different factors:

a) temporary realignment of electrical dipoles within the double lipid membranes that form the OS layer, during the phototransduction process, which results in transient changes of the local refractive index;

b) conformational changes in the opsin protein can alter the scattering profile of the rhodopsin molecules in the OS layer;

c) water influx can cause transient changes in the reflectivity profile of the OS layer.

Phase-based OPD and intensity-based changes of almost $10\times$ smaller magnitude were observed from the outer and inner plexiform layers of the human retina in response to the visual stimulation (Figures 3.7 and 3.8). Since these retinal layers contain dense capillary networks, these changes are most likely related to transient increase in the retinal blood flow (retinal blood cells scatter light strongly) and vasodilation of the retinal capillaries.

The retinal NFL is composed of unmyelinated axons of the ganglion cells that conduct action potentials in order to transmit information from the retina to the brain. The transient increase in the NFL reflectivity measured with OCT during and immediately following the visual stimulation (Figure 3.8K) can most likely be explained by transient increase in the magnitude and frequency of the action potentials, which will alter the local electrical field and therefore the local refractive index of the ganglion cell axons. These changes will result in measurable changes of light reflected and scattered by the NFL [124]. The phase-based OPD changes measured from the NFL (Figure 3.8G) in response to the visual stimulation are most likely due to transient swelling of Müller glial cells, which are located in-between NFL fibers.

The visual stimulation of the human retina caused transient changes both in the local blood flow but also the vasodilation of the retinal blood vessels (Figures 3.8B and 3.8C respectively). These changes can be explained with the increased metabolic activity of retinal neurons during and immediately after visual stimulation which increases the demand for oxygen and nutrition delivered by the retinal blood network.

While we demonstrated that the temporal resolution of the OCT system is sufficient to measure transient changes in the neuronal activity (ORG recordings) and blood vasculature (RBF and RBVD) caused by visual stimulation, 10 second long recordings pose difficulties for both the imaged subjects (keeping the eye fixated and open) and the image processing algorithms (correction of eye motion artifacts). In this study, subjects tended to blink and lose fixation after $\sim$ 7 seconds, which limited the post-stimulus period to only 5 seconds and prevented exploration of the recovery process of the ORG and RBF traces back to baseline. Eye motion artifacts arising from involuntary eye motion (heart rate, breathing rate, ocular muscles twitching) also posed challenges to the filtering process of the ORG and RBF traces and caused the initial increase of the ORG and RBF changes to appear occurring slightly earlier than the stimulus onset. The limited speed of the camera in the current design of the OCT system also prevented measurement of initial fast negative OPD response from the OS-2 layer, corresponding to the ERG a-wave, that was observed by other research groups that used OCT technology with parallel detection such as Swept-Source OCT [77,83,88], Full-Field OCT [74], multiple detection channels [76] and Line-Field OCT [78,84].

3.5 Conclusions

In summary, we have developed a combined OCT+ERG system for in-vivo, simultaneous high -resolution imaging of the human retina structure and measurement of fast, transient

changes in the retinal neuronal function (ORG and ERG) and the local retinal blood flow (Doppler OCT) induced by visual stimulation. Both optical pathlength- and intensity-based ORG signals were acquired from the major retinal layers (nerve fiber layer, plexiform layers, photoreceptor inner and outer segments and the retinal pigmented epithelium). Data acquired in this study provides insight to the neurovascular coupling in the human retina. The novel OCT+ERG technology and OCT image processing algorithms presented here can serve as valuable research tools in future biomedical and clinical studies of potentially blinding neurodegenerative retinal diseases and brain neurodegenerative conditions that are expressed in the retina.

Chapter 4

Visual stimulus-evoked transient blood flow and blood vessel diameter changes in human retina measured with a combined OCT+ERG system

Notes and Acknowledgments

This chapter summarizes the results from a study that aimed to investigate the retinal blood flow in the larger blood vessels around the optic nerve head in healthy humans in response to $10Hz$ of white-light flicker stimulation, measured with a combined OCT + ERG system. The content of this chapter is based on the following submitted manuscript in preparation:

Dhaliwal K, Simmons J, Wong A, Hudson C, Wright T, Ballios B, Bizheva K. "Visual stimulus-evoked transient blood flow and blood vessel diameter changes in human retina measured with a combined OCT+ERG system", to be submitted to *IOVS*, 2024.

Kostadinka Bizheva conceived the study and provided the study materials. **Brian Ballios**, **Chris Hudson** and **Tom Wright** contributed to planning of the study.

Khushmeet Dhaliwal acquired the OCT data; **Tom Wright** acquired the ERG data.

Khushmeet Dhaliwal wrote the algorithm for retinal blood flow detection and **James Simmons** and **Khushmeet Dhaliwal** wrote the algorithm for blood vessel segmentation, with the help of **Alex Wong**.

Khushmeet Dhaliwal and **James Simmons** processed the experimental data.

Khushmeet Dhaliwal analyzed the experimental results.

Khushmeet Dhaliwal, **Kostadinka Bizheva**, **Chris Hudson**, **Brian Ballios**, and **Tom Wright** all contributed to the interpretation of the results.

Khushmeet Dhaliwal wrote the first draft of the manuscript.

All authors contributed to the final version in preparation for publication.

4.1 Introduction

Functional Hyperemia refers to the phenomenon of increased cellular metabolic demand leading to temporary vessel dilation in response to external stimuli [9]. First described by Roy and Sherrington in the brain over a century ago, this mechanism, also referred to as 'Neurovascular Coupling (NVC)', has also been identified in the retina. In this context, neurovascular coupling refers to the transient vasodilation and elevated blood supply to the retina triggered by the increased metabolic demands of retinal neurons responding to visual stimulation [11, 12].

Potentially blinding retinal neurodegenerative diseases- including age-related macular degeneration (AMD) [23, 24], glaucoma [20, 21], diabetic retinopathy [30, 31], and retinitis pigmentosa [25, 26]- are associated with significant changes in the ocular tissue that disrupt neurovascular coupling. These diseases alter the ocular tissue morphology and cellular structure, affecting cell shape and size, which subsequently impacts the optical scattering profile of the tissue. Additionally, they impair ocular blood flow and perfusion, impacting oxygen and nutrient delivery to the retinal tissues. Lastly, these diseases also induce changes in the metabolic and physiological responses of the tissue to external stimuli, further disrupting neurovascular coupling by affecting its constituent mechanisms [7, 18].

Several imaging modalities have been employed to image and detect retinal diseases in human and animal subjects, including fundus photography [33, 34], fluorescein angiography [42–44], laser Doppler velocimetry [37–39], retinal vessel analyzer [15, 47], laser Doppler flowmetry [35, 36], scanning laser ophthalmoscopy [40, 41], and optical coherence tomography (OCT) [54, 78, 102, 134, 146]. However, most of these techniques pre-dominantly detect morphological and vascular changes in the retina that typically emerge during the advanced stages of the disease after irreversible damage to the retina has occurred. Therefore, measurement of morphological, physiological, or metabolic changes in the retina at cellular level requires an imaging modality capable of detecting early-stage retinal changes and transient retinal responses to stimuli.

Doppler Optical Coherence Tomography (D-OCT), a functional extension of OCT, allows for the visualization of blood vessels and quantification of blood velocity via the principle of Doppler Shift as described in section 2.5 [56, 61, 66]. Wang *et. al.* introduced a double-circular scanning protocol around the Optic Nerve Head (ONH) to obtain absolute retinal blood flow values in the retina [62]. In this method, OCT data is acquired from two concentric circles centered at the ONH, enabling the Doppler angle determination using the geometric location of the vessel cross-section in the two B-scans. Since blood flow is the product of blood velocity and vessel cross-sectional area, morphological OCT

B-scans can be used to determine the area of the blood vessels, allowing for the calculation of total retinal blood flow (TRBF) around the ONH by summing individual vessel flow values. Therefore, D-OCT enables dynamic, real-time measurement of retinal blood flow. This capability allows researchers to capture retinal blood flow responses to visual stimuli, facilitating a deeper understanding of neurovascular coupling and its role in health and in disease.

Prior studies have investigated the response of retinal blood flow (RBF) to visual stimulation in both humans and animals. For instance, Wang *et. al.* observed an increase in RBF in healthy humans 10 to 15 seconds after a 30-second patterned white-light stimulus [65]; however, the time delay between the stimulation and the measurement likely obscured the transient peak in the visually-evoked RBF change. Other studies, such as that by Aschinger *et. al.*, used a prolonged 2-minute stimulation period, which may be less feasible in clinical settings, particularly for patients who may be sensitive to prolonged stimulation [122]. Similarly, Warner *et. al.* reported an increase of up to 22% in RBF in smaller vessels in response to 2 minutes of full-field flicker stimulation [96]. Kallab *et. al.* reported an increase in RBF and retinal blood vessel diameter in arteriovenal pairs in healthy human subjects in response to 7 Hz of flicker stimulation [71]. However, these protocols typically involved delayed measurements of RBF relative to the onset of the stimulus, potentially overlooking the rapid, dynamic blood flow changes crucial for understanding neurovascular coupling, as neuronal activity leads to increased metabolic demand that requires immediate vascular response.

To the best of our knowledge, no studies have been conducted in the past to record RBF responses before, during, and immediately after flicker stimulation in human subjects with sufficiently high temporal resolution to map the transient changes in the RBF. Tan *et. al.* conducted similar experiments in rats and observed a transient increase in RBF in response to visual stimulation and the RBF change peaked close to the off-set of the flicker stimulus [67]. Also, in a rat model of glaucoma, Tan *et. al.* observed that the transient RBF changes were suppressed during intraocular pressure (IOP) elevation, though the response normalized once IOP returned to baseline [147], highlighting the importance of monitoring dynamic RBF responses in diseased subjects.

In this study, a combined OCT+ERG system was used to simultaneously capture the transient RBF changes in retinal vessels in the immediate vicinity of the ONH, as well as electrophysiological responses to 10 Hz white-light flicker stimulation of various intensities in healthy human subjects.

4.2 Methods

4.2.1 OCT+ERG system

A custom-built optical coherence tomography (OCT) system, operating at 250 kHz acquisition rate was developed for this study. Briefly, the OCT system, operating in the 800 nm spectral region, was paired with a commercial electroretinography (ERG) system by Diagnosys LLC (Lowell, MA, USA). Both systems were combined by developing a custom imaging probe integrated with a custom visual stimulator and synchronizing the OCT and ERG data acquisition to allow for synchronous recordings of visually evoked changes in the retinal RBF responses with the OCT and electrical recordings with the ERG.

The fiber-based point-scanning, Spectral-Domain OCT system was powered by a broad bandwidth superluminescent diode-based light source with $\lambda_C = 810$ nm and $\Delta\lambda = 100$ nm (Superlum, Carrigtohill, Co. Cork, Ireland, M-D-810-HP) to ensure no prestimulation of the retina due to the imaging beam. The output of the light source was connected to a 60/40 fiber coupler (Gould Fiberoptics, USA), which served as the core of a fiberoptic Michelson interferometer, splitting the light into reference and sample arms. In the imaging arm of the OCT system, a parallel optical beam of 2.8 mm diameter was generated with a fiber collimator (CL1 - achromat doublet, f = 10 mm, Thorlabs, USA). A pair of galvanometric scanners (Cambridge Technologies, USA) were used to scan the imaging beam over the retinal surface. A telescope comprised of 2 achromat doublet lenses (L1 (f = 75 mm) and L2 (f = 60 mm), Thorlabs, USA) was used to generate a parallel optical beam of 2.24 mm diameter and optical power $\sim$ 1.1 mW that was projected onto the human cornea. The mechanical design of the telescope allowed for easy adjustment of the distance between lenses L1 and L2 to compensate for myopia and hyperopia in the imaged subjects and fine-tune the focusing of the imaging beam within the retina.

A custom visual stimulator comprised of a wheel with 4 LEDs (white, blue, green and red) was integrated with the OCT imaging probe through lens L3 (f = 50 mm, Thorlabs, USA) and a pellicle beam splitter (T/R ratio of 92/8, Thorlabs, USA). This design allows for the light from one of the LEDs to be focused at the pupil plane of the human eye in order to generate wide field of view illumination of the retina with almost uniform intensity (Maxwellian view). The custom visual stimulator was interfaced with a commercial electroretinography (ERG) system (Espion 2, Diagnosys LLC, USA), which served two purposes:

a) precise control of the timing, duration, intensity and frequency of visual stimulus; and

b) simultaneous collection of ERG and OCT recordings, so that the ERG recordings are used as a 'gold standard' to validate the optoretinography (ORG) traces extracted from the OCT images.

The reference arm of the OCT interferometer was comprised of a fiber collimator (achromat doublet, f = 10 mm, Thorlabs, USA), a custom-built 1 cm long water cell (WC) for crude compensation of water dispersion of the OCT imaging beam within the human eye, a custom dispersion compensation (DCP) unit comprised of BK7 prisms mounted on miniature translation stages (Edmund Optics, USA), a telescope (L4 and L5, achromat doublets (f4 = f5 = 60 mm), Thorlabs, USA), a focusing lens (L6, achromat doublet (f = 10 mm), Thorlabs, USA) and a mirror mounted on a miniature translation stage (Edmund Optics, USA). The telescope and the focusing mirror were mounted on a manual translation stage (Edmund Optics). Polarization controllers (PC) were used in both arms of the interferometer. The detection end of the OCT system was comprised of a commercially available spectrometer (Cobra-S 800, Wasatch Photonics, Durham, USA), interfaced with a line-scan CMOS camera (OCTOPLUS, Teledyne, USA) with a readout rate of 250 kHz.

This optical design resulted in axial resolution of $\sim 2.7\ \mu m$ in retinal tissue,and signal-to-noise ratio (SNR) of 98 dB, measured for 1.1 mW of power incident on the cornea and 250 kHz acquisition rate. The imaging power was well below the maximum permissible exposure (MPE) for safe retinal imaging as defined by the ANSI standard [140].

4.2.2 Subjects

This study was conducted on 4 healthy subjects (two females and two males, age $25 + -5$ years). The study has received full ethics clearance by the University of Waterloo's Office of Research Ethics and a written consent was obtained from all the participants. Prior to the OCT imaging sessions, all subjects underwent a standard clinical eye examination and only subjects with nearly perfect vision (minor correction of up to -1 Dioptres) and no ocular diseases or a history of epilepsy were included in this study. Both pupils were dilated by application of 1 drop of Tropicamide in each eye followed by ~ 30 minutes dark adaptation. A chin-forehead rest frame was used to position the left eye of the participants relative to the OCT imaging probe and a faint red LED light was used as a fixation target for the non-imaged eye.

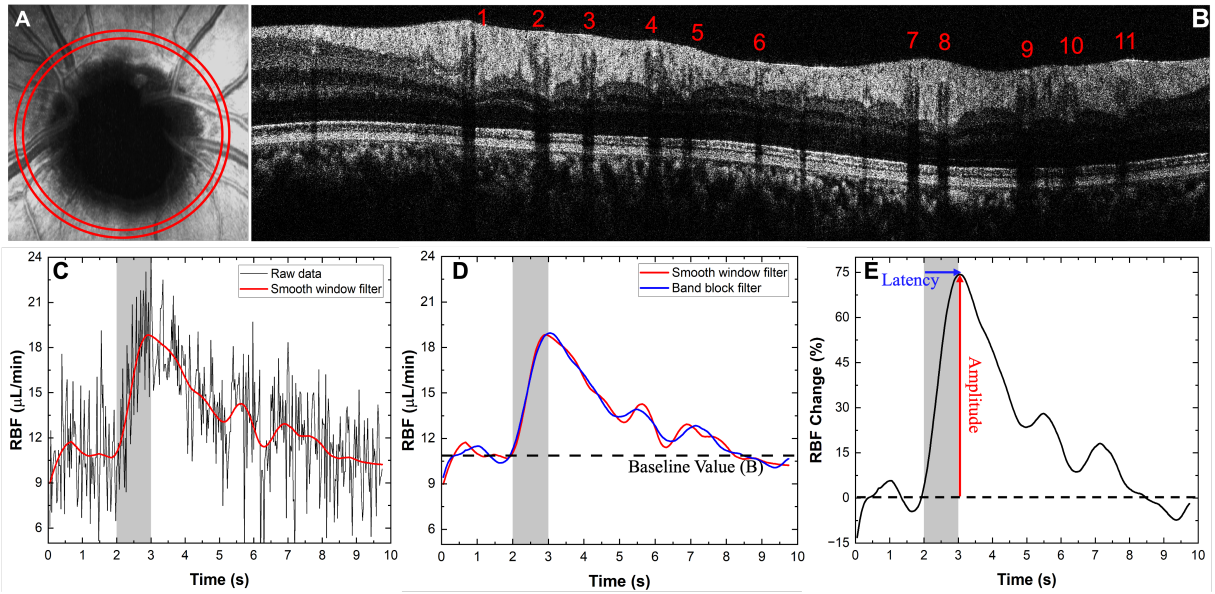


Figure 4.1: (A) *En face* projection of the Optic Nerve Head, where red lines show the approximate location of the OCT double circular scans. (B) Unwrapped circular B-scan, showing vessel cross-sections. (C) Plot showing raw RBF data (black curve), smoothed using a moving Savitzky-Golay function (red curve). (D) The smoothed curve is further band-blocked to remove fluctuations due to pulsatile motion (blue curve). (E) The mean of the first two seconds of RBF values serves as the baseline value to obtain RBF percentage change, characterized by Amplitude and Latency.

Flicker Stimulus Intensity ($cd.s/m^2$)	**Photoreceptors Bleaching** (%)
0.78	7.7
1.67	15.8
2.52	22.8
3.43	29.7
4.27	35.5
5.16	41.2
6.02	46.1

Table 4.1: Bleaching percentage for different stimulus intensities.

4.2.3 Image acquisition protocols and visual stimulation

A volumetric morphological dataset (1000 A-scans $\times$1000 B-scans) was acquired around the ONH from each subject prior to functional imaging to map the blood vessels on *en face* projection, as shown in Figure 4.1A. For D-OCT imaging, a double circular-scanning protocol around the ONH, introduced by Wang *et. al.* [62], was adapted for this study, as depicted in Figure 4.1A. Briefly, two concentric circles centered around the ONH of radii $\sim 1.8mm$ and $\sim 2.0mm$, were acquired over a period of 10 seconds. 3000 A-scans were acquired per B-scan such that there is an overlap between consecutive A-scans, which resulted in a total of 800 B-scans, of which 400 B-scans corresponded to the circle with smaller radii and 400 to the circle with larger radii. Double circle scanning protocol allows for the measurement of the Doppler angle between the blood vessel and the imaging beam, which is necessary for determining the absolute retinal blood flow. The imaging protocol was comprised of 2 seconds of dark (baseline) recording was followed by 1 second of 10 Hz flicker stimulation at a 10% duty cycle, followed by another 7 seconds of post-stimulus recording to observe the recovery of the blood flow. This stimulation protocol was carried out for 6 steps of the stimulus intensity. The ERG system was used to control the stimulation parameters such as the intensity, duration, frequency, pattern as well as timing of the stimulation. An external control box was added to control the LED colour and the current flowing through the LEDs. Only white stimulus was used to conduct this study. Table 4.1 depicts the bleaching percentage for the various stimulus intensities used for this study, calculated based on the method described by Rushton and Henry [141].

4.2.4 Data analysis

Raw OCT data were processed to generate dispersion compensated cross-sectional images of the retina from the circular scans. A representative image is shown in Figure 4.1B and the retinal blood vessels were numbered. Figure 4.1C shows a representative trace of the RBF measured from one blood vessel from the OCT scan shown in Figure 4.1B (black line). The high frequency pattern in the traces is due to the presence of speckle since OCT is based on detection of partially coherent light. To generate a smoother curve (Figure 4.1C) the original data was zero-padded by 3× to enable precise frequency filtering. A smoothing filter with a moving window (Savitzky-Golay) was used to filter out the high frequency component of the signal (red line in Figures 4.1C and 4.1D). Subsequently, a band-block filter (0.4 - 1.3 Hz) was employed to remove the subject's heart rate-related pulsatile fluctuations, resulting in the blue curve in Figure 4.1D. The following formula was used to calculate the change of RBF in percentage:

$$RBFChange\,(\%) = \frac{SignalRBFvalue\,(A) - BaselineRBFValue\,(B)}{BaselineRBFValue\,(B)} \times 100 \qquad (4.1)$$

Here, the signal RBF value corresponds to the RBF value obtained from each blood vessel in each B-scan and the baseline RBF value corresponds to the mean RBF value during the 2 second pre-stimulus period. A similar analysis was conducted to characterize the retinal blood vessel diameter (RBVD) response in the axial and lateral directions, as given by the following equation:

$$RBVDChange\,(\%) = \frac{SignalRBVDvalue\,(A) - BaselineRBVDValue\,(B)}{BaselineRBVDValue\,(B)} \times 100 \quad (4.2)$$

Here, the signal RBVD value corresponds to the value of the vessel diameter in one direction in a B-scan and the baseline RBVD value is determined by taking average of the vessel diameter fluctuations over the 2 seconds of pre-stimulus recording. Unpaired t-test was deployed to verify the statistical significance of the amplitude values relative to the maximum change in baseline values. All results had p-value < 0.01.

The transient RBF changes were characterized by two quantities: the peak amplitude (red arrow in Figure 4.1E) and the peak latency measured relative to the onset of the visual stimulus (blue arrow in Figure 4.1E).

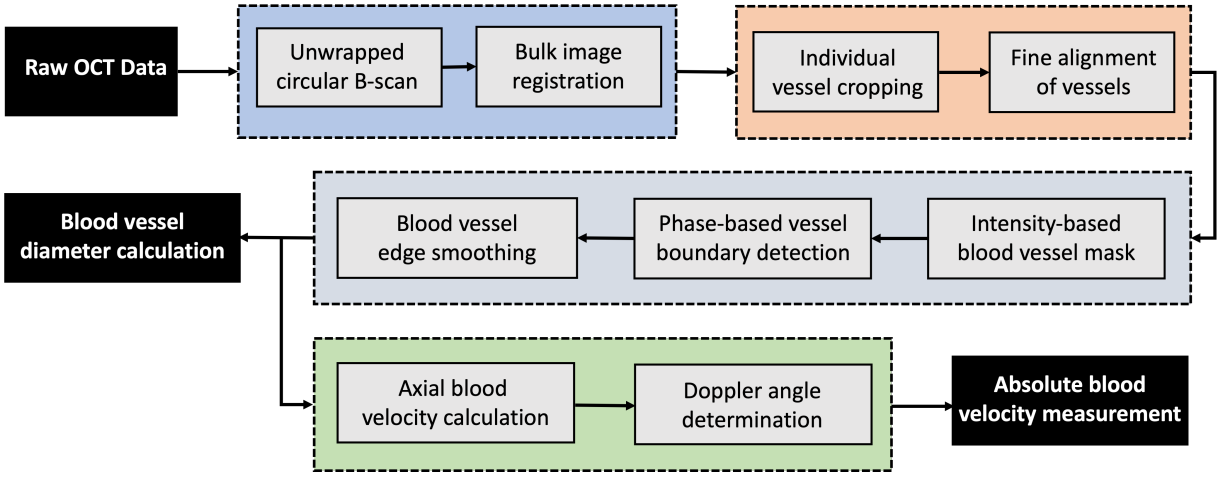


Figure 4.2: Flow-chart depicting the retinal blood flow and retinal blood vessel diameter processing algorithm.

4.2.5 Algorithms

Custom image processing algorithms were developed in MATLAB for extracting time dependent RBF and RBVD changes from the OCT B-scans. Figure 4.2 shows the flow chart for the two measurements. The raw OCT data acquired by the combined OCT+ERG system was first processed to generate unwrapped dispersion-compensated circular B-scans (representative image shown in Figure 4.1B) as well as the phase information for each of the B-scans [52]. To compensate for the involuntary human eye motion due to breathing, heartbeat, and ocular muscle twitching which resulted in misalignment between consecutive OCT B-scans, a sub-pixel image registration method was employed [142].

Blood vessels were manually selected from a tomogram by looking at the shadows cast by the blood vessels in the deeper layers of the retina as blood particles are highly reflective. The width of these shadows is correlated to the diameter of the blood vessels and as the lumen of the blood vessels is not reflective, it is easier to distinguish the blood vessel wall from the blood particles. Since a fine-tuned alignment of individual blood vessels was required to effectively extract the blood flow information, each of the blood vessels was cropped from all B-scans in the time series using a semi-automated algorithm and aligned based on its surrounding tissue by correlation.

This cropped data was used to generate an intensity-based mask for the blood vessel by setting a threshold value. Next the mask was fine-tuned this mask using the phase-resolved information, and its edges were smoothed using a Gaussian filter. The mask, thus obtained,

was used to extract the blood velocity information based on the phase shift between the adjacent A-scans and the blood vessel diameter information in the horizontal (lateral) as well as the vertical (axial) direction were used to calculate the blood vessel's cross-section. The coordinates of the blood vessels in these images were used to extract the Doppler angle between the blood vessel and the imaging beam, and the vessel cross-sectional area was corrected by the Doppler angle and then used to extract the RBF values for individual vessels.

4.3 Results

4.3.1 Functional RBF changes

The RBF response of each of the blood vessels labeled in Figure 4.1B was measured and characterized using the parameters depicted in Figure 4.1E. The vessels exhibited behavior that was generally classified into two groups: Type 1 and Type 2. This categorization of vessels also corresponded to the two directions of phase variance exhibited by the vessels. Therefore they can be characterized into arteries and veins by considering the phase shift between heart rate related peaks in the RBF traces measured from arteries and veins, with the veins showing a lag in phase with respect to the arteries. Based on the phase shift observed between the two vessel types, type 1 was identified as arteries and type 2 as veins. The blood vessel classification results were confirmed through an independent method. Coloured fundus photos of the imaged retina were provided to two ophthalmologists who were asked to identify independently the type of retinal blood vessels (artery or vein) from the photos. The results from this test matched with the identification of the retinal blood vessels using the phase method based on OCT images.

Figure 4.3 summarizes changes to the RBF measured from arteries and veins in response to 10 Hz, white-light flicker stimulation. Figures 4.3A and 4.3D show representative traces of the fractional RBF changes acquired from arteries and veins respectively at baseline (dark recordings, black lines) and three different intensities of the visual stimulus (red, blue and green curves). Transient RBF changes measured from arteries were very fast and peaked very close to the stimulus off-set. The fractional RBF change showed nearly 100% peak magnitude increase relative to baseline with small variations of the peak magnitude as a function of the stimulus intensity. The arterial RBF change dropped to a minimum value at ~ 3 seconds relative to the stimulus onset. Afterwards, the RBF oscillated for the rest of the recording time.

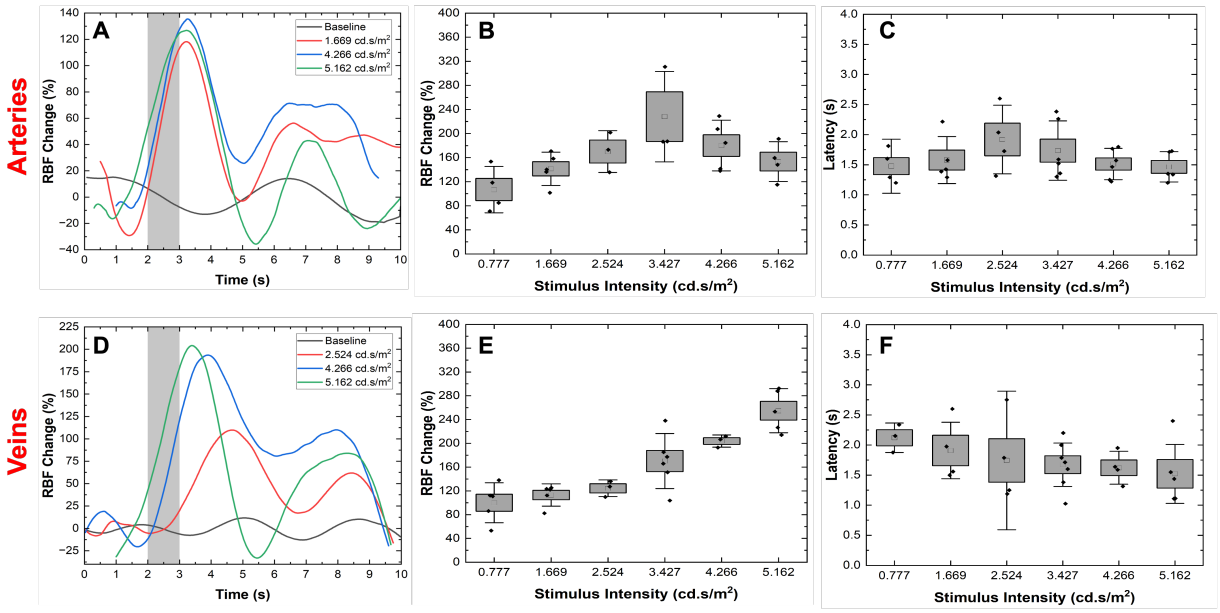


Figure 4.3: (A) Fractional RBF change measured from an artery at baseline (black curve) and in response to 10 Hz white-light flicker stimulation of increasing intensities (red, blue, and green curves). (B) Average RBF peak magnitude measured in retinal arteries in response to increasing stimulus intensity. (C) Average RBF peak latency response measured in arteries in response to 10 Hz white-light flicker stimulation. (D) Fractional RBF change measured from a vein at baseline (black curve) and in response to 10 Hz white-light flicker stimulation of increasing intensities (red, blue, and green curves). (E) Average RBF peak magnitude measured in retinal veins in response to increasing stimulus intensity of 10 Hz white-light flicker stimulation. (F) Average RBF peak latency measured in veins in response to 10 Hz white-light flicker stimulation.

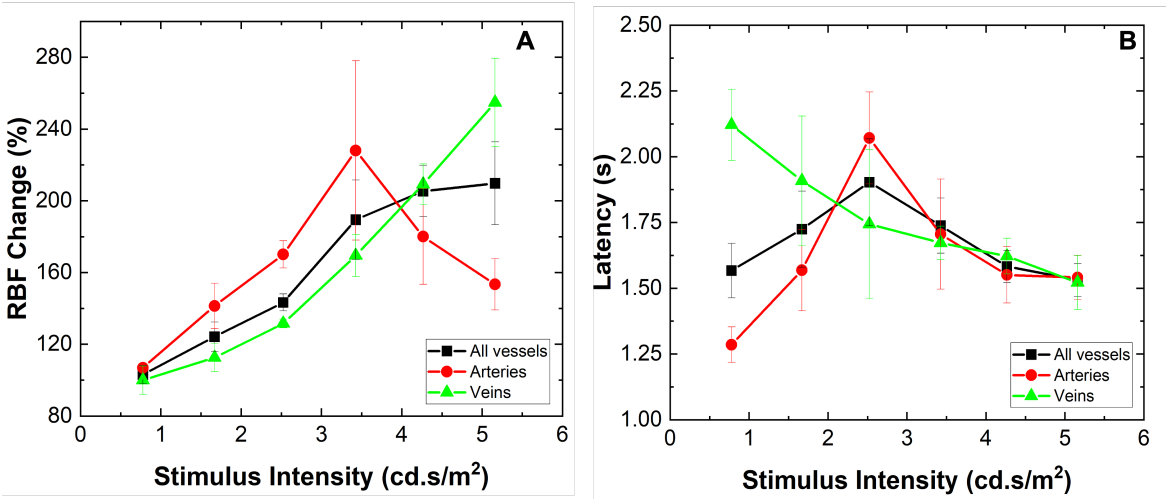


Figure 4.4: (A) Summary of the RBF peak change in arteries (red plot), veins (green plot), and total blood flow behavior (black plot) in response to increasing stimulus intensity of 10 Hz white-light flicker stimulation. (B) RBF peak latency trend in arteries (red curve), veins (green curve), and overall vessel response (black curve) to increasing stimulus intensity of 10 Hz white-light flicker stimulation. The error bars represent the Standard Error of the mean values.

Fractional RBF changes measured in retinal veins exhibited different behavior. The peak magnitude of the RBF change increased with the stimulus intensity, while the peak latency decreased progressively.

Figures 4.3B and 4.3E show statistical data for the peak magnitude of the RBF change as a function of the stimulus intensity measured from arteries and veins respectively, and analyzed from multiple recordings from one subject. The arterial RBF change shows almost linear increase with the stimulus intensity up to intensity of $\sim 3.4 cd.s/m^2$. Further increase in the stimulus intensity resulted in almost linear decrease of RBF peak magnitude. In contrast, the peak magnitude of the RBF changes measured in veins increased non-linearly up to the maximum flash intensity of $\sim 5.2 cd.s/m^2$ used in this study and showed no trend for saturation.

Figures 4.3C and 4.3F show statistical data for the peak latency of the RBF change as a function of the stimulus intensity measured from arteries and veins respectively. There is no significant trend for the arterial latency, while the latency of the peak RBF change shows a negative trend with the increase of the stimulus intensity.

Figure 4.4 shows an overview of the RBF behavior of all retinal blood vessels around the

Intensity ($cd.s/m^2$)	**Subject 1** **(Mean ± SE)**	**Subject 2** **(Mean ± SE)**	**Subject 3** **(Mean ± SE)**
0.777	103.06 ± 5.10	164.24 ± 11.60	167.62 ± 20.55
1.669	124.20 ± 8.18	171.16 ± 21.26	
2.524	143.30 ± 4.73	174.9 ± 15.71	199.27 ± 19.33
3.427	189.46 ± 22.14		
4.266	205.4 ± 14.17	179.59 ± 23.04	221.59 ± 33.12
5.162	209.74 ± 23.09	173.05 ± 15.57	
6.015		171.74 ± 13.92	225.60 ± 47.98

Table 4.2: Peak RBF change values (mean and standard error) for different subjects using various stimulus intensities in the study.

ONH (black lines) compared to the behavior of arteries (red lines) and veins (green line). The peak magnitude of the RBF fractional change (Figure 4.4A) initially increases with the stimulus intensity and plateaus for stimulus intensity $> 3.5cd.s/m^2$. The peak RBF change measured in arteries shows almost linear initial increase with stimulus intensity, peaks at intensity $\sim 3.5cd.s/m^2$ and then decreases linearly. The peak RBF change measured in veins shows non-linear increase with the stimulus intensity . The RBF peak latency in both arteries and the average over all vessels shows initial increase with the stimulus intensity, which peaks for stimulus intensity of $2.5cd.s/m^2$, then decreases almost linearly. In contrast, the RBF peak latency in veins decreases non-linearly with the increase of the stimulus intensity.

Table 4.2 presents statistical values for the peak RBF changes measured from 3 of the study subjects for different stimulus intensity values. The data was averaged over all retinal blood vessels in the circular scans and over 4 recordings for each stimulus intensity value.

Table 4.3 presents statistical values for the peak RBF latency measured from 3 of the study subjects for different stimulus intensity values. The data was averaged over all retinal blood vessels in the circular scans and over 4 recordings for each stimulus intensity value.

4.3.2 Functional RBV Diameter changes

In addition to RBF changes the visual stimulus induced vasoconstriction and vasodilation in the retinal blood vessels. Figure 4.5 shows transient changes in the retinal blood vessels diameter (RBVD) measured in one artery (Figures 4.5A-4.5D) and one vein (Figures 4.5E-4.5H) in response to flicker stimulation of different intensities. The black curves correspond

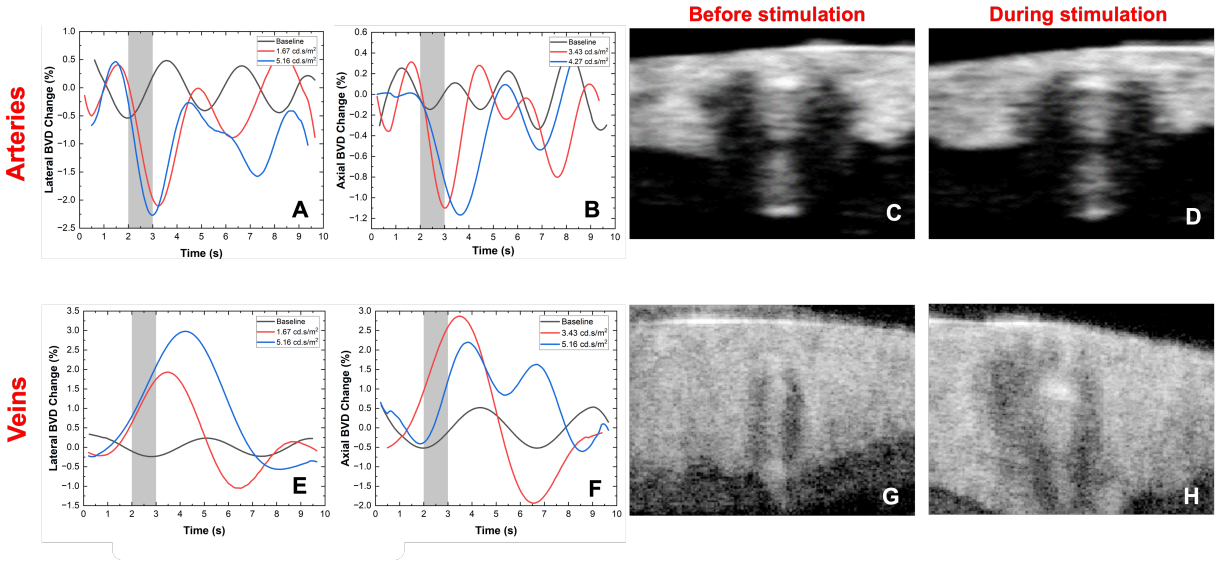


Figure 4.5: (A) Retinal blood vessel diameter changes in the lateral direction in an artery in response to varying stimulus intensities of 10 Hz white-light flicker stimulation (red and blue curves). (B) Retinal blood vessel diameter changes in the axial direction in an artery in response to varying stimulus intensities of 10 Hz white-light flicker stimulation (red and blue curves); the black curves in these figures represent the response of the blood vessel in the absence of flicker stimulation. (C) Time-averaged vessel cross-section of an artery before flicker stimulation. (D) Time-averaged vessel cross-section of an artery during flicker stimulation. (E) Retinal blood vessel diameter changes in the lateral direction in a vein in response to varying stimulus intensities of 10 Hz white-light flicker stimulation (red and blue curves). (F) Retinal blood vessel diameter changes in the axial direction in a vein in response to varying stimulus intensities of 10 Hz white-light flicker stimulation (red and blue curves); the black curves in these figures represent the response of the blood vessel in the absence of flicker stimulation. (G) Time-averaged vessel cross-section of a vein before flicker stimulation. (H) Time-averaged vessel cross-section of a vein during flicker stimulation.

Intensity ($cd.s/m^2$)	**Subject 1 (Mean ± SE)**	**Subject 2 (Mean ± SE)**	**Subject 3 (Mean ± SE)**
0.777	1.57 ± 0.10	1.78 ± 0.12	1.51 ± 0.12
1.669	1.72 ± 0.15	1.71 ± 0.09	
2.524	1.90 ± 0.17	1.68 ± 0.10	1.49 ± 0.14
3.427	1.74 ± 0.10		
4.266	1.58 ± 0.06	1.6 ± 0.10	1.29 ± 0.11
5.162	1.53 ± 0.06	1.58 ± 0.09	
6.015		1.50 ± 0.09	1.63 ± 0.15

Table 4.3: RBF peak latency values (mean and standard error) for different subjects using various stimulus intensities in the study.

to dark recordings (baseline). The transient changes in the RBVD were evaluated in both the lateral and axial directions. Figures 4.5A and 4.5B show a fast initial vasoconstriction of the artery that is initiated with the onset of the visual stimulus, peaks close to the stimulus off-set and occurs simultaneously in the lateral and axial directions. However, vasoconstriction is not uniform in the lateral and axial directions: the RBVD peak magnitude is $\sim 2\%$ in the lateral direction and only $\sim 1\%$ in the axial direction. Figures 4.5C and 4.5D show time-averaged OCT images of a cross-section of a retinal artery before and during visual stimulation where the initial vasoconstriction is clearly visible.

Figures 4.5E and 4.5F show vasodilation of a retinal vein caused by flicker stimulation of different intensities in the lateral and axial directions respectively. The black curves correspond to dark recordings (baseline). While the vasodilation is initiated with the onset of the flash, its peak latency is dependent on the stimulus intensity.

Figures 4.5G and 4.5H are the time-averaged snapshots of the vessel cross-section before and during the flicker stimulation, respectively. The vessel response in veins can be characterized as anisotropic similar to the trend observed in arteries, with a greater change measured in the lateral direction.

Figure 4.6 shows the RBVD response to flicker stimulation as a function of the vessel diameter. Figures 4.6A and 4.6B show the response of the arterial vessel constriction with an increase in the vessel diameter in the lateral and axial directions, respectively. In both figures, the black dots show the mean value for individual vessel response to a flicker stimulus of $3.427 cd.s/m^2$ intensity and the black line represents the straight-line fit. The red dots in both figures show mean values of individual vessel responses averaged over multiple recordings to a flicker stimulation of $5.162 cd.s/m^2$ intensity and the red line is the straight-line fit for this behavior. Figures 4.6A and 4.6B show two general trends in the

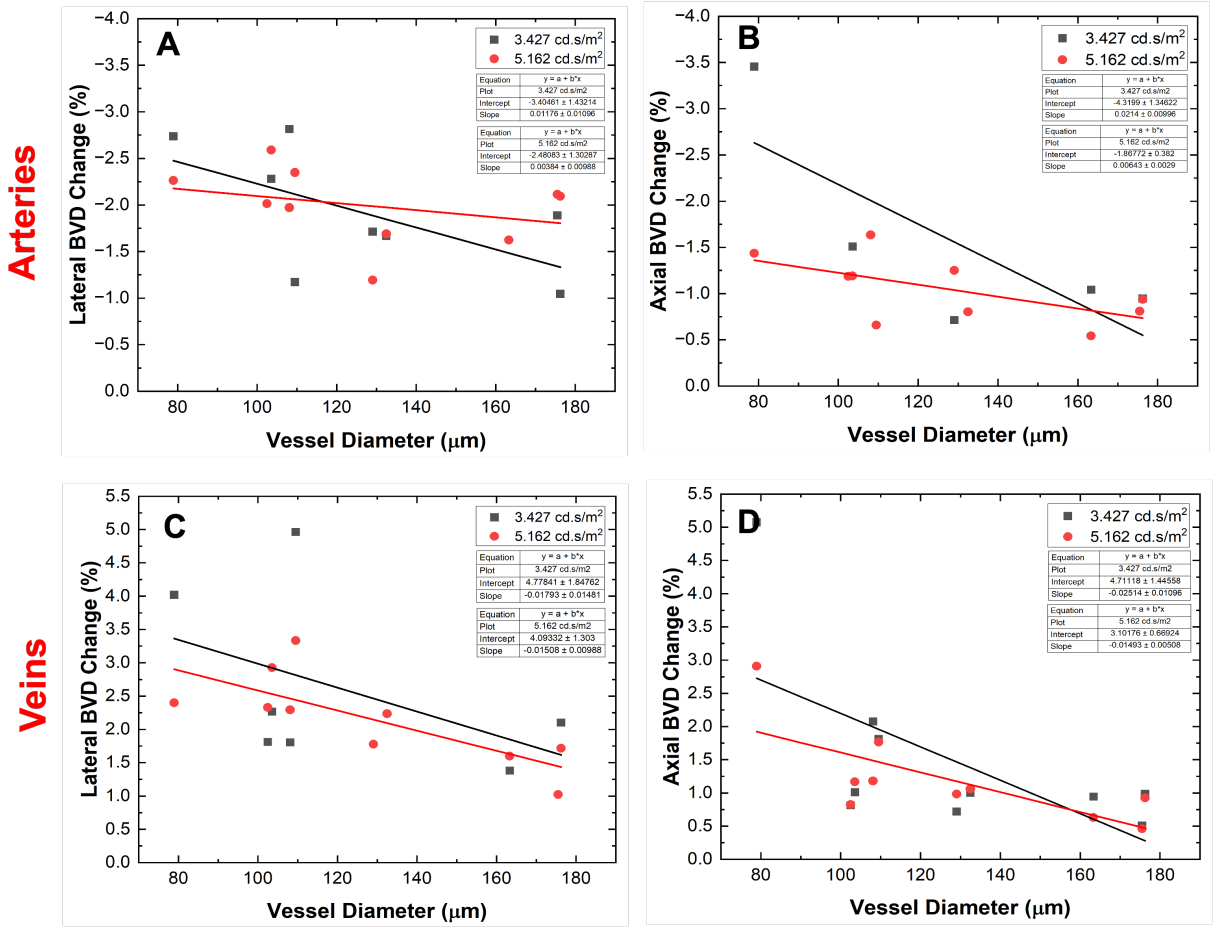


Figure 4.6: (A) Retinal blood vessel diameter changes in the lateral direction in arteries as a function of the vessel diameter in response to increasing stimulus intensity for 10 Hz of white-light flicker stimulation. (B) Retinal blood vessel diameter changes in the axial direction in arteries as a function of the vessel diameter in response to increasing stimulus intensity for 10 Hz of white-light flicker stimulation. (C) Retinal blood vessel diameter changes in the lateral direction in veins as a function of the vessel diameter in response to increasing stimulus intensity for 10 Hz of white-light flicker stimulation. (D) Retinal blood vessel diameter changes in the axial direction in veins as a function of the vessel diameter in response to increasing stimulus intensity for 10 Hz of white-light flicker stimulation.

RBVD response to the visual stimulation:

a) smaller vessels show slightly larger percentage change in constriction; and

b) the vasoconstriction of the retinal arteries is less dependent on the blood vessel diameter for higher intensity of the visual stimulus.

Figures 4.6C and 4.6D show the venous response with an increase in the vessel diameter in the lateral and axial directions, respectively. Similarly, the black dots here represent mean values of individual vessel responses averaged over multiple recordings to a flicker stimulation of $3.427 cd.s/m^2$ and the black line shows the fitted plot. The red dots show the mean values of individual vessel responses averaged over multiple recordings to flicker stimulation of $5.162 cd.s/m^2$ and the red line shows the fitted plot. Figures 4.6C and 4.6D show two general trends in the RBVD response to the visual stimulation:

a) smaller vessels show slightly larger percentage change in dilation; and

b) the vasodilation of the retinal veins is less dependent on the blood vessel diameter for higher intensity of the visual stimulus.

4.3.3 ERG responses

Figure 4.7 summarizes the electrical response of a healthy human retina to the increasing intensity of 10 Hz white-light flicker stimulation. Figure 4.7A shows the ERG traces in response to 10 Hz white-light flicker stimulation at intensities $0.312 cd.s/m^2$ (the black curve), $1.72 cd.s/m^2$ (the red curve) and $3.44 cd.s/m^2$ (the blue curve). The magnitude of the a-wave and b-wave peaks increases with the increase of the stimulus intensity which is in agreement with published ERG studies on healthy human subjects.

4.4 Discussion

Results from this study showed significant and transient increase in RBF measured in the vicinity of the ONH in response to flicker stimulation in healthy human subjects. These results agree, in general, with the results from similar studies conducted by other research groups. Aschinger *et. al.* detected a change of $\sim 48\%$ in RBF after 2 minutes of 12.5 Hz low-intensity flicker stimulation ($\sim 1.96E-04 W/cm^2$) at 530-600 nm range, where

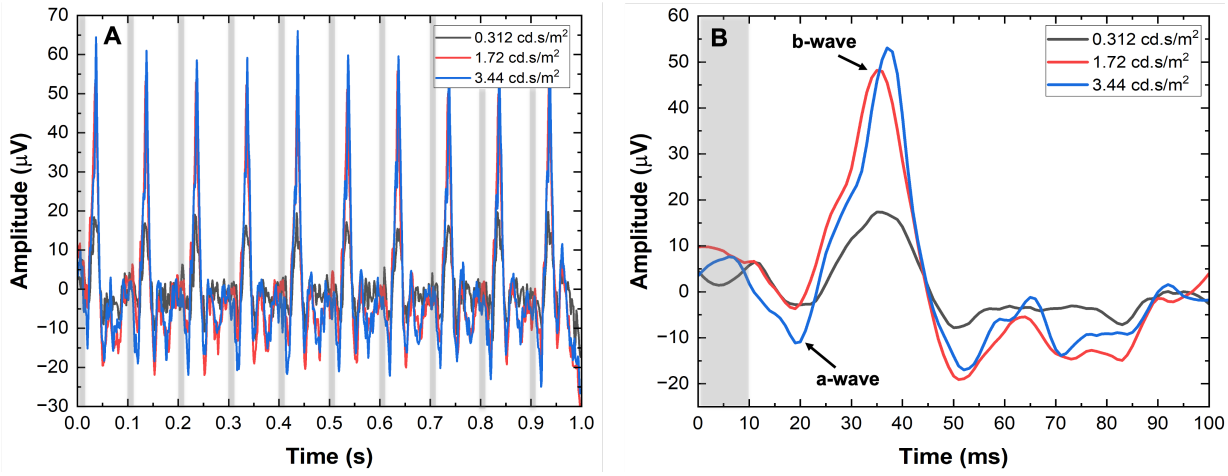


Figure 4.7: (A) ERG traces in response to increasing intensity of 10 Hz white-light flicker stimulus. (B) Zoomed in ERG response depicting the negative a-wave and the first positive b-wave.

the response from individual blood vessels ranged between 34% and 66% [122]. Kallab *et. al.* reported an increase of $\sim 40\%$ in an arteriovenal pair by using 12 light-emitting diode ring at 7 Hz flicker stimulation and $\sim$ 450 lx [71]. Zhong *et. al.* reported an increase of $\sim 65\%$ in response to local retinal flicker stimulation in healthy human subjects using a mini liquid crystal display between 0.6 lux and 6.6 lux at 10 Hz [148].

Kondo *et. al.* reported an increase of 256% in RBF change in blood vessels around ONH in cats in response to wide-field flicker stimulation [13]. Riva *et. al.* observed an initial increase in RBF% change as stimulus intensity increases and plateaus at $\sim 250\%$ at higher stimulus intensities [149]. These results show an RBF change very similar to this study, possibly due to the similarity in the dark-adaptation technique used to conduct the experiments.

Zhong *et. al.* demonstrated that the area of flicker stimulation plays a crucial role in the response of RBF to stimulation [148]. Tan *et. al.* demonstrated in rat retina that the pattern of stimulation (single flash v/s flicker) plays an important role in the detected response as well [67]. This could also explain the higher RBF response observed in this study since a Maxwellian illumination was achieved at the surface of the retina, instead of a pattern illumination used in the majority of the other studies. Results from this study also showed that prolonged stimulation, as has been used for most of the previous studies, is not necessary to observe transient changes in RBF. Our study shows that short flicker stimulation of only 1 second duration can result in fast transient changes in the RBF that

tend to peak close to the stimulus off-set. Therefore, an OCT system of moderately high image acquisition rate (250 kHz for our study) offers the necessary temporal resolution for measuring fast transient RBF changes in the human retina caused by visual stimulation.

Results from our study show that retinal arteries exhibit a greater initial RBF% change in response to flicker stimulation compared to retinal veins. This aligns with the existing literature suggesting that arteries show a higher response than veins at lower stimulus intensities [15, 64, 65, 96]. Since arteries actively pump the blood to the organs and tissues, it is reasonable that they show a stronger response as compared to the veins, which shows lower pulsatility and more stable baseline RBF changes [62, 150, 151]. Moreover, arterial vessel walls contain more smooth muscle cells, which respond dynamically to the metabolic demands of the tissue via astrocytes and pericytes [4, 7, 152]. In our study, we measured an initial vasoconstriction of the retinal arteries, followed by vasodilation. Since blood behaves similarly to a Newtonian fluid, the vasoconstriction results in a temporary increase in velocity of the red blood cells and therefore in the RBF.

Previous studies have observed greater responses in retinal blood vessels with smaller diameters to flicker stimulation [15, 122]. While no such analysis was conducted for the RBF% change, the response of the retinal blood vessel diameter (RBVD) measured in our study aligns well with these studies, showing a larger percentage change in the smaller vessels in both lateral and axial directions. Additionally, for retinal blood flow increase as high as $\sim 200\%$, a very small change in the vessel diameter is observed in larger blood vessels indicating that vascular resistance is significantly decreased in smaller vessels.

Results from our study show that the RBF does not return to baseline immediately after the transient increase caused by the visual stimulation, which is supported by the results reported by Wang *et. al.*, where they have observed an increase of $\sim 22\%$ in RBF $10 - 15$ seconds after 30 seconds of flicker stimulation. Moreover, a secondary increase in RBF was also observed in rat retina by Tan *et. al* [67]. This can also be explained by the elastic nature of the walls of blood vessels, which resist rapid changes in the blood flow.

Based on the trend observed in the retinal arteries, it is natural to expect that the RBF% change in veins would decrease with the increase of the stimulus intensity, as veins return the blood supplied to the tissue back to the heart. Based on the principle of mass conservation, the volume of the blood supplied to the tissue must equal the volume of the blood returned to the heart.

Son *et. al.* reported anisotropic diameter changes in the retinal blood vessels in response flicker stimulation [153], which aligns with the results from this study. Blood vessels tend to show differential response based on the location of the blood vessel, as the surrounding tissue could allow more flexibility in one direction than the other [154]. Moreover, it has

been reported that the distribution of smooth muscle cells is not even in the blood vessel wall, which could contribute to the anisotropic behavior [155–157].

ERG traces were recorded in this study to confirm the proper visual stimulation of the retina and to confirm that the transient RBF changes measured with OCT are indeed associated with increased neuronal activity in the retina. In future studies, RBF and ERG data acquired simultaneously with the combined OCT+ERG system can assist vision scientists with exploring neurovascular coupling in the healthy and diseased retina.

Several limitations need to be considered for this study. In humans, the retinal blood vessel pattern is unique to each individual, unlike the rat retina where the vessels alternate between the arteries and the veins, which makes it difficult to distinguish arteries from the veins in human subjects. Additionally, the blood vessel pattern is very sensitive to involuntary eye motion where a slight shift in the lateral direction changes both the Doppler angle between the blood vessel and the imaging beam, and also the location at which the vessels are being imaged. It poses a challenge to the vessel diameter measurements as well. At times, vessels are imaged at the vessel bifurcation and a slight lateral motion changes the imaging location to the merged vessel. In such cases, it becomes very difficult evaluate correctly the visually evoked RBF response without the use of additional techniques.

With the current version of the image processing algorithms, processing the OCT images to extract RBF traces from about 10 blood vessels per OCT dataset takes a long time ($\sim$ 2 hours), although the algorithms are already semi-automated. The algorithms are not able to completely account for large saccades in the human eye due to several contributing factors, without the use of machine learning and/or adaptive optics components. Additionally, the frequency filtering method used to remove the vessel pulsatile fluctuations can modify the shape of the peak of the RBF since some of the frequencies are blocked from the signal. As a result, the RBF response sometimes appears to start before the onset of flicker stimulation. Future work on this project will focus in part on the development of novel image processing algorithms based on machine learning that can speed up the data processing. Novel filtering approaches of the RBF data will also be explored.

4.5 Conclusions

In conclusion, a combined OCT+ERG system has been developed to utilize the D-OCT technique to study human retinal blood flow changes in response to flicker stimulation. The results from this study show that flicker stimulation in healthy human subjects leads to a significant increase in RBF and that the behavior of the RBF and RBV diameters in

response to stimulation are dependent both on the stimulus intensity and the vessel type (artery or vein).

Chapter 5

Color and frequency dependence of flicker induced transient retinal blood flow changes in healthy human retina measured with OCT

Notes and Acknowledgments

This chapter summarizes the preliminary results from an ongoing study that aimed to investigate the effects of temporal and chromatic variations of flicker stimulus on retinal blood flow in the larger blood vessels around the optic nerve head in healthy humans, measured with OCT. The content of this chapter is based on the following manuscript in preparation:

Dhaliwal K, Hudson C, Wright T, Ballios B, Bizheva K. "Color and frequency dependence of flicker induced transient retinal blood flow changes in healthy human retina measured with OCT".

Kostadinka Bizheva conceived the study and provided the study materials. **Chris Hudson**, **Brian Ballios** and **Tom Wright** contributed to the organization of the study.

Khushmeet Dhaliwal acquired the OCT data.

Khushmeet Dhaliwal wrote the algorithm for retinal blood flow detection and blood vessel segmentation.

Khushmeet Dhaliwal processed the experimental data.

Khushmeet Dhaliwal analyzed the experimental results.

Khushmeet Dhaliwal, **Kostadinka Bizheva**, **Chris Hudson** all contributed to the interpretation of the results.

Khushmeet Dhaliwal wrote the first draft.

5.1 Introduction

The retina is a multi-layered tissue located at the posterior end of the eye. As an extension of the central nervous system, the retina is comprised of neurons that contain photosensitive pigments essential for visual acuity [92]. As a highly metabolically active tissue, the retina relies on its vasculature to meet the cellular demands for oxygen and nutrients to maintain normal visual function [90, 91]. The response of the retinal vasculature to neuronal stimulation, resulting in time-dependent changes in the retinal metabolic demand, is referred to as neurovascular coupling [4, 11, 12]. Disruptions in the neurovascular coupling are linked to retinal neurodegenerative diseases such as glaucoma [20, 21], retinitis pigmentosa [25, 26], age-related macular degeneration [23, 24], and diabetic retinopathy [30, 31]. Therefore, studies of neurovascular coupling are essential for gaining a better understanding of how neurodegenerative retinal diseases originate and progress. Such studies may identify biomarkers that would aid the early diagnosis of potentially blinding retinal diseases.

Several imaging modalities, including fundus photography [34, 48], scanning laser ophthalmoscopy [40], and clinical ophthalmoscopy [158], have been used to image the human morphology and vascular network. While these imaging modalities can visualize and characterize structural damage in the human retina, most of these methods lack the ability to provide clinically useful information about the normal or abnormal retinal function associated with retinal diseases. Furthermore, by the time structural damage becomes detectable with such clinical imaging modalities, irreversible damage to the retina has already occurred. Technologies such as laser Doppler flowmetry [35, 36], adaptive optics scanning laser ophthalmoscope (AO-SLO) [41, 96], fluorescein angiography [42, 44], and retinal vessel analyzers [15, 47] have been used in the past to examine transient responses of the healthy and diseased retinal vasculature to visual stimulation. However, these technologies often provide only qualitative information or require expensive equipment, which is not feasible in routine clinical settings.

Therefore, an accessible, non-invasive imaging modality that offers quantitative information about transient, visually evoked changes in the retinal blood flow is desirable. Over the past 3 decades, Optical Coherence Tomography (OCT) has emerged as a powerful, clinically-adopted imaging modality for ophthalmic applications, as it allows for non-contact, non-invasive, high-speed, high-resolution *in vivo* structural and functional imaging of the human retina [54]. Doppler OCT, a functional extension of OCT, is especially promising for analyzing blood flow dynamics *in vivo* [58, 62]. This technology provides both morphological information about the retinal layered structure and can quantify transient changes in the retinal blood flow based on the Doppler shift principle.

Previous studies have investigated the response of the retinal blood flow to visual stim-

ulation in the human and animal retina, where it was observed that flicker stimulation leads to increased retinal blood flow and induces vasodilation in the retinal blood vessels [15, 67, 71, 122, 148, 159, 160]. In humans, Wang *et. al.* reported an increase in retinal blood flow (RBF) approximately 30 seconds after 15 seconds of 8 Hz flicker stimulation using white light emitting diodes arrayed in a ring [65]. However, this imaging protocol is impractical for clinical studies as patients and study participants cannot keep their eyes open for longer than 10s and blinking and eye motion can corrupt the OCT images. Warner *et. al.* observed an average increase of $\sim 12\%$ in retinal blood velocity in small blood vessels in response to full-field 10 Hz flicker stimulus at mean luminance of 3.7 lx [96], while Riva *et. al.* observed an RBF change as high as 250% in dark-adapted cats [149]. However, most of these studies were conducted for a fixed stimulus frequency and a single color of the stimulus.

The human retina contains three types of cones (S, M, and L) and rods, each sensitive to a specific range of wavelengths [90]. Given this spectral sensitivity, it is likely that retinal blood flow changes depend on specific characteristics of the stimulus used to elicit a photoreceptor response. In humans, there are two known visual pathways that process these signals: the parvocellular and magnocellular pathways [161, 162]. The parvocellular system, typically associated with retinal ganglion cells with smaller cell bodies, is responsible for carrying the small, slow color-sensitive information (low temporal frequency, high spatial frequency) and is mainly M- and L-cone driven. In contrast, the magnocellular system, linked to retinal ganglion cells with larger cell bodies, processes large, fast, color-insensitive information (high temporal frequency, but low spatial frequency) [162] and is mainly rod driven. In a study by Riva *et. al.* [163], retinal blood vessel responses were found to depend on the activation of these pathways, with distinct blood flow responses to luminance versus chromatic stimuli. However, this methodology involved over 30 seconds of stimulation and prolonged recording times, limiting its clinical adaptability.

Studying the RBF response to visual stimuli of varying wavelengths and flicker frequencies could aid the better understanding of neurovascular coupling in the human retina. It can also provide valuable insights into how certain retinal diseases affect rod versus cone function and the respective transient, visually evoked changes in the RBF. Currently, the effect of flicker stimulation with different colors on the photoreceptor responses and related neurovascular coupling remains largely unexplored. Furthermore, the use of different stimulation frequencies to isolate cone responses by saturating rod activity has not been extensively studied. Better understanding of the spectral and frequency dependence of neurovascular coupling in the human retina may uncover early biomarkers for various potentially blinding retinal diseases.

The main goal of this study is to characterize transient RBF changes measured near

the optic nerve head (ONH) of the healthy human retina in response to visual stimuli with different colors (white, red, blue, and green) and frequencies (10 Hz and 30Hz) by using Doppler OCT. By targeting specific photoreceptor types, we seek to provide a more detailed understanding of visually evoked changes in the retinal blood flow dynamics and their potential role as predictive biomarkers for early diagnosis of potentially blinding retinal diseases.

5.2 Methods

5.2.1 OCT system

The combined OCT+ERG system used for this study has been previously described in section 3.2.1 of this thesis. In brief, a broad bandwidth superluminescent diode-based light source operating at $800nm$ was used to power up a fiber-based research-grade OCT system, providing an axial resolution of $\sim 2.7\mu m$ in tissue. The optics in the sample arm was configured such that a parallel beam of $\sim 2.3mm$ and 1.1 mW optical power was incident on the cornea, in accordance with the maximum permissible exposure set by ANSI standards [140]. A custom-built visual stimulator was integrated into the human retina imaging probe to generate Maxwellian illumination at the surface of the retina. The stimulus color (red, green, blue, and white) was manually controlled as the 4 LEDs are mounted on a rotating wheel, while the timing, frequency, and pattern of the stimulus were controlled by using a commercial electroretinography (ERG) system (Diagnosys LLC, USA).

5.2.2 Imaging Protocol and processing

The imaging protocol as well as the processing algorithms used for this study were also previously described in section 4.2. Briefly, a concentric circular protocol centered on the Optic Nerve Head (ONH) was utilized for this study [62]. A total of 800 B-scans were acquired over a time period of 10 seconds, with each B-scan consisting of 3000 A-scans. The first 2 seconds were recorded as the pre-stimulus period, followed by 1 second of flicker stimulation at varying wavelengths and flicker frequencies, and 7 seconds of post-stimulus recording.

All data processing was conducted using custom MATLAB-based algorithms. The raw data was first processed to generate dispersion-compensated intensity- and phase-based cross-sectional images of the human retina [52]. After crude alignment for bulk

motion correction [142], blood vessel cross-sections visible throughout data acquisition in the unwrapped circular B-scans were individually cropped and aligned. Phase-based Doppler shift information from these cross-sections was used to quantify retinal blood flow. This data was then filtered to remove high-frequency variations arising from the speckle pattern of OCT and artifacts due to human heartbeat. The first two seconds of recording were used as the baseline, and retinal blood flow changes were calculated as follows:

$$RBF\ Change(\%) = \left(\frac{Absolute\ value\,(A) - Baseline\ value\,(B)}{Baseline\ value\,(B)} \right) \times 100 \tag{5.1}$$

The RBF response was characterized separately for arteries and veins using the peak magnitude and the latency (response time) from the onset of flicker stimulation as described previously. To compare the trends shown by arteries and veins, an unpaired t-test was used to analyze vessel responses for individual stimulus intensities. The unpaired t-test was selected because the arterial and venous response was considered independently for this analysis since they represent distinct physiological pathways. Responses showing a statistically significant trend ($p < 0.05$) were marked on the figures with an asterisk.

5.2.3 Stimulation

The ERG system was used to control some of the stimulus parameters, such as frequency, duration, timing, pattern, and intensity. A wheel with four LEDs (white (430 nm - 680 nm), red (640 nm), green (530 nm), and blue (440 nm)) mounted on the visual stimulator integrated with the OCT imaging probe was connected to the ERG system to allow for color selection of the visual stimulus. The OCT and ERG data acquisition was synchronized.

Each ERG and OCT recording consisted of 2 seconds of dark recording (baseline), followed by 1 second of flicker stimulation at 10 Hz and 30 Hz, and concluded with 7 seconds of post-stimulation recording to observe the recovery of the blood flow. Two flicker frequencies were used: 10 Hz and 30 Hz, in order to separate the responses from retinal cones and rods by suppressing the rod response to visual stimulation at 30 Hz. This step in the protocol was required as the spectral response range for rods overlaps with the spectra response ranged for green and red cones. The stimulation protocol was carried out for several intensity levels per subject, with progressively increased stimulation intensities to avoid photoreceptor saturation. Tables 5.1 summarizes the bleaching percentage for different scotopic stimulus intensities and colors [141].

Flicker Stimulus Intensity 430-680 nm ($cd.s/m^2$)	**PR Bleach** (%)	**Flicker Stimulus Intensity 640 nm** ($cd.s/m^2$)	**PR Bleach** (%)	**Flicker Stimulus Intensity 530 nm** ($cd.s/m^2$)	**PR Bleach** (%)	**Flicker Stimulus Intensity 440 nm** ($cd.s/m^2$)	**PR Bleach** (%)
0.78	7.7	2.52	12.1	1.94	16.4	0.04	0.4
1.7	15.8	4.83	22	3.92	30.4	0.06	0.6
2.52	22.8	7	30.2	5.9	42.0	0.08	0.8
3.43	29.7	8.83	36.5	7.94	52	0.14	1.4
4.27	35.5	10.88	42.8	9.95	60.1	0.18	1.9
5.16	41.2	12.61	47.7	11.92	66.8	0.26	2.6
6.02	46.1	14.14	51.6			0.38	2.8
6.92	50.9	15.51	54.9				
7.74	54.9						

Table 5.1: Bleaching percentage for different stimulus intensities for different colors of stimulation.

5.2.4 Subjects

This study has received full ethics clearance from the University of Waterloo Office of Research Ethics and informed consent was obtained from all participants. The study was conducted on three subjects (one male, two females; age 25 ± 5 years) with near-perfect vision (up to -1 Diopters correction). Eye exams were conducted for all the subjects and only subjects with no ocular diseases or a history of epilepsy were included in this study. One drop of Tropicamide was administered to each of the eyes for pupil dilation, followed by $\sim$ 30 minutes of dark adaptation. A chin and headrest frame was used to align the imaged eye (left eye) with respect to the OCT imaging probe. A red LED was used as a fixation target on the contralateral eye. Each imaging session lasted about 2 hours, with about 2 minute break between consecutive recordings to allow for recovery of the retina after visual stimulation. Longer breaks of about 10 minutes were given to allow for switching the wavelength or the flicker frequency of stimulation.

5.3 Results

The RBF response for each of the blood vessels visible in the cross-sectional OCT scans was measured and characterized in terms of amplitude and latency. Arteries and veins were

differentiated based on fundus photography and phase-based analysis of OCT images, as described previously in section 4.3.1. Figure 5.1 summarizes the response of retinal arteries, veins, and the averaged vessel response during 1 second of white-light flicker stimulation at frequencies of 10 Hz and 30 Hz. The use of 30 Hz flicker stimulation was intended to saturate the rods, ensuring that the response originates primarily from cones. Figures 5.2, 5.3, and 5.4 illustrate the responses of retinal vessels to 1-second flicker stimulation using red, green, and blue lights, respectively. In these figures, red plots depict the behavior of arteries, while green plots represent veins. The black curves in Figures 5.1-5.4 A and 5.1-5.4D represent the baseline response of a blood vessel in the absence of flicker stimulation. The colored rectangles in these figures mark the color, timing, and duration of the flicker stimuli.

5.3.1 Differential RBF responses in Arteries and Veins to White-Light Flicker Stimulation at 10 Hz and 30 Hz

Figure 5.1 shows the RBF changes in response to 10 Hz (Figure 5.1A-5.1C) and 30 Hz (Figure 5.1D-5.1F) of white-light flicker stimulation. Figure 5.1A shows the response from two individual blood vessels, an artery (red curve) and a vein (green curve), to 10 Hz flicker stimulation at $5.162 cd.s/m^2$ illumination level. The artery shows an approximate peak RBF change of 120%, with and peak latency of $\sim$ 1.2 seconds. A secondary peak at 40% RBF change is observed approximately 5 seconds after the stimulus onset, possibly due to the strong pulsatile nature of RBF measured from arteries that could not be filtered out completely by the custom algorithms without changing the main peak amplitude and latency. In contrast, the vein exhibits a more substantial RBF increase of 250% at a latency of 1.2 seconds. The black curve represents the baseline response of the same vein during dark recordings (no visual stimulation), with typical RBF variations of up to 25%. The gray rectangle corresponds to the timing of white-light flicker stimulation.

Figures 5.1B and 5.1E show the dependence of the peak RBF amplitude on the stimulus intensity for 10 Hz and 30 Hz white-light flicker stimulation respectively. In the case of 10 Hz stimulation, RBF changes measured from arteries (red curves) increase almost linearly with the stimulus intensity up to $\sim 3.5 cd.s/m^2$, then decrease almost linearly with further increase of the stimulus intensity. RBF changes measured from veins (green curves) show a non-linear increase with an increase of the stimulus intensity. The RBF changes measured from the two types of blood vessels for the highest setting of the stimulus are statistically significantly different (marked with asterisk in Figure 5.1B). The black curve in Figure 5.1B represents the behavior of the total RBF (sum of arterial and venal flow for all blood vessels

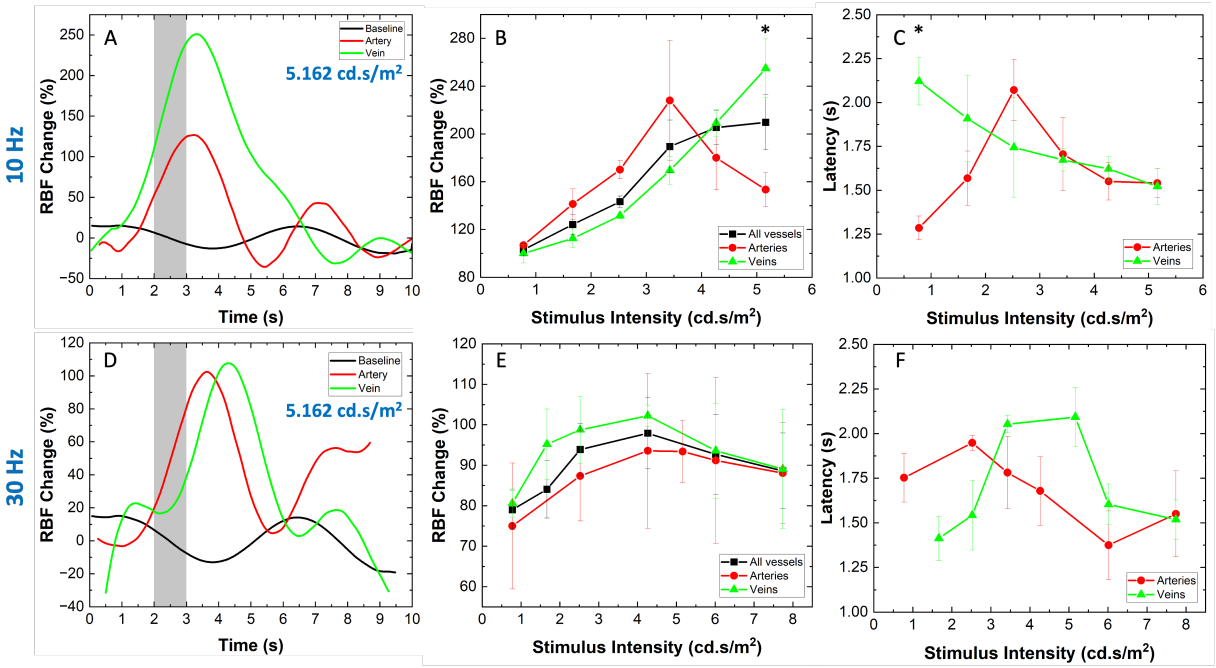


Figure 5.1: (A) RBF response measured from an artery (red) and a vein (green) in response to 10 Hz of white-light flicker stimulation. The black curve corresponds to RBF changes measured during dark recordings (no stimulus). RBF peak amplitude (B) as a function of the stimulus intensity for arteries (red), veins (green), and the total retinal blood flow (black) and latency (C) as a function of the stimulus intensity in response to 10 Hz white-light flicker stimulation. (D) RBF response measured from an artery (red) and a vein (green) in response to 30 Hz of white-light flicker stimulation. RBF peak amplitude (E) to varying stimulus intensities for arteries (red), veins (green), and the total retinal blood flow (black). (F) Latency response of arteries (red) and veins (green) to varying stimulus intensities. The error bars represent the Standard Error of the mean values. Statistically significant differences in the arterial and venous RBF responses are marked with an asterisk in Figures 5.1B and 5.1C.

visible on the circular OCT B-scans) in response to the increasing intensity of the visual stimulus. The total RBF change appears to plateau for stimulus intensities $> 4cd.s/m^2$. In contrast, RBF changes measured in retinal vessels in response to 30 Hz flicker stimulation show very similar behavior for the arteries and veins (Figure 5.1E).

Figures 5.1C and 5.1F show the peak RBF latency as a function of the stimulus intensity in response to 10 Hz and 30 Hz of white-light flicker stimulation respectively. In the case of 10 Hz flicker stimulation, arteries exhibit an initial increase in RBF peak latency, followed by an almost linear decrease with the stimulus intensity increase and the peak response occurs for $\sim 2.5cd.s/m^2$. In contrast, the peak RBF latency measured in veins shows a continuous, non-linear decrease. Note that the RBF peak latencies measured from arteries and veins with the weakest stimulus intensity are statistically significant (marked with an asterisk in Figure 5.1C). While for 30 Hz stimulus (Figure 5.1F), the RBF peak latency measured in arteries and veins shows some variation with the increase of the stimulus intensity, those variations do not appear to be statistically significant.

5.3.2 Differential RBF Responses in Arteries and Veins to Red-Light Flicker Stimulation at 10 Hz and 30 Hz

Figure 5.2 shows the retinal blood flow changes in response to 1 second of red-light flicker stimulation at 10 Hz (Figures 5.2A-5.2C) and 30 Hz (Figures 5.2D-5.2F). Figure 5.2A presents the RBF response of an artery and a vein during 10 Hz red-light flicker stimulation at $12.612cd.s/m^2$. Both the artery (red curve) and the vein (green curve) exhibit a sharp increase in RBF at the onset of stimulation, with the artery reaching a maximum change of $\sim$ 150% with a latency of around 2 seconds and the vein reaching a slightly smaller amplitude of roughly 120% with a latency of about 1.5 seconds. The baseline response (dark recording), depicted by the black curve, shows fluctuations in the RBF change of up to 25%. Figure 5.2D shows the response of the RBF measured from an artery and a vein to 30 Hz red-light flicker stimulation. The RBF change measured from the artery (red curve) peaks at $\sim$ 75% RBF change, while the one from the vein peaks at $\sim$ 60% which in both cases is about 50% smaller than the response of the RBF from these vessels for 10 Hz flicker stimulation.

Figures 5.2B and 5.2E show the dependence of the peak RBF amplitude on the stimulus intensity for 10 Hz and 30 Hz white-light flicker stimulation respectively. In the case of 10 Hz stimulation (Figure 5.2B), RBF changes measured from arteries (red curves) and veins (green curves) both show a non-linear increase with an increase of the stimulus intensity that develop in parallel. In contrast, RBF changes measured in retinal vessels in response

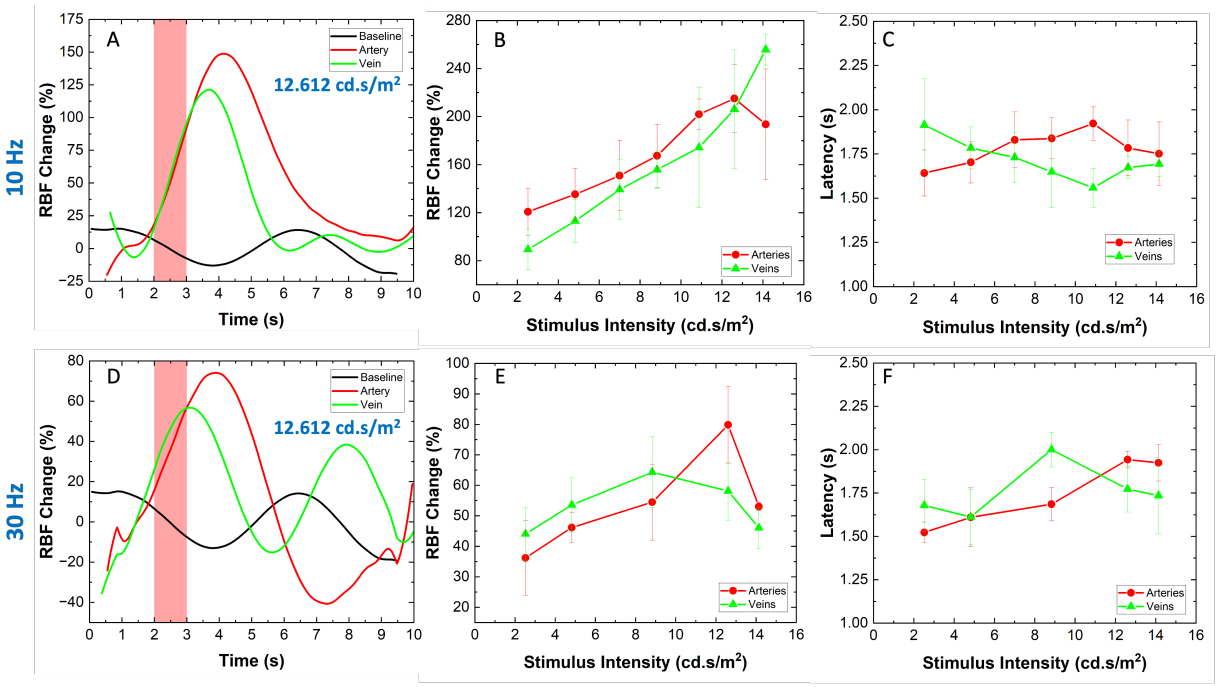


Figure 5.2: (A) RBF response measured from an artery (red) and a vein (green) in response to 10 Hz of red-light flicker stimulation. The black curve corresponds to RBF changes measured during dark recordings (no stimulus). RBF peak amplitude (B) and latency (C) as functions of the stimulus intensity to varying stimulus intensities. (D) RBF response measured from an artery (red) and a vein (green) in response to 30 Hz of white-light flicker stimulation. RBF peak amplitude (E) and latency (F) to varying stimulus intensities. The error bars represent the Standard Error of the mean values.

to 30 Hz flicker stimulation (Figure 5.2E) show a non-linear increase of the RBF peak amplitude in arteries and a non-linear decrease in veins for stimulus intensity higher than $\sim 9cd.s/m^2$.

Figures 5.2C and 5.2F show the peak RBF latency as a function of the stimulus intensity in response to 10 Hz and 30 Hz of white-light flicker stimulation respectively. In the case of 10 Hz flicker stimulus, arteries exhibit an initial increase in RBF peak latency, followed by an almost linear decrease with the stimulus intensity increase and the peak response occurs for $\sim 2.5cd.s/m^2$. In both cases, the RBF peak latency measured in arteries and veins shows some variation with the increase of the stimulus intensity, however, those variations do not appear to be statistically significant.

5.3.3 Differential RBF Responses in Arteries and Veins to Green-Light Flicker Stimulation at 10 Hz and 30 Hz

Figure 5.3 shows the retinal blood flow changes in response to 10 Hz (Figures 5.3A-5.3C) and 30 Hz (Figures 5.3D-5.3F) of green-light flicker stimulation. Figures 5.3A and 5.3D show the RBF response of an artery and a vein to 10 Hz and 30 Hz green-light flicker stimulation at $9.945cd.s/m^2$, respectively. All vessels show a steep increase in RBF at the onset of flicker stimulation, with the venous response slightly higher than the arterial response for both frequencies. The secondary peaks observed in these responses can be attributed to the pulsatile nature of the vessels. Baseline fluctuations, shown by the black curve, reach up to $\sim 25\%$ and the green rectangle indicates the color and the timing of flicker stimulation.

Figures 5.3B and 5.3E show the dependence of the peak RBF amplitude on the stimulus intensity for 10 Hz and 30 Hz green-light flicker stimulation respectively. In both cases, the RBF peak magnitude in both types of vessels increases somewhat with the increase of the stimulus intensity. The response is more pronounced for 10 Hz compared to the 30 Hz flicker frequency.

Figures 5.3C and 5.3F show the peak RBF latency as a function of the stimulus intensity in response to 10 Hz and 30 Hz of white-light flicker stimulation respectively. In general, the RBF peak latency exhibits a slight decrease with the increase of the stimulus intensity for both types of retinal vessels and the two flicker frequencies. One exception is the arterial RBF peal latency measured for 10 Hz flicker and $6cd.s/m^2$ stimulus intensity. Given the small number of study participants, it is unlikely that this deviation is statistically significant.

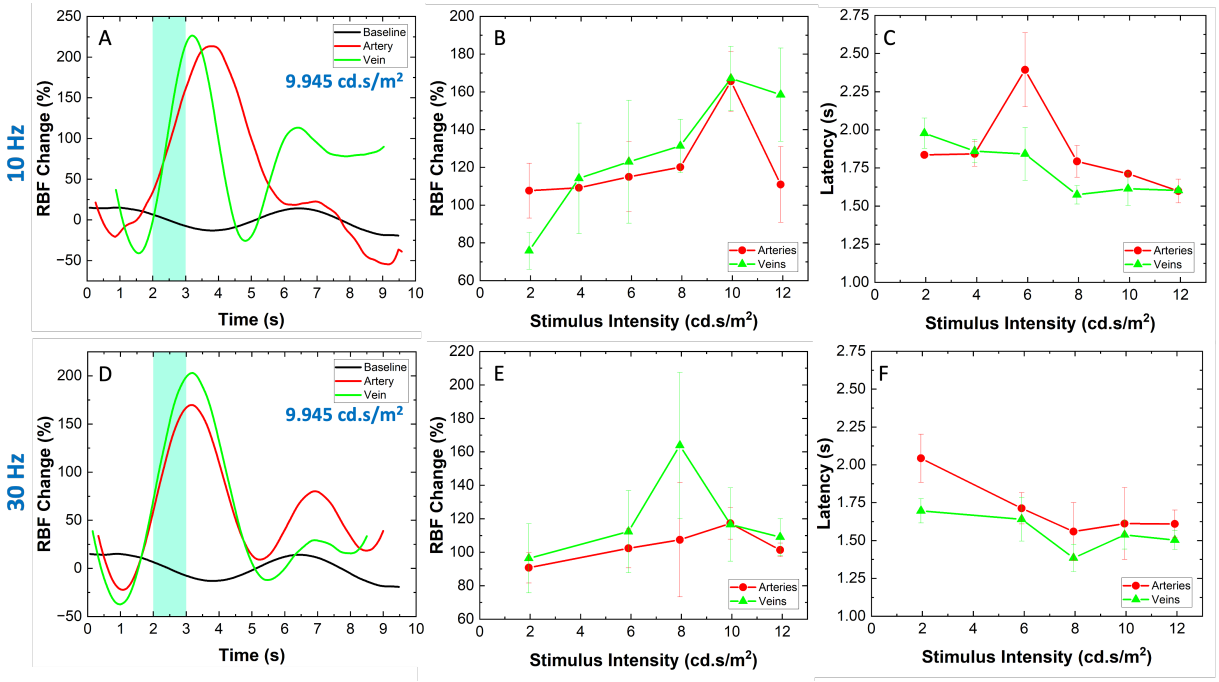


Figure 5.3: (A) RBF response measured from an artery (red) and a vein (green) in response to 10 Hz of green-light flicker stimulation. The black curve corresponds to RBF changes measured during dark recordings (no stimulus). RBF peak amplitude (B) and latency (C) as functions of the stimulus intensity to varying stimulus intensities. (D) RBF response measured from an artery (red) and a vein (green) in response to 30 Hz of white-light flicker stimulation. RBF peak amplitude (E) and latency (F) to varying stimulus intensities. The error bars represent the Standard Error of the mean values.

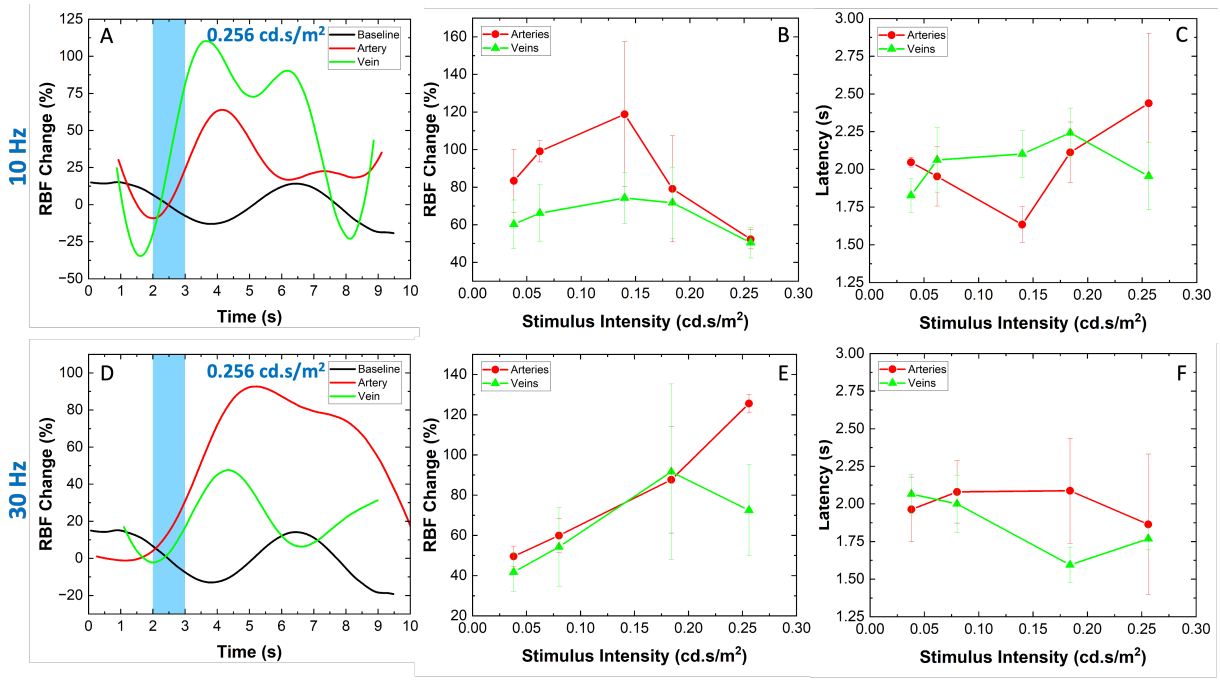


Figure 5.4: (A) RBF response measured from an artery (red) and a vein (green) in response to 10 Hz of blue-light flicker stimulation. The black curve corresponds to RBF changes measured during dark recordings (no stimulus). RBF peak amplitude (B) and latency (C) as functions of the stimulus intensity to varying stimulus intensities. (D) RBF response measured from an artery (red) and a vein (green) in response to 30 Hz of white-light flicker stimulation. RBF peak amplitude (E) and latency (F) to varying stimulus intensities. The error bars represent the Standard Error of the mean values.

5.3.4 Differential RBF Responses in Arteries and Veins to Blue-Light Flicker Stimulation at 10 Hz and 30 Hz

Figure 5.4 shows the RBF changes in response to 10 Hz (Figures 5.4A-5.4C) and 30 Hz (Figures 5.4D-5.4F) of blue-light flicker stimulation. Figures 5.4A and 5.4D represent the response of an artery and a vein to 10 Hz and 30 Hz blue-light flicker stimulation at $0.256 cd.s/m^2$, respectively. The artery (red curve) shows a peak RBF change of $\sim 60\%$ for 10 Hz and about 1.5 times higher for 30 Hz. Vein shows a higher response for 10 Hz compared to 30 Hz flicker frequency. The latency for all responses is about 2 seconds.

Figure 5.4B shows the RBF changes with 10 Hz blue-light flicker stimulation across

vessels. Both arteries and veins do not show a significant change in RBF amplitude with increasing stimulus intensity. At lower stimulus intensities, arteries demonstrate a more pronounced change in RBF compared to veins; however, this response decreases significantly with the increase in the stimulus intensity. In contrast, veins show a more modest change in RBF peak magnitude with a non-linear response that appears to peak for stimulus intensity of $\sim 0.14 cd.s/m^2$.

Figures 5.4C and 5.4F show the RBF latency with 10 Hz and 30 Hz blue-light flicker stimulation respectively. While in both cases both arteries and veins show some changes in the RBF peak latency, those changes are not statistically significant.

Figure 5.4E shows the RBF changes with 30 Hz blue-light flicker stimulation in retinal blood vessels. Both arteries and veins show almost linear changes in RBF peak amplitude with increasing stimulus intensity that develop in parallel, up to stimulus intensity of $\sim 0.19 cd.s/m^2$. For higher stimulus intensities, the arterial and venous responses diverge with RBF peak magnitude increasing in arteries and decreasing in veins.

5.4 Discussion

Results from this study demonstrate a differential increase in RBF around the ONH in response to varying wavelengths and frequencies of flicker stimulation in healthy human subjects. These findings align with past studies. For instance, Hanaguri *et. al.* reported a peak RBF change of 40.9% in mice at 12 Hz of flicker stimulation, compared to 24.0% and 25.9% at 8 Hz and 16 Hz flicker frequencies, respectively [164]. Similarly, Polak *et. al.* found that arteries showed a significantly reduced vasodilation in response to 64 Hz flicker stimulation [47]. Additionally, Falsini *et. al.* reported attenuation in RBF change beyond 9 Hz of flicker frequency and noted saturation in RBF changes with increased luminance of flicker stimulus [165]. Similarly, Riva *et. al.* reported that chromatic and luminance modulations are potentially related to the parvocellular and magnocellular pathways, respectively [163]. In cats, Van *et. al.* observed peak RBF change between 5 Hz and 20 Hz flicker frequencies with diminished response at higher frequencies [166].

While previous studies focused on RBF responses from single wavelengths and fixed frequencies, this study expands on these findings by characterizing the response of RBF to different wavelengths and flicker frequencies using a short-duration stimulus, making it more feasible for clinical adaptability. The use of 30 Hz stimulus effectively saturates the rod response [167], allowing for the RBF changes predominantly arising from cone stimulation to be isolated. Although there is some overlap in the spectral sensitivity of

different cone types, the overall response to a specific color stimulus provides a reasonable estimate of the contributions from the corresponding cone population.

RBF changes observed using blue-light stimulation were lower at both 10 Hz and 30 Hz, likely due to the limiting number of S-cones [168, 169]. Additionally, average RBF changes were more pronounced with 10 Hz flicker stimulation compared to 30 Hz, possibly due to rod saturation at the higher frequency [170]. This study's findings align with Riva *et. al.*, who reported greater RBF responses with single-wavelength (G and R) luminance compared to mixed wavelengths ($G + R$) [163]. Although technical limitations prevent direct comparisons, the similar peak responses at 10 Hz with white-light and red-light stimulation provide partial support for these observations.

Responses to S-cone stimulation seem to indicate a slow recovery after stimulation when compared with white or L/M targeting stimuli, suggesting a similarity between S-cones and rods in response patterns, while M- and L-cones show distinct dynamics [171, 172]. These differential responses could serve as potential biomarkers for retinal diseases that disproportionately affect certain photoreceptors, such as the S-cones in AMD.

Overall, 30 Hz stimulation elicited faster yet smaller changes in RBF compared to 10 Hz, likely due to the faster delivery of stimuli that induces a higher metabolic demand over a shorter time span [173]. The response at 30 Hz is primarily cone-driven that have faster recovery rate as compared to rods [174], which could explain the faster response for 30 Hz stimulation. The smaller magnitude of RBF changes can also be explained by rod saturation at higher frequencies, resulting in the stimulation of a smaller number of photoreceptors overall. White-light stimulation, by stimulating all cone types, results in a cumulative response that reflects the combined effects of monochromatic stimulation.

It is important to note that although the arteries and the veins show slightly different mean responses, the difference is not significant in most cases. The observed variations could arise from the difference in the vessel wall structure between arteries and veins. In general, arteries have more muscular walls, while veins are more elastic and capable of expanding and holding larger volumes of blood. Besides, the range of the RBF change and latencies for each type of blood vessel varies, depending on additional factors like the area being served by the blood vessel, which has not been explored in this study but poses an important question for future direction. Besides frequency and intensity, the pattern, region, and modulation depth of flicker stimulation also play a crucial role in RBF responses. Studies by Zhong *et. al.* [41] and Tan *et. al.* [67] demonstrated that smaller stimulation areas and patterns of stimulation (e.g., single flash versus flicker) influence RBF dynamics significantly. Van *et. al.* demonstrated in cats that higher modulation depth leads to increased RBF response [166]. These parameters were not explored in the

current study but are essential considerations for future work.

The presence of secondary peaks in RBF responses likely reflects the pulsatile nature of blood flow. The elastic properties of vessel walls also contribute, as they resist rapid changes in flow. Regional metabolic demands could result in delayed secondary peaks, indicating that RBF does not immediately return to baseline after stimulation. This is supported by the study conducted by Wang *et. al.* [65], who reported an increase of $\sim 22\%$ in RBF observed $10-15$ seconds after 30 seconds of flicker stimulation. Moreover, a secondary increase in RBF was also observed in rat retina by Tan *et. al.* [67].

Several limitations need to be considered for this study. First, while it is possible to distinguish the rod versus the cone response using the different frequencies of flicker stimulation, it is quite challenging to isolate individual cone-type responses due to their overlapping wavelength sensitivities. As a result, a wavelength targeted to stimulate one type of cone cells also triggers a response from a small percentage of the other type of cone cells. This is especially important to consider when using 10 Hz flicker frequency as rods contribute to RBF changes at this frequency. Additionally, variations in cone distribution among individuals- related to age, sex, ethnicity, and other factors- affect RBF responses and limit direct comparisons across wavelengths. The lack of active pupil tracking to account for eye motion artifacts introduces additional computational demands during post-processing, which may hinder clinical application.

5.5 Conclusions

In summary, a D-OCT system has been used to investigate the contributions of different photoreceptor types to retinal blood flow changes in response to flicker stimulation. Findings from this study show that flicker stimulation significantly increases RBF in healthy subjects, with distinct responses based on vessel type and stimulus characteristics. This work suggests the potential of RBF measurements as a diagnostic tool for retinal health and paves the way for further studies on neurovascular coupling and photoreceptor-specific responses.

Chapter 6

Conclusions

This dissertation investigated retinal blood flow changes and neuronal responses associated with visual stimulation of retina. The results from these studies extend our understanding of neurovascular coupling in healthy human retina, offering valuable insights into the mechanisms of blood flow regulations in the eye.

6.1 Summary and contributions

The main contributions of this PhD dissertation are:

- **Development of the OCT+ERG technology and image processing algorithms:** This thesis research resulted in a novel combined OCT+ERG technology capable of detecting intensity and phase variations linked to local electric field and optical path length changes across retinal layers. The system is also capable of measuring retinal blood flow and blood vessel diameter changes caused by visual stimulus, while simultaneously recording the electrical activity of the neurons as the 'gold standard' via ERG. Since the OCT system is compact and fiberoptic and the ERG system is a commercial clinical device, the combined OCT+ERG instrument, along with the image acquisition protocols and image processing algorithms can be easily adapted for clinical studies, offering a new tool for investigating retinal neuronal diseases such as Glaucoma, Age-related Macular Degeneration, and Diabetic Retinopathy.
- **Neurovascular Coupling Mechanisms:** Results from the single-flash stimulation experiments indicate that visual stimulation triggers a response from the retinal

visual pathway that includes photoreceptors, bipolar cells, and retinal ganglion cells. This neuronal activation generates an ion flux, altering local electric fields in the cell membranes, osmotic changes as well as conformational changes in the rhodopsin molecules. All of these processes can lead to local changes in the refractive index of the retinal tissue and correspondingly change how light is scattered from the retinal tissue, therefore resulting in intrinsic optical signals that are measurable with OCT. In this study, ERG recordings were used in parallel with the OCT-based ORG recordings to validate the ORG responses from different retinal layers.

- **Insights on the stimulus-dependent neurovascular responses:** Results from our studies revealed that retinal arteries and veins respond differently to visual stimulation and that transient RBF response is dependent on both the color and intensity of the visual stimulus. Furthermore, our study showed that visual stimulation causes initial vasoconstriction of retinal arteries and vasodilation in retinal veins with the two processes causing anisotropic changes to the lateral and axial diameter of the retinal blood vessels.

6.2 Future Work

The OCT+ERG technology and studies presented in this PhD study leave plenty of room for future technological and experimental advancements, as well as pose questions that can become the center point of future studies:

- **Expanded stimulus parameter exploration:** The current studies on neurovascular coupling explored a limited number of stimulus parameters. Future experiments can examine additional stimulus parameters, such as varied flicker stimulus timing, a broader range of frequencies, complex patterns of flicker stimulus, modulation, and duty cycles, to deepen our understanding of neurovascular coupling.
- **Establishing normative data:** Developing baseline values for retinal blood flow changes in the healthy retina is essential for comparing responses in diseased states, providing a foundation for studies on conditions such as glaucoma.
- **Application in clinical and research settings:** This thesis lays the groundwork for extensive studies in both healthy and diseased subjects. Minor adjustments to the image processing algorithms could enable clinical adaptation, facilitating early diagnosis and monitoring of retinal diseases.

References

[1] Göran Darius Hildebrand and Alistair R Fielder. Anatomy and physiology of the retina. *Pediatric retina*, pages 39–65, 2011.

[2] Vilayanur S Ramachandran. *Encyclopedia of the human brain*. Elsevier, 2002.

[3] Anat London, Inbal Benhar, and Michal Schwartz. The retina as a window to the brain—from eye research to cns disorders. *Nature Reviews Neurology*, 9(1):44–53, 2013.

[4] Alon Harris, Thomas A Ciulla, Hak Sung Chung, and Bruce Martin. Regulation of retinal and optic nerve blood flow. *Archives of ophthalmology*, 116(11):1491–1495, 1998.

[5] Jan M Provis. Development of the primate retinal vasculature. *Progress in retinal and eye research*, 20(6):799–821, 2001.

[6] Marcus Fruttiger. Development of the retinal vasculature. *Angiogenesis*, 10:77–88, 2007.

[7] Joanna Kur, Eric A Newman, and Tailoi Chan-Ling. Cellular and physiological mechanisms underlying blood flow regulation in the retina and choroid in health and disease. *Progress in retinal and eye research*, 31(5):377–406, 2012.

[8] JP Campbell, M Zhang, TS Hwang, ST Bailey, DJ Wilson, Y Jia, and D Huang. Detailed vascular anatomy of the human retina by projection-resolved optical coherence tomography angiography. *Scientific reports*, 7(1):1–11, 2017.

[9] Charles Smart Roy and Charles S Sherrington. On the regulation of the blood-supply of the brain. *The Journal of physiology*, 11(1-2):85, 1890.

[10] David Attwell, Alastair M Buchan, Serge Charpak, Martin Lauritzen, Brian A MacVicar, and Eric A Newman. Glial and neuronal control of brain blood flow. *Nature*, 468(7321):232–243, 2010.

[11] CE Riva, JE Grunwald, and BL Petrig. Autoregulation of human retinal blood flow. an investigation with laser doppler velocimetry. *Investigative ophthalmology & visual science*, 27(12):1706–1712, 1986.

[12] Charles E Riva, Eric Logean, and Benedetto Falsini. Visually evoked hemodynamical response and assessment of neurovascular coupling in the optic nerve and retina. *Progress in retinal and eye research*, 24(2):183–215, 2005.

[13] Mitsuhiro Kondo, Lin Wang, and Anders Bill. The role of nitric oxide in hyperaemic response to flicker in the retina and optic nerve in cats. *Acta Ophthalmologica Scandinavica*, 75(3):232–235, 1997.

[14] Youngseok Song, Taiji Nagaoka, Takafumi Yoshioka, Seigo Nakabayashi, Tomofumi Tani, and Akitoshi Yoshida. Role of glial cells in regulating retinal blood flow during flicker-induced hyperemia in cats. *Investigative Ophthalmology & Visual Science*, 56(12):7551–7559, 2015.

[15] Mozhgan Sharifizad, Katarzyna J Witkowska, Gerold C Aschinger, Sabina Sapeta, Alexandra Rauch, Doreen Schmidl, Rene M Werkmeister, Gerhard Garhöfer, and Leopold Schmetterer. Factors determining flicker-induced retinal vasodilation in healthy subjects. *Investigative Ophthalmology & Visual Science*, 57(7):3306–3312, 2016.

[16] Dries Hendrikx, Anne Smits, Mario Lavanga, Ofelie De Wel, Liesbeth Thewissen, Katrien Jansen, Alexander Caicedo, Sabine Van Huffel, and Gunnar Naulaers. Measurement of neurovascular coupling in neonates. *Frontiers in physiology*, 10:65, 2019.

[17] Ameer A Haider, Tonia S Rex, and Lauren K Wareham. cgmp signaling in the neurovascular unit—implications for retinal ganglion cell survival in glaucoma. *Biomolecules*, 12(11):1671, 2022.

[18] Constantin J Pournaras, Elisabeth Rungger-Brändle, Charles E Riva, Sveinn H Hardarson, and Einar Stefansson. Regulation of retinal blood flow in health and disease. *Progress in retinal and eye research*, 27(3):284–330, 2008.

[19] Jonathan E Noonan, Ecosse L Lamoureux, and Marc Sarossy. Neuronal activity-dependent regulation of retinal blood flow. *Clinical & experimental ophthalmology*, 43(7):673–682, 2015.

[20] G Garhöfer, C Zawinka, H Resch, KH Huemer, L Schmetterer, and GT Dorner. Response of retinal vessel diameters to flicker stimulation in patients with early open angle glaucoma. *Journal of glaucoma*, 13(4):340–344, 2004.

[21] A Popa Cherecheanu, G Garhofer, D Schmidl, R Werkmeister, and L Schmetterer. Ocular perfusion pressure and ocular blood flow in glaucoma. *Current opinion in pharmacology*, 13(1):36–42, 2013.

[22] Lauren K Wareham and David J Calkins. The neurovascular unit in glaucomatous neurodegeneration. *Frontiers in Cell and Developmental Biology*, 8:452, 2020.

[23] Berthold Pemp and Leopold Schmetterer. Ocular blood flow in diabetes and age-related macular degeneration. *Canadian journal of ophthalmology*, 43(3):295–301, 2008.

[24] Rita Ehrlich, Nisha S Kheradiya, Diana M Winston, Daniel B Moore, Barbara Wirostko, and Alon Harris. Age-related ocular vascular changes. *Graefe's Archive for Clinical and Experimental Ophthalmology*, 247:583–591, 2009.

[25] John G Flannery, DB Farber, Alan C Bird, and Dean Bok. Degenerative changes in a retina affected with autosomal dominant retinitis pigmentosa. *Investigative ophthalmology & visual science*, 30(2):191–211, 1989.

[26] Christian Hamel. Retinitis pigmentosa. *Orphanet journal of rare diseases*, 1:1–12, 2006.

[27] Gerhard Garhöfer, Jacqueline Chua, Bingyao Tan, Damon Wong, Doreen Schmidl, and Leopold Schmetterer. Retinal neurovascular coupling in diabetes. *Journal of Clinical Medicine*, 9(9):2829, 2020.

[28] Ayoub Lassoued, Furu Zhang, Kazuhiro Kurokawa, Yan Liu, Marcel T Bernucci, James A Crowell, and Donald T Miller. Cone photoreceptor dysfunction in retinitis pigmentosa revealed by optoretinography. *Proceedings of the National Academy of Sciences*, 118(47):e2107444118, 2021.

[29] Robert Cooper and Mina Gaffney. Intensity-based optoretinography reveals subclinical deficits in cone function in retinitis pigmentosa. *Frontiers in Ophthalmology*, 4:1373549, 2024.

[30] L Schmetterer and M Wolzt. Ocular blood flow and associated functional deviations in diabetic retinopathy. *Diabetologia*, 42(4):387, 1999.

[31] Yoshitaka Ueno, Takeshi Iwase, Kensuke Goto, Ryo Tomita, Eimei Ra, Kentaro Yamamoto, and Hiroko Terasaki. Association of changes of retinal vessels diameter with ocular blood flow in eyes with diabetic retinopathy. *Scientific Reports*, 11(1):4653, 2021.

[32] Shen Nian, Amy CY Lo, Yajing Mi, Kai Ren, and Di Yang. Neurovascular unit in diabetic retinopathy: pathophysiological roles and potential therapeutical targets. *Eye and Vision*, 8(1):15, 2021.

[33] Martin J Dumskyj, Stephen J Aldington, Caroline J Doré, and Eva M Kohner. The accurate assessment of changes in retinal vessel diameter using multiple frame electrocardiograph synchronised fundus photography. *Current eye research*, 15(6):625–632, 1996.

[34] Lars Pedersen, Michael Grunkin, Bjarne Ersbøll, Kaj Madsen, Michael Larsen, Nynne Christoffersen, and Ulrik Skands. Quantitative measurement of changes in retinal vessel diameter in ocular fundus images. *Pattern Recognition Letters*, 21(13-14):1215–1223, 2000.

[35] CE Riva, S Harino, BL Petrig, and RD Shonat. Laser doppler flowmetry in the optic nerve. *Experimental eye research*, 55(3):499–506, 1992.

[36] G Michelson, B Schmauss, MJ Langhans, J Harazny, and MJM Groh. Principle, validity, and reliability of scanning laser doppler flowmetry, 1996.

[37] Charles Riva, Benjamin Ross, and George B Benedek. Laser doppler measurements of blood flow in capillary tubes and retinal arteries. *Investigative Ophthalmology & Visual Science*, 11(11):936–944, 1972.

[38] Charles E Riva, Gilbert T Feke, Bruno Eberli, and Vili Benary. Bidirectional ldv system for absolute measurement of blood speed in retinal vessels. *Applied Optics*, 18(13):2301–2306, 1979.

[39] Charles E Riva, Juan E Grunwald, Stephen H Sinclair, and BL Petrig. Blood velocity and volumetric flow rate in human retinal vessels. *Investigative ophthalmology & visual science*, 26(8):1124–1132, 1985.

[40] Sebastian Wolf, Oliver Arend, and Martin Reim. Measurement of retinal hemodynamics with scanning laser ophthalmoscopy: reference values and variation. *Survey of ophthalmology*, 38:S95–S100, 1994.

[41] Zhangyi Zhong, Benno L Petrig, Xiaofeng Qi, and Stephen A Burns. In vivo measurement of erythrocyte velocity and retinal blood flow using adaptive optics scanning laser ophthalmoscopy. *Optics express*, 16(17):12746–12756, 2008.

[42] Harold R Novotny and David L Alvis. A method of photographing fluorescence in circulating blood in the human retina. *Circulation*, 24(1):82–86, 1961.

[43] PR Preussner, G Richard, O Darrelmann, J Weber, and I Kreissig. Quantitative measurement of retinal blood flow in human beings by application of digital image-processing methods to television fluorescein angiograms. *Graefe's archive for clinical and experimental ophthalmology*, 221:110–112, 1983.

[44] T Guran, Ran C Zeimer, Mahnaz Shahidi, and Marek T Mori. Quantitative analysis of retinal hemodynamics using targeted dye delivery. *Investigative ophthalmology & visual science*, 31(11):2300–2306, 1990.

[45] C Prünte and P Niesel. Quantification of choroidal blood-flow parameters using indocyanine green video-fluorescence angiography and statistical picture analysis. *Graefe's archive for clinical and experimental ophthalmology*, 226:55–58, 1988.

[46] Naoko Matsuda, Yuichiro Ogura, Hirokazu Nishiwaki, Kazuaki Miyamoto, Takashi Matsubara, Junichi Kiryu, and Yoshihito Honda. Visualization of leukocyte dynamics in the choroid with indocyanine green. *Investigative ophthalmology & visual science*, 37(11):2228–2233, 1996.

[47] Kaija Polak, Leopold Schmetterer, and Charles E Riva. Influence of flicker frequency on flicker-induced changes of retinal vessel diameter. *Investigative ophthalmology & visual science*, 43(8):2721–2726, 2002.

[48] Nishtha Panwar, Philemon Huang, Jiaying Lee, Pearse A Keane, Tjin Swee Chuan, Ashutosh Richhariya, Stephen Teoh, Tock Han Lim, and Rupesh Agrawal. Fundus photography in the 21st century—a review of recent technological advances and their implications for worldwide healthcare. *Telemedicine and e-Health*, 22(3):198–208, 2016.

[49] Lawrence A Yannuzzi, Kathleen T Rohrer, Lori J Tindel, Russell S Sobel, Marcelle A Costanza, William Shields, and Edith Zang. Fluorescein angiography complication survey. *Ophthalmology*, 93(5):611–617, 1986.

[50] Monique Hope-Ross, Lawrence A Yannuzzi, Evangelos S Gragoudas, David R Guyer, Jason S Slakter, John A Sorenson, Sara Krupsky, Dennis A Orlock, and Carmen A Puliafito. Adverse reactions due to indocyanine green. *Ophthalmology*, 101(3):529–533, 1994.

[51] David Huang, Eric A Swanson, Charles P Lin, Joel S Schuman, William G Stinson, Warren Chang, Michael R Hee, Thomas Flotte, Kenton Gregory, Carmen A Puliafito, et al. Optical coherence tomography. *science*, 254(5035):1178–1181, 1991.

[52] Maciej Wojtkowski, Vivek J Srinivasan, Tony H Ko, James G Fujimoto, Andrzej Kowalczyk, and Jay S Duker. Ultrahigh-resolution, high-speed, fourier domain optical coherence tomography and methods for dispersion compensation. *Optics express*, 12(11):2404–2422, 2004.

[53] Barry Cense, Nader A Nassif, Teresa C Chen, Mark C Pierce, Seok-Hyun Yun, B Hyle Park, Brett E Bouma, Guillermo J Tearney, and Johannes F De Boer. Ultrahigh-resolution high-speed retinal imaging using spectral-domain optical coherence tomography. *Optics express*, 12(11):2435–2447, 2004.

[54] Wolfgang Drexler and James G Fujimoto. *Optical coherence tomography: technology and applications*. Springer Science & Business Media, 2008.

[55] Hongwu Ren, Kjell Morten Brecke, Zhihua Ding, Yonghua Zhao, J Stuart Nelson, and Zhongping Chen. Imaging and quantifying transverse flow velocity with the doppler bandwidth in a phase-resolved functional optical coherence tomography. *Optics letters*, 27(6):409–411, 2002.

[56] Rainer A Leitgeb, L Schmetterer, W Drexler, AF Fercher, RJ Zawadzki, and T Bajraszewski. Real-time assessment of retinal blood flow with ultrafast acquisition by color doppler fourier domain optical coherence tomography. *Optics express*, 11(23):3116–3121, 2003.

[57] Rainer A Leitgeb, Leopold Schmetterer, Christoph K Hitzenberger, Adolf F Fercher, Fatma Berisha, Maciej Wojtkowski, and Tomasz Bajraszewski. Real-time measurement of in vitro flow by fourier-domain color doppler optical coherence tomography. *Optics letters*, 29(2):171–173, 2004.

[58] Joseph A Izatt, Manish D Kulkarni, Siavash Yazdanfar, Jennifer K Barton, and Ashley J Welch. In vivo bidirectional color doppler flow imaging of picoliter blood volumes using optical coherence tomography. *Optics letters*, 22(18):1439–1441, 1997.

[59] Zhongping Chen, Thomas E Milner, Shyam Srinivas, Xiaojun Wang, Arash Malekafzali, Martin JC van Gemert, and J Stuart Nelson. Noninvasive imaging of in vivo blood flow velocity using optical doppler tomography. *Optics letters*, 22(14):1119–1121, 1997.

[60] Brian R White, Mark C Pierce, Nader Nassif, Barry Cense, B Hyle Park, Guillermo J Tearney, Brett E Bouma, Teresa C Chen, and Johannes F De Boer. In vivo dynamic human retinal blood flow imaging using ultra-high-speed spectral domain optical doppler tomography. *Optics express*, 11(25):3490–3497, 2003.

[61] Yimin Wang, Bradley A Bower, Joseph A Izatt, Ou Tan, and David Huang. In vivo total retinal blood flow measurement by fourier domain doppler optical coherence tomography. *Journal of biomedical optics*, 12(4):041215–041215, 2007.

[62] Yimin Wang, Bradley A Bower, Joseph A Izatt, Ou Tan, and David Huang. Retinal blood flow measurement by circumpapillary fourier domain doppler optical coherence tomography. *Journal of biomedical optics*, 13(6):064003–064003, 2008.

[63] Yimin Wang, Amani A Fawzi, Rohit Varma, Alfredo A Sadun, Xinbo Zhang, Ou Tan, Joseph A Izatt, and David Huang. Pilot study of optical coherence tomography measurement of retinal blood flow in retinal and optic nerve diseases. *Investigative ophthalmology & visual science*, 52(2):840–845, 2011.

[64] Veronika Doblhoff-Dier, Leopold Schmetterer, Walthard Vilser, Gerhard Garhöfer, Martin Gröschl, Rainer A Leitgeb, and René M Werkmeister. Measurement of the total retinal blood flow using dual beam fourier-domain doppler optical coherence tomography with orthogonal detection planes. *Biomedical optics express*, 5(2):630–642, 2014.

[65] Yimin Wang, Amani A Fawzi, Ou Tan, Xinbo Zhang, and David Huang. Flicker-induced changes in retinal blood flow assessed by doppler optical coherence tomography. *Biomedical optics express*, 2(7):1852–1860, 2011.

[66] Rainer A Leitgeb, René M Werkmeister, Cedric Blatter, and Leopold Schmetterer. Doppler optical coherence tomography. *Progress in retinal and eye research*, 41:26–43, 2014.

[67] Bingyao Tan, Erik Mason, Benjamin MacLellan, and Kostadinka K Bizheva. Correlation of visually evoked functional and blood flow changes in the rat retina measured with a combined oct+ erg system. *Investigative Ophthalmology & Visual Science*, 58(3):1673–1681, 2017.

[68] Shuichi Makita, Youngjoo Hong, Masahiro Yamanari, Toyohiko Yatagai, and Yoshiaki Yasuno. Optical coherence angiography. *Optics express*, 14(17):7821–7840, 2006.

[69] Anqi Zhang, Qinqin Zhang, Chieh-Li Chen, and Ruikang K Wang. Methods and algorithms for optical coherence tomography-based angiography: a review and comparison. *Journal of biomedical optics*, 20(10):100901–100901, 2015.

[70] Ruikang K Wang, Qinqin Zhang, Yuandong Li, and Shaozhen Song. Optical coherence tomography angiography-based capillary velocimetry. *Journal of biomedical optics*, 22(6):066008–066008, 2017.

[71] Martin Kallab, Nikolaus Hommer, Bingyao Tan, Martin Pfister, Andreas Schlatter, René M Werkmeister, Jacqueline Chua, Doreen Schmidl, Leopold Schmetterer, and Gerhard Garhöfer. Plexus-specific effect of flicker-light stimulation on the retinal microvasculature assessed with optical coherence tomography angiography. *American Journal of Physiology-Heart and Circulatory Physiology*, 320(1):H23–H28, 2021.

[72] Yunchan Hwang, Jungeun Won, Antonio Yaghy, Hiroyuki Takahashi, Jessica M Girgis, Kenneth Lam, Siyu Chen, Eric M Moult, Stefan B Ploner, Andreas Maier, et al. Retinal blood flow speed quantification at the capillary level using temporal autocorrelation fitting octa. *Biomedical Optics Express*, 14(6):2658–2677, 2023.

[73] Ravi S Jonnal, Jungtae Rha, Yan Zhang, Barry Cense, Weihua Gao, and Donald T Miller. In vivo functional imaging of human cone photoreceptors. *Optics express*, 15(24):16141–16160, 2007.

[74] Dierck Hillmann, Hendrik Spahr, Clara Pfäffle, Helge Sudkamp, Gesa Franke, and Gereon Hüttmann. In vivo optical imaging of physiological responses to photostimulation in human photoreceptors. *Proceedings of the National Academy of Sciences*, 113(46):13138–13143, 2016.

[75] Taeyoon Son, Minhaj Alam, Devrim Toslak, Benquan Wang, Yiming Lu, and Xincheng Yao. Functional optical coherence tomography of neurovascular coupling interactions in the retina. *Journal of biophotonics*, 11(12):e201800089, 2018.

[76] Furu Zhang, Kazuhiro Kurokawa, Ayoub Lassoued, James A Crowell, and Donald T Miller. Cone photoreceptor classification in the living human eye from photostimulation-induced phase dynamics. *Proceedings of the National Academy of Sciences*, 116(16):7951–7956, 2019.

[77] Mehdi Azimipour, Denise Valente, Kari V Vienola, John S Werner, Robert J Zawadzki, and Ravi S Jonnal. Optoretinogram: optical measurement of human cone and rod photoreceptor responses to light. *Optics letters*, 45(17):4658–4661, 2020.

[78] Vimal Prabhu Pandiyan, Xiaoyun Jiang, Aiden Maloney-Bertelli, James A Kuchenbecker, Utkarsh Sharma, and Ramkumar Sabesan. High-speed adaptive optics line-scan oct for cellular-resolution optoretinography. *Biomedical optics express*, 11(9):5274–5296, 2020.

[79] Vimal Prabhu Pandiyan, Aiden Maloney-Bertelli, James A Kuchenbecker, Kevin C Boyle, Tong Ling, Zhijie Charles Chen, B Hyle Park, Austin Roorda, Daniel Palanker, and Ramkumar Sabesan. The optoretinogram reveals the primary steps of phototransduction in the living human eye. *Science advances*, 6(37):eabc1124, 2020.

[80] Guangying Ma, Taeyoon Son, Tae-Hoon Kim, and Xincheng Yao. In vivo optoretinography of phototransduction activation and energy metabolism in retinal photoreceptors. *Journal of biophotonics*, 14(5):e202000462, 2021.

[81] Ewelina Pijewska, Pengfei Zhang, Michał Meina, Ratheesh K Meleppat, Maciej Szkulmowski, and Robert J Zawadzki. Extraction of phase-based optoretinograms (org) from serial b-scans acquired over tens of seconds by mouse retinal raster scanning oct system. *Biomedical Optics Express*, 12(12):7849–7871, 2021.

[82] Austin Roorda. Optoretinography is coming of age. *Proceedings of the National Academy of Sciences*, 118(51):e2119737118, 2021.

[83] Sławomir Tomczewski, Piotr Węgrzyn, Dawid Borycki, Egidijus Auksorius, Maciej Wojtkowski, and Andrea Curatolo. Light-adapted flicker optoretinograms captured with a spatio-temporal optical coherence-tomography (stoc-t) system. *Biomedical Optics Express*, 13(4):2186–2201, 2022.

[84] Vimal Prabhu Pandiyan, Sierra Schleufer, Emily Slezak, James Fong, Rishi Upadhyay, Austin Roorda, Ren Ng, and Ramkumar Sabesan. Characterizing cone spectral classification by optoretinography. *Biomedical Optics Express*, 13(12):6574–6594, 2022.

[85] Clara Pfäffle, Hendrik Spahr, Katharina Gercke, Léo Puyo, Svea Höhl, David Melenberg, Yoko Miura, Gereon Hüttmann, and Dierck Hillmann. Phase-sensitive measurements of depth-dependent signal transduction in the inner plexiform layer. *Frontiers in medicine*, 9:885187, 2022.

[86] Kari V Vienola, Denise Valente, Robert J Zawadzki, and Ravi S Jonnal. Velocity-based optoretinography for clinical applications. *Optica*, 9(10):1100–1108, 2022.

[87] Bingyao Tan, Huakun Li, Yueming Zhuo, Le Han, Rajeshkumar Mupparapu, Davide Nanni, Veluchamy Amutha Barathi, Daniel Palanker, Leopold Schmetterer, and Tong Ling. Light-evoked deformations in rod photoreceptors, pigment epithelium and subretinal space revealed by prolonged and multilayered optoretinography. *Nature Communications*, 15(1):5156, 2024.

[88] Sławomir Tomczewski, Piotr Węgrzyn, Maciej Wojtkowski, and Andrea Curatolo. Chirped flicker optoretinography for in vivo characterization of human photoreceptors' frequency response to light. *Optics Letters*, 49(9):2461–2464, 2024.

[89] K Bizheva, Renate Pflug, Boris Hermann, Boris Považay, H Sattmann, P Qiu, E Anger, Herbert Reitsamer, Sergei Popov, JR Taylor, et al. Optophysiology: depth-resolved probing of retinal physiology with functional ultrahigh-resolution optical coherence tomography. *Proceedings of the national academy of sciences*, 103(13):5066–5071, 2006.

[90] Helga Kolb, Eduardo Fernandez, and Ralph Nelson. The organization of the retina and visual system. *Webvision-the organization of the retina and visual system*, 2005.

[91] Navid Mahabadi and Yasir Al Khalili. *Neuroanatomy, retina*. StatPearls Publishing, 2019.

[92] Richard H Masland. The neuronal organization of the retina. *Neuron*, 76(2):266–280, 2012.

[93] Gilbert T Feke, Hiroshi Tagawa, Dana M Deupree, Douglas G Goger, Jerry Sebag, and JJ Weiter. Blood flow in the normal human retina. *Investigative ophthalmology & visual science*, 30(1):58–65, 1989.

[94] A Aim. Ocular circulation//adler's physiology of the eye, 1992.

[95] Julie L Schnapf and Denis A Baylor. How photoreceptor cells respond to light. *Scientific American*, 256(4):40–47, 1987.

[96] Raymond L Warner, Alberto de Castro, Lucie Sawides, Tom Gast, Kaitlyn Sapoznik, Ting Luo, and Stephen A Burns. Full-field flicker evoked changes in parafoveal retinal blood flow. *Scientific Reports*, 10(1):16051, 2020.

[97] Alex D Pechauer, David Huang, and Yali Jia. Detecting blood flow response to stimulation of the human eye. *BioMed research international*, 2015(1):121973, 2015.

[98] Stephen A Burns, Ann E Elsner, and Thomas J Gast. Imaging the retinal vasculature. *Annual review of vision science*, 7(1):129–153, 2021.

[99] Michael A Duquay. Light photographed in flight. *American Scientist*, 59(5):550–556, 1971.

[100] MA Duguay and AT Mattick. Ultrahigh speed photography of picosecond light pulses and echoes. *Applied Optics*, 10(9):2162–2170, 1971.

[101] R Leitgeb, CK Hitzenberger, and Adolf F Fercher. Performance of fourier domain vs. time domain optical coherence tomography. *Optics express*, 11(8):889–894, 2003.

[102] Robert Huber, Desmond C Adler, Vivek J Srinivasan, and James G Fujimoto. Fourier domain mode locking at 1050 nm for ultra-high-speed optical coherence tomography of the human retina at 236,000 axial scans per second. *Optics letters*, 32(14):2049–2051, 2007.

[103] Bingyao Tan, Zohreh Hosseinaee, Le Han, Olivera Kralj, Luigina Sorbara, and Kostadinka Bizheva. 250 khz, 1.5 μm resolution sd-oct for in-vivo cellular imaging of the human cornea. *Biomedical optics express*, 9(12):6569–6583, 2018.

[104] Michael Münter, Mario Pieper, Tabea Kohlfaerber, Ernst Bodenstorfer, Martin Ahrens, Christian Winter, Robert Huber, Peter König, Gereon Hüttmann, and Hinnerk Schulz-Hildebrandt. Microscopic optical coherence tomography (moct) at 600 khz for 4d volumetric imaging and dynamic contrast. *Biomedical Optics Express*, 12(10):6024–6039, 2021.

[105] Wolfgang Wieser, Benjamin R Biedermann, Thomas Klein, Christoph M Eigenwillig, and Robert Huber. Multi-megahertz oct: High quality 3d imaging at 20 million a-scans and 4.5 gvoxels per second. *Optics express*, 18(14):14685–14704, 2010.

[106] Andrés F Zuluaga and Rebecca Richards-Kortum. Spatially resolved spectral interferometry for determination of subsurface structure. *Optics letters*, 24(8):519–521, 1999.

[107] Daniel J Fechtig, Branislav Grajciar, Tilman Schmoll, Cedric Blatter, Rene M Werkmeister, Wolfgang Drexler, and Rainer A Leitgeb. Line-field parallel swept source mhz oct for structural and functional retinal imaging. *Biomedical optics express*, 6(3):716–735, 2015.

[108] Vimal Prabhu Pandiyan, Xiaoyun Jiang, James A Kuchenbecker, and Ramkumar Sabesan. Reflective mirror-based line-scan adaptive optics oct for imaging retinal structure and function. *Biomedical optics express*, 12(9):5865–5880, 2021.

[109] Le Han, Bingyao Tan, Zohreh Hosseinaee, Lin Kun Chen, Denise Hileeto, and Kostadinka Bizheva. Line-scanning sd-oct for in-vivo, non-contact, volumetric, cellular resolution imaging of the human cornea and limbus. *Biomedical Optics Express*, 13(7):4007–4020, 2022.

[110] Keyu Chen, Weixiang Song, Le Han, and Kostadinka Bizheva. Powell lens-based line-field spectral domain optical coherence tomography system for cellular resolution imaging of biological tissue. *Biomedical Optics Express*, 14(5):2003–2014, 2023.

[111] Zijian Zhang, Xingyu Yang, Zhiyi Zhao, Feng Zeng, Sicong Ye, Sara J Baldock, Hungyen Lin, John G Hardy, Yalin Zheng, and Yaochun Shen. Rapid imaging and product screening with low-cost line-field fourier domain optical coherence tomography. *Scientific reports*, 13(1):10809, 2023.

[112] Kai Neuhaus, Shanjida Khan, Omkar Thaware, Shuibin Ni, Mini Aga, Yali Jia, Travis Redd, Siyu Chen, David Huang, and Yifan Jian. Real-time line-field optical coherence tomography for cellular resolution imaging of biological tissue. *Biomedical Optics Express*, 15(2):1059–1073, 2024.

[113] Boris Považay, Angelika Unterhuber, Boris Hermann, Harald Sattmann, Holger Arthaber, and Wolfgang Drexler. Full-field time-encoded frequency-domain optical coherence tomography. *Optics Express*, 14(17):7661–7669, 2006.

[114] Patrycjusz Stremplewski, Egidijus Auksorius, Paweł Wnuk, Łukasz Kozoń, Piotr Garstecki, and Maciej Wojtkowski. In vivo volumetric imaging by crosstalk-free full-field oct. *Optica*, 6(5):608–617, 2019.

[115] Egidijus Auksorius, Dawid Borycki, Piotr Wegrzyn, Ieva Žičkienė, Karolis Adomavičius, Bartosz L Sikorski, and Maciej Wojtkowski. Multimode fiber as a tool to reduce cross talk in fourier-domain full-field optical coherence tomography. *Optics Letters*, 47(4):838–841, 2022.

[116] Tim Bonin, Gesa Franke, Martin Hagen-Eggert, Peter Koch, and Gereon Hüttmann. In vivo fourier-domain full-field oct of the human retina with 1.5 million a-lines/s. *Optics letters*, 35(20):3432–3434, 2010.

[117] Helge Sudkamp, Peter Koch, Hendrik Spahr, Dierck Hillmann, Gesa Franke, Michael Münst, Fred Reinholz, Reginald Birngruber, and Gereon Hüttmann. In-vivo retinal imaging with off-axis full-field time-domain optical coherence tomography. *Optics Letters*, 41(21):4987–4990, 2016.

[118] Jinze Zhang, Viacheslav Mazlin, Keyi Fei, Albert Claude Boccara, Jin Yuan, and Peng Xiao. Time-domain full-field optical coherence tomography (td-ff-oct) in ophthalmic imaging. *Therapeutic Advances in Chronic Disease*, 14:20406223231170146, 2023.

[119] Kamil Liżewski, Slawomir Tomczewski, Dawid Borycki, Piotr Węgrzyn, and Maciej Wojtkowski. Imaging the retinal and choroidal vasculature using spatio-temporal optical coherence tomography (stoc-t). *Biocybernetics and Biomedical Engineering*, 44(1):95–104, 2024.

[120] Ratheesh K Meleppat, Denise Valente, Soohyun Lee, Ravi S Jonnal, Nathan Doble, and Robert J Zawadzki. On-axis full-field swept-source optical coherence tomography for murine retinal imaging. *Optics Letters*, 49(16):4630–4633, 2024.

[121] Benjamin J Vakoc, Seok-Hyun Yun, Johannes F De Boer, Guillermo J Tearney, and Brett E Bouma. Phase-resolved optical frequency domain imaging. *Optics express*, 13(14):5483–5493, 2005.

[122] Gerold C Aschinger, Leopold Schmetterer, Klemens Fondi, Valentin Aranha Dos Santos, Gerald Seidel, Gerhard Garhöfer, and René M Werkmeister. Effect of diffuse luminance flicker light stimulation on total retinal blood flow assessed with dual-beam bidirectional doppler oct. *Investigative Ophthalmology & Visual Science*, 58(2):1167–1178, 2017.

[123] Leila Kantola, Marco Piccolino, and Nicholas J Wade. The action of light on the retina: Translation and commentary of holmgren (1866). *Journal of the History of the Neurosciences*, 28(4):399–415, 2019.

[124] RA Stepnoski, A LaPorta, F Raccuia-Behling, GE Blonder, RE Slusher, and D Kleinfeld. Noninvasive detection of changes in membrane potential in cultured neurons by light scattering. *Proceedings of the National Academy of Sciences*, 88(21):9382–9386, 1991.

[125] Xin-Cheng Yao, Angela Yamauchi, Beth Perry, and John S George. Rapid optical coherence tomography and recording functional scattering changes from activated frog retina. *Applied optics*, 44(11):2019–2023, 2005.

[126] VJ Srinivasan, M Wojtkowski, JG Fujimoto, and JS Duker. In vivo measurement of retinal physiology with high-speed ultrahigh-resolution optical coherence tomography. *Optics letters*, 31(15):2308–2310, 2006.

[127] Pengfei Zhang, Robert J Zawadzki, Mayank Goswami, Phuong T Nguyen, Vladimir Yarov-Yarovoy, Marie E Burns, and Edward N Pugh Jr. In vivo optophysiology reveals that g-protein activation triggers osmotic swelling and increased light scattering of rod photoreceptors. *Proceedings of the National Academy of Sciences*, 114(14):E2937–E2946, 2017.

[128] Pengfei Zhang, Bradley Shibata, Gabriel Peinado, Robert J Zawadzki, Paul FitzGerald, and Edward N Pugh. Measurement of diurnal variation in rod outer segment length in vivo in mice with the oct optoretinogram. *Investigative ophthalmology & visual science*, 61(3):9–9, 2020.

[129] Tae-Hoon Kim, Guangying Ma, Taeyoon Son, and Xincheng Yao. Functional optical coherence tomography for intrinsic signal optoretinography: recent developments and deployment challenges. *Frontiers in Medicine*, 9:864824, 2022.

[130] Robert F Cooper, David H Brainard, and Jessica IW Morgan. Optoretinography of individual human cone photoreceptors. *Optics express*, 28(26):39326–39339, 2020.

[131] Anat London, Inbal Benhar, and Michal Schwartz. The retina as a window to the brain—from eye research to cns disorders. *Nature Reviews Neurology*, 9(1):44–53, 2013.

[132] World Health Organization et al. World report on vision. 2019.

[133] Piotr Węgrzyn, Wiktor Kulesza, Maciej Wielgo, Sławomir Tomczewski, Anna Galińska, Bartłomiej Bałamut, Katarzyna Kordecka, Onur Cetinkaya, Andrzej Foik, Robert J Zawadzki, et al. In vivo volumetric analysis of retinal vascular hemodynamics in mice with spatio-temporal optical coherence tomography. *Neurophotonics*, 11(4):045003–045003, 2024.

[134] Vivek J Srinivasan, Aaron M Kho, and Pooja Chauhan. Visible light optical coherence tomography reveals the relationship of the myoid and ellipsoid to band 2 in humans. *Translational vision science & technology*, 11(9):3–3, 2022.

[135] Omer P Kocaoglu, Timothy L Turner, Zhuolin Liu, and Donald T Miller. Adaptive optics optical coherence tomography at 1 mhz. *Biomedical optics express*, 5(12):4186–4200, 2014.

[136] Zhuolin Liu, Furu Zhang, Kelvy Zucca, Anant Agrawal, and Daniel X Hammer. Ultrahigh-speed multimodal adaptive optics system for microscopic structural and functional imaging of the human retina. *Biomedical optics express*, 13(11):5860–5878, 2022.

[137] Ruikang K Wang. Optical microangiography: a label-free 3-d imaging technology to visualize and quantify blood circulations within tissue beds in vivo. *IEEE Journal of Selected Topics in Quantum Electronics*, 16(3):545–554, 2009.

[138] Guangru B Liang, Shuibin Ni, Tristan T Hormel, John C Morrison, Diana C Lozano, Yifan Jian, J Peter Campbell, and Yali Jia. 112° field of view high-resolution swept-source oct angiography for rat retinas. *Optics Letters*, 49(22):6449–6452, 2024.

[139] Liang Wang, Olwen Murphy, Natalia Gonzalez Caldito, Peter A Calabresi, and Shiv Saidha. Emerging applications of optical coherence tomography angiography (octa) in neurological research. *Eye and Vision*, 5:1–11, 2018.

[140] ANSI Z136.1-2022. *American national standard for safe use of lasers*. Laser Institute of America, 2022.

[141] WAH Rushton and GH Henry. Bleaching and regeneration of cone pigments in man. *Vision research*, 8(6):617–631, 1968.

[142] Manuel Guizar-Sicairos, Samuel T Thurman, and James R Fienup. Efficient subpixel image registration algorithms. *Optics letters*, 33(2):156–158, 2008.

[143] Huakun Li, Bingyao Tan, Vimal Prabhu Pandiyan, Veluchamy Amutha Barathi, Ramkumar Sabesan, Leopold Schmetterer, and Tong Ling. Phase-restoring subpixel image registration: Enhancing motion detection performance in fourier-domain optical coherence tomography. *bioRxiv*, pages 2022–06, 2022.

[144] Andrew Lang, Aaron Carass, Matthew Hauser, Elias S Sotirchos, Peter A Calabresi, Howard S Ying, and Jerry L Prince. Retinal layer segmentation of macular oct images using boundary classification. *Biomedical optics express*, 4(7):1133–1152, 2013.

[145] Khushmeet Kaur Dhaliwal, James Simmons, Alex Wong, Chris Hudson, Brian Ballios, and Kostadinka K Bizheva. Transient, visually-evoked changes in human retinal

blood flow velocity and vessel diameter measured with oct. *Investigative Ophthalmology & Visual Science*, 65(7):3413–3413, 2024.

[146] WooJhon Choi, Benjamin Potsaid, Vijaysekhar Jayaraman, Bernhard Baumann, Ireneusz Grulkowski, Jonathan J Liu, Chen D Lu, Alex E Cable, David Huang, Jay S Duker, et al. Phase-sensitive swept source oct imaging of the human retina with a vcsel light source. *Optics letters*, 38(3):338, 2013.

[147] Bingyao Tan, Benjamin MacLellan, Erik Mason, and Kostadinka K Bizheva. The effect of acutely elevated intraocular pressure on the functional and blood flow responses of the rat retina to flicker stimulation. *Investigative Ophthalmology & Visual Science*, 58(12):5532–5540, 2017.

[148] Zhangyi Zhong, Gang Huang, Toco Yuen Ping Chui, Benno L Petrig, and Stephen A Burns. Local flicker stimulation evokes local retinal blood velocity changes. *Journal of vision*, 12(6):3–3, 2012.

[149] CE Riva, S Harino, RD Shonat, and BL Petrig. Flicker evoked increase in optic nerve head blood flow in anesthetized cats. *Neuroscience letters*, 128(2):291–296, 1991.

[150] CE Riva, CJ Pournaras, CL Poitry-Yamate, and BL Petrig. Rhythmic changes in velocity, volume, and flow of blood in the optic nerve head tissue. *Microvascular research*, 40(1):36–45, 1990.

[151] Hean C Chen, Vinod Patel, Jutta Wiek, Salwan M Rassam, and Eva M Kohner. Vessel diameter changes during the cardiac cycle. *Eye*, 8(1):97–103, 1994.

[152] GSP Santos, PHDM Prazeres, A Mintz, and A Birbrair. Role of pericytes in the retina. *Eye*, 32(3):483–486, 2018.

[153] Taeyoon Son, Guangying Ma, and Xincheng Yao. Functional oct reveals anisotropic changes of retinal flicker-evoked vasodilation. *Optics Letters*, 49(8):2121–2124, 2024.

[154] Yi Liu, Charles Dang, Marisa Garcia, Hans Gregersen, and Ghassan S Kassab. Surrounding tissues affect the passive mechanics of the vessel wall: theory and experiment. *American Journal of Physiology-Heart and Circulatory Physiology*, 293(6):H3290–H3300, 2007.

[155] HW Weizsäcker and K Pascale. Anisotropic passive properties of blood vessel walls. In *Cardiovascular system dynamics: models and measurements*, pages 347–362. Springer, 1982.

[156] J Zhou and YC Fung. The degree of nonlinearity and anisotropy of blood vessel elasticity. *Proceedings of the National Academy of Sciences*, 94(26):14255–14260, 1997.

[157] Siamak Mishani, Hanane Belhoul-Fakir, Chris Lagat, Shirley Jansen, Brian Evans, and Michael Lawrence-Brown. Stress distribution in the walls of major arteries: implications for atherogenesis. *Quantitative imaging in medicine and surgery*, 11(8):3494, 2021.

[158] Devin D Mackay, Philip S Garza, Beau B Bruce, Nancy J Newman, and Valérie Biousse. The demise of direct ophthalmoscopy: a modern clinical challenge. *Neurology: Clinical Practice*, 5(2):150–157, 2015.

[159] Donald G Buerk, Charles E Riva, and Stephan D Cranstoun. Frequency and luminance-dependent blood flow and k+ ion changes during flicker stimuli in cat optic nerve head. *Investigative ophthalmology & visual science*, 36(11):2216–2227, 1995.

[160] Junichi Kiryu, Sanjay Asrani, Mahnaz Shahidi, Marek Mori, and Ran Zeimer. Local response of the primate retinal microcirculation to increased metabolic demand induced by flicker. *Investigative ophthalmology & visual science*, 36(7):1240–1246, 1995.

[161] Janette Atkinson. Early visual development: Differential functioning of parvocellular and magnocellular pathways. *Eye*, 6(2):129–135, 1992.

[162] Samuel G Solomon. Retinal ganglion cells and the magnocellular, parvocellular, and koniocellular subcortical visual pathways from the eye to the brain. In *Handbook of Clinical Neurology*, volume 178, pages 31–50. Elsevier, 2021.

[163] Charles E Riva, Benedetto Falsini, and Eric Logean. Flicker-evoked responses of human optic nerve head blood flow: luminance versus chromatic modulation. *Investigative ophthalmology & visual science*, 42(3):756–762, 2001.

[164] Junya Hanaguri, Harumasa Yokota, Masahisa Watanabe, Lih Kuo, Satoru Yamagami, and Taiji Nagaoka. Longitudinal stability of retinal blood flow regulation in response to flicker stimulation and systemic hyperoxia in mice assessed with laser speckle flowgraphy. *Scientific reports*, 10(1):19796, 2020.

[165] Benedetto Falsini, Charles E Riva, and Eric Logean. Flicker-evoked changes in human optic nerve blood flow: relationship with retinal neural activity. *Investigative ophthalmology & visual science*, 43(7):2309–2316, 2002.

[166] Vo Van Toi and CE Riva. Variations of blood flow at optic nerve head induced by sinusoidal flicker stimulation in cats. *The Journal of physiology*, 482(1):189–202, 1995.

[167] Marci L DeRamus and Timothy W Kraft. Optimizing erg measures of scotopic and photopic critical flicker frequency. In *Retinal Degenerative Diseases: Mechanisms and Experimental Therapy*, pages 145–150. Springer, 2018.

[168] Christine A Curcio, Kimberly A Allen, Kenneth R Sloan, Connie L Lerea, James B Hurley, Ingrid B Klock, and Ann H Milam. Distribution and morphology of human cone photoreceptors stained with anti-blue opsin. *Journal of comparative neurology*, 312(4):610–624, 1991.

[169] Austin Roorda and David R Williams. The arrangement of the three cone classes in the living human eye. *Nature*, 397(6719):520–522, 1999.

[170] Lindsay T Sharpe, Andrew Stockman, and Donald IA MacLeod. Rod flicker perception: scotopic duality, phase lags and destructive interference. *Vision research*, 29(11):1539–1559, 1989.

[171] David J Calkins. Seeing with s cones. *Progress in retinal and eye research*, 20(3):255–287, 2001.

[172] Peter Gouras. The role of s-cones in human vision. *Documenta ophthalmologica*, 106:5–11, 2003.

[173] Sophie K Herbst, Amir Homayoun Javadi, Elke van der Meer, and Niko A Busch. How long depends on how fast—perceived flicker dilates subjective duration. *PloS one*, 8(10):e76074, 2013.

[174] Xiaofan Jiang and Omar A Mahroo. Human retinal dark adaptation tracked in vivo with the electroretinogram: insights into processes underlying recovery of cone-and rod-mediated vision. *The Journal of Physiology*, 600(21):4603–4621, 2022.